Master's degree course in Automotive Engineering

Academic year 2024/2025

Graduation session of March 2025

Assessment of a 3.0L diesel engine model developed in GT-SUITE environment

Supervisors:
Prof. Roberto Finesso
Prof. Stefano D'Ambrosio
Dott. Omar Marello

Candidate:
Francesco Guidotti 317358

Abstract

The goal of this thesis is to validate a GT-SUITE model of a 3.0L diesel engine through a series of steady-state tests. The starting point is the comparison between two versions of the same engine model. The first model is equipped with an After-Treatment System (ATS), while the second is not.
The first engine model uses a map of convective heat transfer coefficients, whose values lack physical consistency, as they deviate significantly from experimental data. This map has been adopted to achieve an accurate prediction of the tailpipe exhaust gas temperatures, which serve as boundary conditions for the ATS. In contrast, the second engine model does not include this map and instead adopts a single convective heat transfer coefficient. This coefficient has a more physically consistent value but results in an overestimation of the exhaust gas temperatures compared to the experimental data.
This thesis focuses on the second engine model, with the aim of refining it to better predict the exhaust gas temperatures, while simultaneously adopting calibration parameters that remain physically consistent.

Contents

List of Figures

List of Tables

Chapter 1

Introduction

1.1 The concept of "Digital Twin"

Nowadays one of the main challenges is the reduction of the pollutant emissions, which are seriously threatening the enviromental balance. For this reason the legislative restrictions about them are becoming more and more rigorous. A great responsibility lies with the automotive industry, which is working hardly to comply with these limitations, developing new technologies and refining those that already exist. A very important strategy by which it is possible to reach these goals concerns the so called "Digital Twin", i.e. the digital version of a real system that tries to reproduce as much as possible the functioning and the outcomes of the latter. In this way, it is possible to carry out tests and studies directly on this virtual system, without resorting to a real one. The advantages are mainly a more effective development and a greater ease of optimization, since having a system within a specific software gives more margin of control and problem solving. Furthermore, a relevant percentage of economical and energetic resources can be saved, thanks to the possibility of avoiding a real system and its complex experimental setup. The hard task is to ensure that the virtual system has the highest possible level of fidelity to the reality, not 100 % achievable, but surely a notable approach can be obtained. This thesis focuses on this type of task, evaluating the digital twin of a diesel engine.

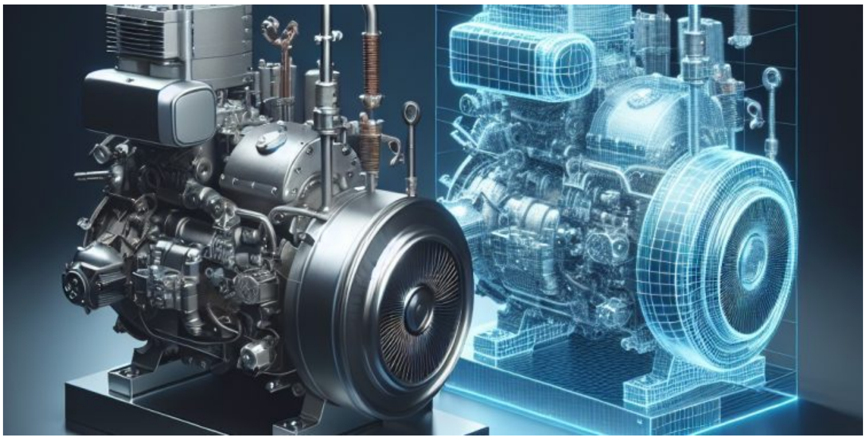

Figure 1.1: Illustration of "Digital Twin" concept [1].

1.2 Engine and testing conditions

The engine used in this work is a 3.0L diesel engine, suitable for Light Commercial Vehicles (LCV) application. The main technical specifications of this engine are reported in Table 1.1. It is a quite recent diesel engine, compliant to the Euro VI legislation and equipped with all the almost default

systems for a compression ignition engine, i.e. the high-pressure Common Rail, the Exhaust Gas Recirculation (EGR) and the Turbocharger.
This engine can be subjected to various types of tests. The typology of test on which this thesis is based concerns the steady-state condition. This means that the engine was run imposing working points which are independent of time. The tests were performed in a specific experimental test bench, and their results are taken as the experimental data set of reference. More details about these steady-state tests, in particular about their working points, will be provided in the next chapter.

Engine technical specifications

Engine type	Euro VI diesel engine
Number of cylinders	4
Valves per cylinder	4
Total displacement	2998 cm^3
Bore × Stroke	95.8 mm × 104 mm
Rod length	160 mm
Compression ratio	17.5
Fuel injection system	High-pressure Common Rail
EGR type	Short-route, equipped with cooler
Turbocharger type	VGT
Exhaust flap valve	Positioned at the turbine outlet

Table 1.1: Essential technical specifications of the engine.

1.3 Software used

The digital twin of the diesel engine is implemented in GT-SUITE environment, a specific software for the modeling and simulation of internal combustion engines and much more. In fact, this software is aimed at many areas of the engineerig fields, allowing to perform a large variety of actions, from the concept design to the detailed system analysis [2].
GT-SUITE software is made up of many applications. In this thesis two of them will be used, that are GT-ISE and GT-POST. The first is the main model builder, exploited for the interaction with the engine model blocks, with the possibility of building new ones and modifying them by the change of the related parameters. Regarding GT-POST, it is the software application in which the simulation of the GT-ISE model can run, allowing to consult all the outcomes related to every model block.
In this thesis, the results of each simulation are extracted from GT-POST and are collected in Microsoft Excel environment, ordering them into tables. Then these data are imported in MATLAB software, by which specific diagrams are made, to visualize and analyze all the outcomes. Therefore, for the post-processing of the results, once each simulation has been run, the following procedural logic is adopted to obtain all the plots shown in the next chapters:

$$\text{GT-POST} \rightarrow \text{Excel} \rightarrow \text{MATLAB}$$

Regarding the experimental results, they were provided directly by an Excel table. There are a large amount of quantities, and only the ones considered are imported into MATLAB, to make the comparison with the corresponding quantities supplied by the engine model.

1.4 Thesis goal

This thesis starts with the analysis of two versions of the same engine model: a version equipped with After Treatment System (ATS) and a version not equipped with ATS. These two models will be deeply described and the results of the initial simulation for each engine model will be examined. Then the two models will be compared, exploring all their differences, beyond the one related to the presence of the ATS. There will be an important difference that will lead to discard the engine model with ATS and to focus exclusively to the other model, studying the effect of some important GT-ISE parameters and understanding how to guarantee to the model a better estimate capability of the experimental quantities. This work will be performed giving to the model a physical consistency, i.e. respecting the limits imposed by the physics within the blocks that define the model itself. Finally, to observe the variation between the original and final versions of the engine model without ATS, there will be a final comparison about each engine quantity.

Chapter 2

Description of the two engine models and initial simulations

2.1 Engine model with ATS

Starting from the engine model with the After Treatment System (ATS), it is possible to observe the entire configuration in Figure 2.1. The first feature of the model to consider is the large amount of detail, highlighted by the great number of GT-ISE blocks. This provides to the model greater possibilities to get closer to a real engine but at the same time gives it a higher level of complexity.

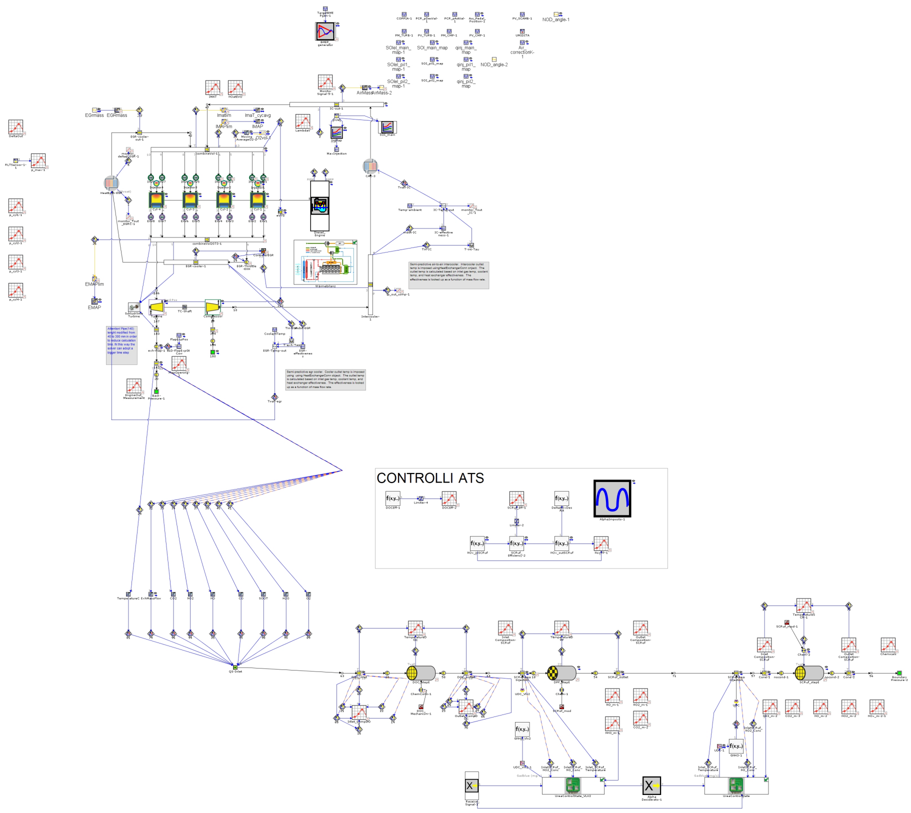

Figure 2.1: Engine model with ATS: full view.

It is necessary to take into account two subsystems to describe the whole engine configuration: the part at the ATS upstream, reported in Figure 2.2, and the ATS itself, shown in Figure 2.3. Since the first subsystem has a fundamental role in this thesis, especially about the comparison with the other engine model, it will be accurately analyzed. In fact, all its main parts will be

described, starting from the group that includes the cylinders, the valves, the injectors, and the manifolds. Then the part which regards the kinematics and the rigid dynamics of the engine will be illustrated, that is the engine cranktrain. The Exhaust Gas Recirculation (EGR) with its control, the turbo group with the Variable Geometry Turbine (VGT) control, and the intercooler will also be shown.
Regarding the ATS model, it has been carefully developed in [3] and since the thesis does not focus on it, a brief description will be reserved for it.

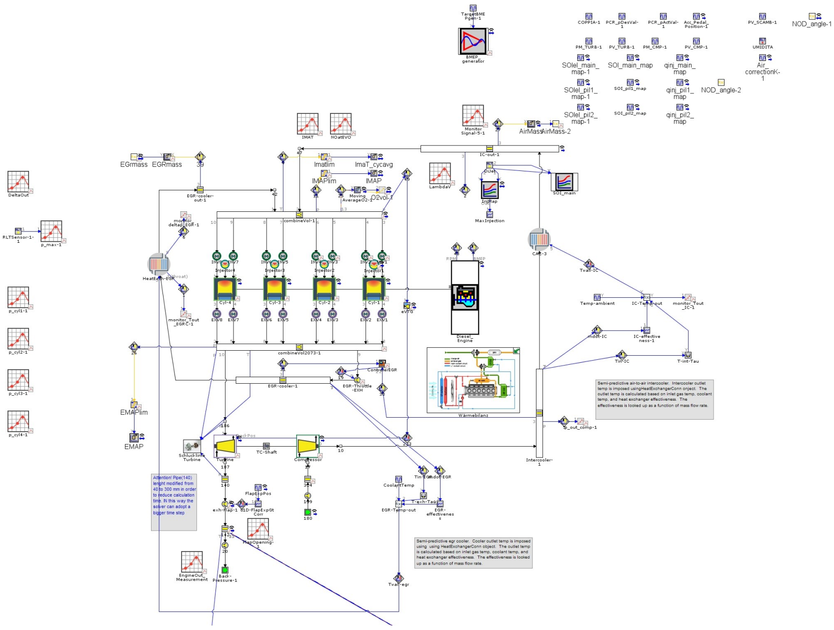

Figure 2.2: Engine model with ATS: ATS upstream view.

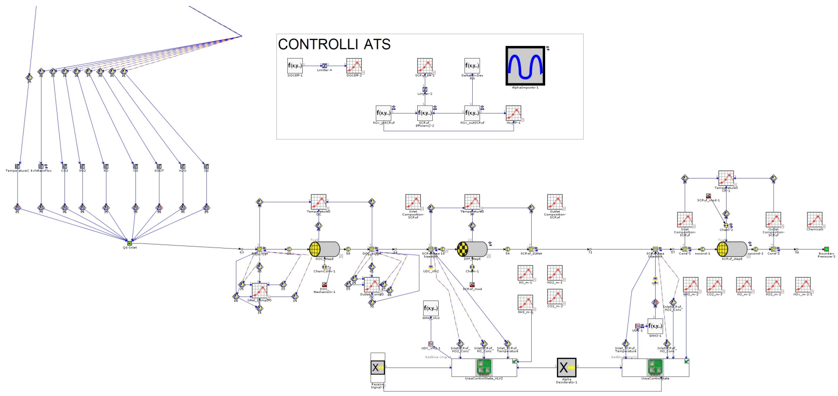

Figure 2.3: Engine model with ATS: ATS view.

2.1.1 Cylinders, valves, injectors and manifolds

Among the ATS upstream subsystem the first group of blocks that can be described is made up of the four cylinders, the sixteen valves, the four injectors and the two manifolds, i.e. the intake and the exhaust ones. This group is shown in Figure 2.4. Every block, in GT-ISE called "part", belongs to a specific "object", that is the reference element which defines the properties of all the related parts. In Figure 2.5 it is possible to observe the engine cylinder object, that provides all the features which the four cylinders, hence its parts, must have. In the main section of this object, there are different fields, each one with a precise property. It is worth examining the most important ones. First of all the *Initial State Object*, which specifies the initial conditions

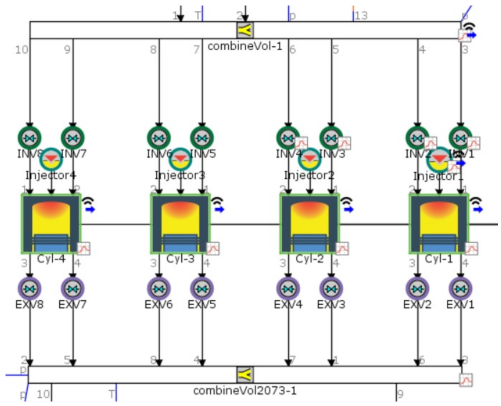

Figure 2.4: Cylinders, valves, injectors and manifolds.

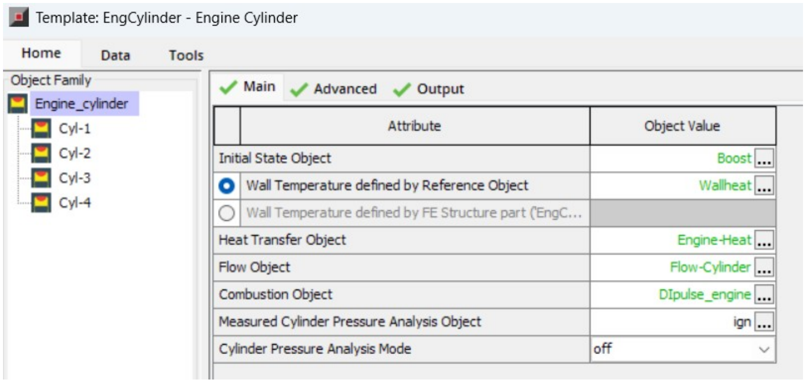

Figure 2.5: Engine cylinder object.

inside the cylinder, i.e. the initial pressure, the initial temperature and the fluid composition. In this field there is the reference object "*Boost*", in which for this engine model the pressure is characterized by the experimental boost values case by case, the initial temperature is of 40 °C and the fluid composition is that of the air. The next field concerns the wall temperature of the cylinder, which in this case is defined by a reference object, called "*Wallheat*". This object will be carefully analyzed in one of the next chapters. For the moment it can be briefly described as the object that defines the geometry and the materials of the cylinder liner, the head, the valves and the piston. Furthermore, it determines the coolant boundary conditions, therefore the thermal properties of the coolant and the oil. Another important field is the *Heat Transfer Object*, in which the heat transfer properties within the cylinder are specified. In particular, the heat transfer model that has been chosen in this case is the Hohenberg one, which is suitable for direct injection diesel engines. In fact, it predicts very accurately the in-cylinder heat transfer for this type of engine. Then there is the *Flow Object* field, which shows the flow features inside the cylinder. The piston cup geometry is specified, and the tumble, the swirl and the turbulence properties are indicated. Finally, the last field that is worth analyzing is the *Combustion Object*, which characterizes the in-cylinder combustion model. All the main properties of the compression ignition are in this object, for instance the ignition delay, the premixed combustion rate and the diffusion combustion rate, predicting also the associated emissions.
Regarding the valves, there are eight intake valves and eight exhaust valves, defined by two objects, one for the intake group and the other for the exhaust group. In these objects the timing, the lift profile and the flow characteristics of the valves group are determined.
Another important group of parts is that of injectors, defined by a single object reported in Figure 2.6. Some sections can be observed, and in the figure the fluid one is selected, in which, considering the engine type, the injected fluid is diesel. Then there is the nozzle section, where the geometry of the injector nozzle is defined, and two last sections on the right determine the profiles of injection. These will be explained more in detail in the fourth chapter.

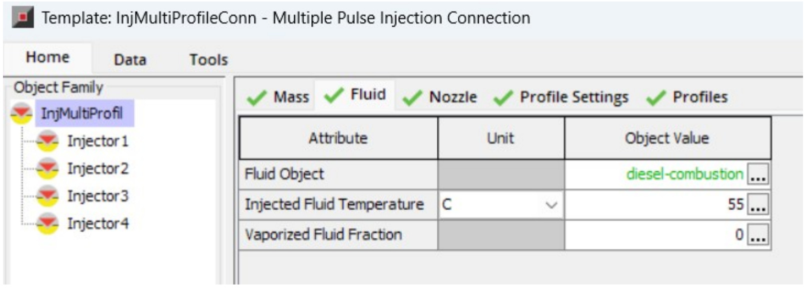

Figure 2.6: Engine injector object.

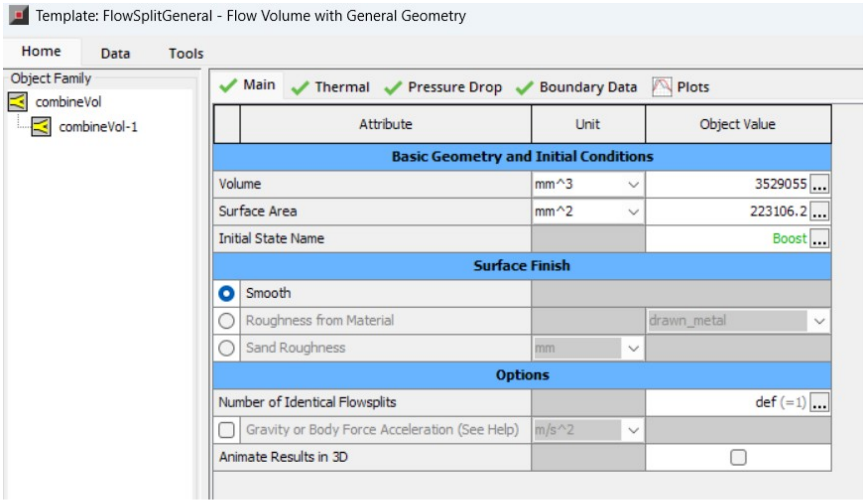

Figure 2.7: Flow volume with general geometry: intake manifold object

Finally, there are the intake and exhaust manifolds, which are defined by the same type of object, i.e. the flow volume with general geometry. Of course, two distinct objects are used, due to the different properties and conditions about the intake and exhaust environment. In Figure 2.7 the object related to the intake manifold is shown. Some sections can be noted, and in the main one the geometry and the initial conditions are defined. It is possible to observe that there is the same *Initial State Object* met inside the cylinder object, and it refers to the boost conditions. Subsequently, in *Thermal* section the wall material and its thermal properties are determined, and this section, about the Exhaust Manifold, will cover a very important role in this thesis. Therefore, it will be deeply explored in the next chapters. Then there is the *Pressure Drop* section, where the pressure losses due to friction are defined. Finally, about the *Boundary data* section, the parts contiguous to the manifold and their spatial positioning are specified within it.

2.1.2 Engine cranktrain

The part that holds the kinematics and rigid dynamics of the engine is the Engine Cranktrain, which is possible to observe in Figure 4.24. The related object is made up of some sections, as it can be seen in Figure 2.9. The *Main* section treats the engine type, in this case a four-stroke, and the speed or load specification, in which the prescribed quantity in the simulation is specified. In this engine layout the appointed quantity is the speed, and so the corresponding engine load variation is computed. Then there is another important field, which is the *Engine Friction Object*, where the parameters of the engine friction model are specified. GT-SUITE uses the Chenn-Flynn engine friction model, based on this relation:

$$FMEP = A + B \cdot p_{max} + C \cdot u + D \cdot u^2 \tag{2.1}$$

where:

- A: FMEP constant term [bar]
- p_{max}: maximum cylinder pressure [bar]
- B: maximum cylinder pressure coefficient [-]
- u: mean piston speed [m/s]
- C: mean piston speed coefficient [bar/(m/s)]
- D: mean piston speed squared coefficient [bar/(m/s)^2]

For what regards the angle in which the cycle starts, the value is of -140 °CA. Then in the other sections the details about the cylinder geometry, the firing order, which is the typical one of a four-cylinders engine, i.e. 1-3-4-2, with evenly spaced cranks, the reference density for the calculation of the engine volumetric efficiency, which is that of the air, the engine effective rotating inertia and the loads acting on bearings can be found.

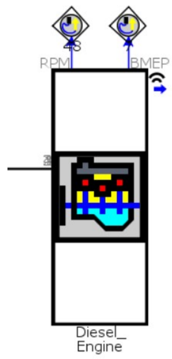

Figure 2.8: Engine cranktrain.

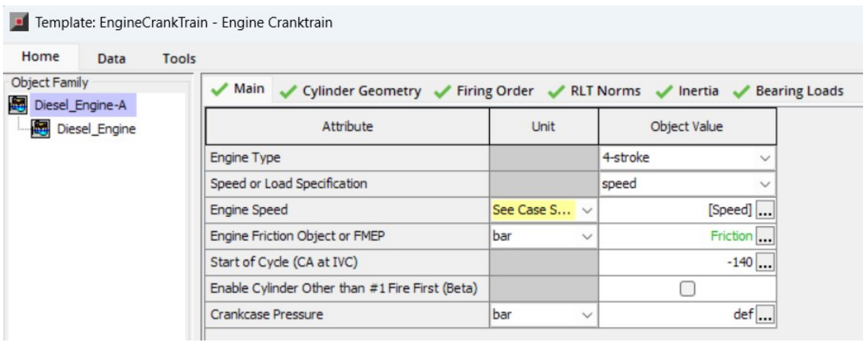

Figure 2.9: Engine cranktrain object.

2.1.3 EGR control

An important part of the engine model is the Exhaust Gas Recirculation (EGR) and the related control, which is of closed-loop nature. The latter is a very crucial part of this engine configuration and it is worth focusing on it. The EGR control is carried out by the part called "*ControllerEGR*", that can be observed in Figure 2.10. In practice, this block receives two feedback variables, one from "*EGR-cooler-1*", i.e. the EGR mass flow rate, and the other from the first intercooler block, reported in Figure 2.17(a), i.e. the air mass flow rate.
The logic with which the block operates is this: the current EGR fraction can be obtained from the two feedback variables , and subtracting it to the target one the corresponding EGR fraction error is computed. The goal of the EGR controller is to ensure a small EGR fraction error, and

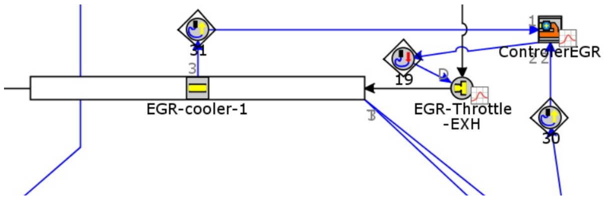

Figure 2.10: Exhaust Gas Recirculation control.

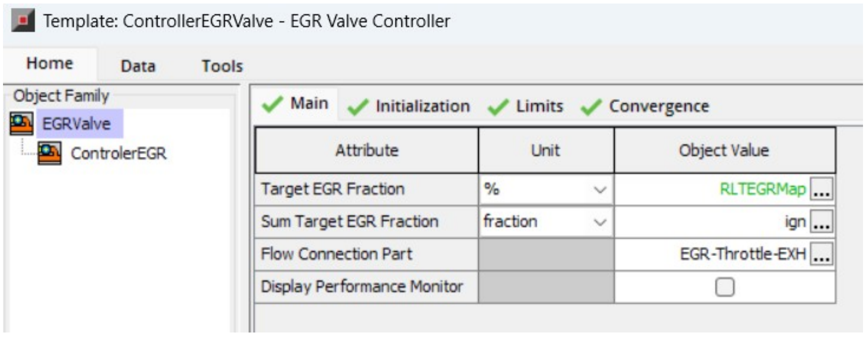

Figure 2.11: EGR valve controller object.

for doing this the variable on which it acts, i.e. its output, is the orifice diameter of the EGR valve, called "*EGR-Throttle-EXH*". The target EGR fraction is the first field of the *Main* section of the EGR valve controller block, reported in Figure 2.11. There is a three-dimensional map, named "*RLTEGRMap*", which has the EGR fraction as a function of the engine speed and BMEP. It is possible also to note the field called "*Flow connection part*", where the part on which the controller acts is specified, i.e. the EGR valve.

2.1.4 Turbo group and VGT control

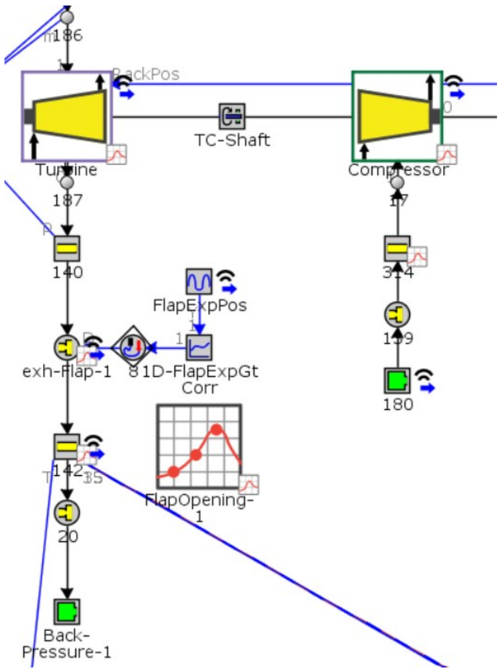

Figure 2.12: Turbo group.

The turbo group is a very detailed subsystem of the engine model, made up of various blocks, as it can be noted in Figure 2.12. It is possible to start from the two green blocks, which represent the

external thermodynamic environments. The "*180*" block defines the thermodynamic conditions at the compressor upstream, in which there are the cabin pressure and temperature, very similar to the typical environmental conditions, and the reference fluid is the air. Instead the "*Back-Pressure-1*" block contains the thermodynamic conditions at the turbine downstream, where the pressure is the same of the compressor upstream, but the temperature is much higher, with a value of 350 °C, and the fluid composition is that of the exhaust gases.
Before describing the compressor, there are some blocks useful to connect in a realistic way the compressor itself with the external upstream environment, and they are two orifices and one pipe. Within the compressor block there are many fields. First of all, the type of compressor is specified, in this case radial. Then the main dimensions are indicated, the reference thermodynamic conditions and the compressor map data are specified. The map identifies the operating characteristic of the compressor and is made up of four group of data, which are the corrected speed, the corrected mass flow rate, the pressure ratio and the efficiency.
The compressor block is connected to the turbine one by "*TC-shaft*" block, which represents the shaft that links mechanically and kinematically the turbine and the compressor. This block is used to model the kinematics and dynamics of the turbocharger shaft.
Regarding the turbine, it is defined by a dedicated block, with the same settings typology of the compressor one. However, the turbine exhibits a more complex feature with respect to the compressor: it is a Variable Geometry Turbine (VGT). This means that a specific turbine map corresponds to a specific rack position. Hence, varying the rack position, it is possible to change the operational characteristic of the turbine. The variation of the rack position is actuated by the VGT control block, reported in Figure 2.13. It is a closed-loop control like the EGR one. In this case there is only a feedback variable, which is the pressure inside the exhaust manifold. The target pressure is the boost one, and a three-dimensional map is exploited, made up of the boost pressure as a function of engine speed and BMEP. The variable on which the controller acts is the rack position. In fact, the output of the controller block is directly linked to the turbine one.

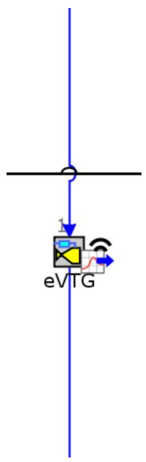

Figure 2.13: Variable Geometry Turbine control.

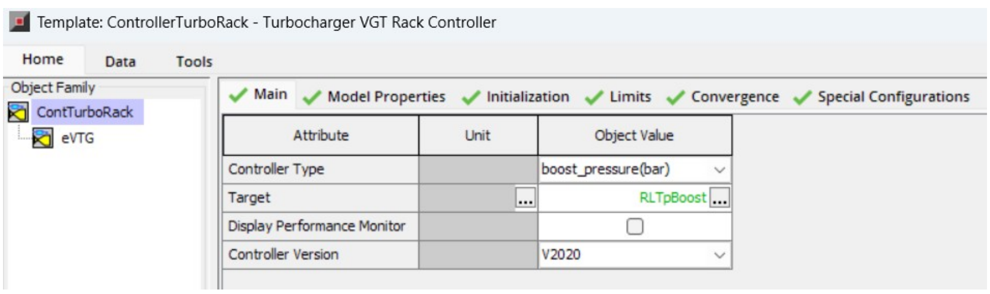

Figure 2.14: VGT controller object.

Between the turbine block and the external environment of the turbine downstream there is a greater number of blocks with respect to the compressor-external environment path. In fact, there are three orifices and two pipes. In particular, it is worth giving attention to the central orifice, named "*exh-Flap-1*". It regards the engine flap, and the amount of its overture is controlled by the open-loop chain on the right(Figure 2.12). The latter is made up of three blocks: a signal generator, a correlation block and an actuator. The signal generator, reported in Figure 2.15, provides a signal based on a constant or dependency reference object. In this case the reference object is a 3D map, in which there is the relative flap closing, i.e. a quantity between 0 and 1, as a function of the engine speed and BMEP. Since this open-loop controller acts on the hole diameter of the orifice "*exh-Flap-1*", a block that converts the flap closing signal into a diameter is needed, and this role is covered by the correlation block, shown in Figure 2.16. This block receives as input the generated signal and gives as output the corresponding diameter, obtained through a one-dimensional lookup table. The latter will be carefully explored in one of the next chapters. The block on the left side of the open-loop chain is the actuator, essential to impose the diameter value to the flap orifice.

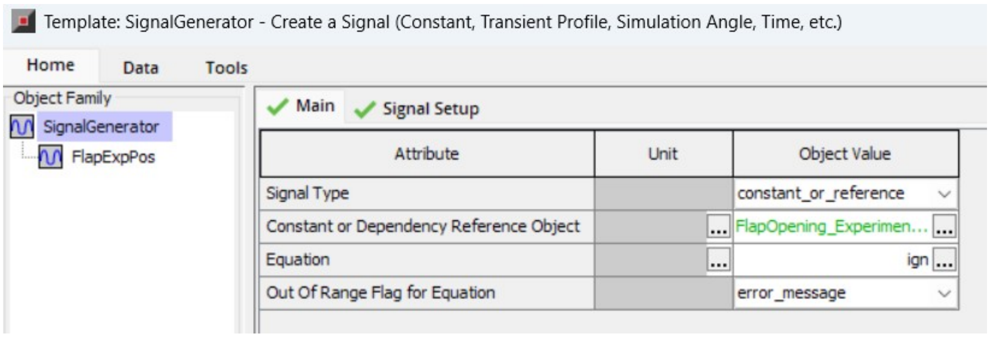

Figure 2.15: Object of the flap signal generator.

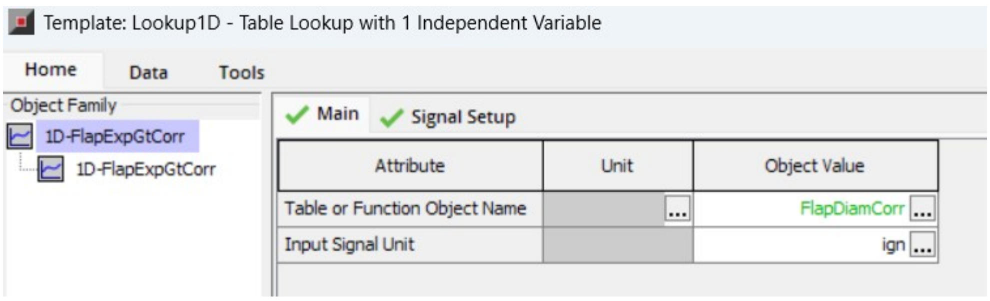

Figure 2.16: Object of the flap correlation.

2.1.5 Intercooler

A fundamental subsystem of the engine is the intercooler. The most important parts that compose it are two pipes, shown in Figure 4.21. Their setting layouts is similar to the one of intake and exhaust manifolds, but they are different objects. In fact, the manifolds are flow volumes, while the intercooler objects are pipes with circular cross section. Therefore the geometry options are different with respect to the manifolds ones. Here there is no need to specify the surface area and volume, but rather the diameters at inlet and outlet end, the length and the discretization length. The pipe is divided in many sub-volumes and in each one the solution quantities are computed. The length of each sub-volume is the discretization length. Instead, the pipe object exhibits the same settings of flow volumes about the thermodynamics, the material definition and the pressure drop. The intercooler has a proper set of material definition and thermodynamic properties. Finally, for what concerns the boundary data, they are not present within the pipe object, but are a feature of the flow volumes.

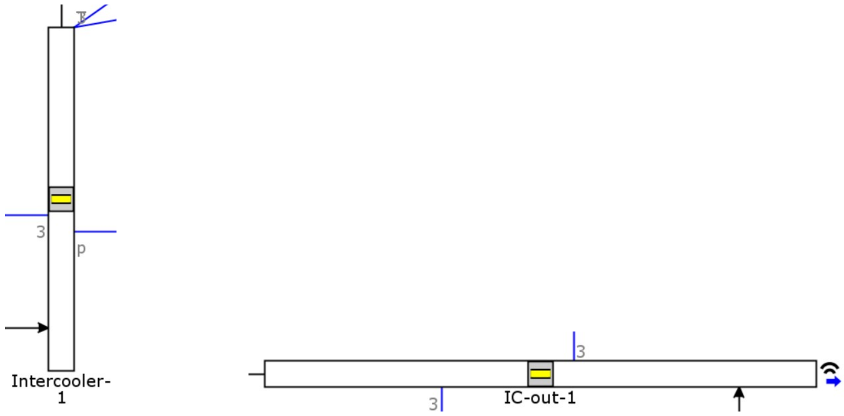

(a) (b)

Figure 2.17: Intercooler:**(a)** first pipe object; **(b)** second pipe object.

2.1.6 After Treatment System

The After Treatment System was shown at the beginning of the section, in Figure 2.3. It is a very complex system and only the basic structure and the main functioning will be explained. This system is composed by three main parts, arranged in the following order: the Diesel Oxidation Catalyst (DOC), the Diesel Particulate Filter (DPF), and the Selective Catalytic Reduction (SCR) device. The function of the ATS applied in this propulsion system is to reduce the two typical pollutant emission elements of the diesel engine: the nitrogen oxides (NOx) and the particulates. This ATS is optimized for the NOx reduction, thanks to a direct model-based controller, which uses the instantaneous value of the SCR efficiency.

2.2 Engine model without ATS

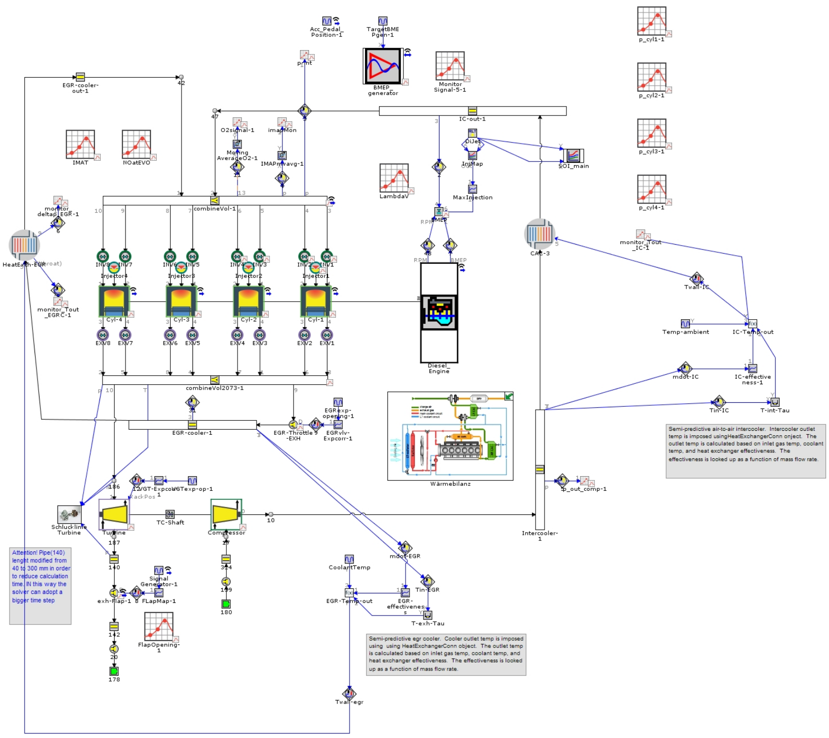

Figure 2.18: Engine model without ATS.

This section shows the engine model without ATS. As it can be seen in Figure 2.18, the following model seems simpler than the previous one. In fact, this configuration has not all the parts that compose the ATS and all the blocks reserved for the monitoring of the various quantities of the latter. The sub-systems that were described in the section of the engine model with ATS are present also in this model. So, all the previous explanation holds for this model too. However, there are some important differences between the two models, and one of the next chapter is reserved for a deep analysis of them. For now it is worth discussing only about a difference that can be noted just observing the model in Figure 2.18: the absence of the closed-loop controllers. In fact, it is possible to see that both EGR and VGT do not have a closed-loop system, but an open-loop chain, as the flap one. The structure is the same of the open-loop controller met about the flap valve, i.e. a signal generator followed by a correlation block and an actuator. The effect that these open-loop controllers have on the engine simulation will be accurately analyzed in the next chapters.

2.3 Simulation setup

The main work that can be done with the engine models is to run simulations and observe how much the quantities provided by the software differ from the experimental ones. Therefore, it is necessary to provide the same testing conditions of the experimental test bench. The test is based on the diagram shown in Figure 2.19. It is the Brake Mean Effective Pressure (BMEP) as a function of the engine rotational speed. There are 126 points and each one constitutes a specific steady-state test, so in the GT-SUITE language a specific case. The points cloud covers all the operational domain of the engine, including many load and speed levels.

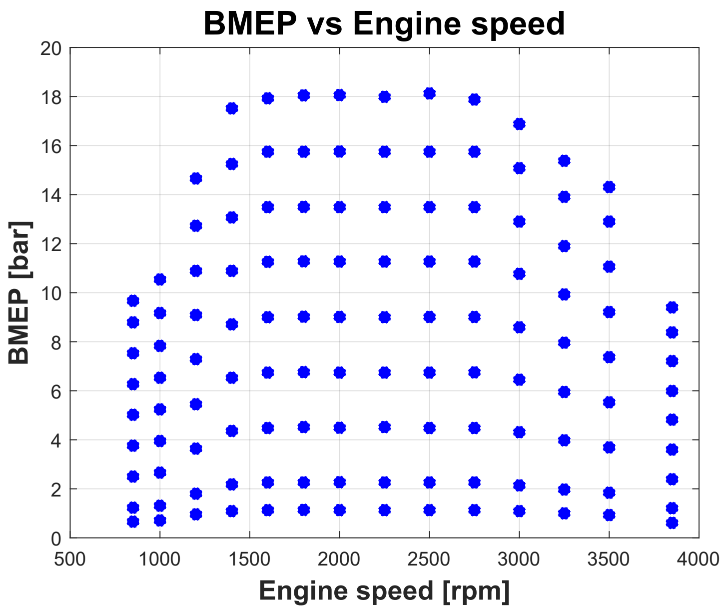

Figure 2.19: Operating points in the diagram of BMEP as a function of engine speed.

To observe more in detail the features of the entire series of tests, it can be useful to look at the diagram of the engine speed and BMEP as a function of the steady-state test number, reported in Figures 2.20(a) and 2.20(b) respectively. The test number represents the chronological order with which the steady-state tests were performed. For what concerns the engine speed, it is included in a range from 850 rpm to 3850 rpm, and different intermediate values were taken. The logic is to start from the maximum value and then decrease until the minimum one, repeating this execution nine times. About the corresponding BMEP values, it is possible to observe that many tests were carried out at precise load levels, and this can be noted looking at the almost horizontal trends in Figure 2.19. From a chronological point of view, at the beginning there are high loads, for then going to medium levels, and finally concluding with the lowest ones.

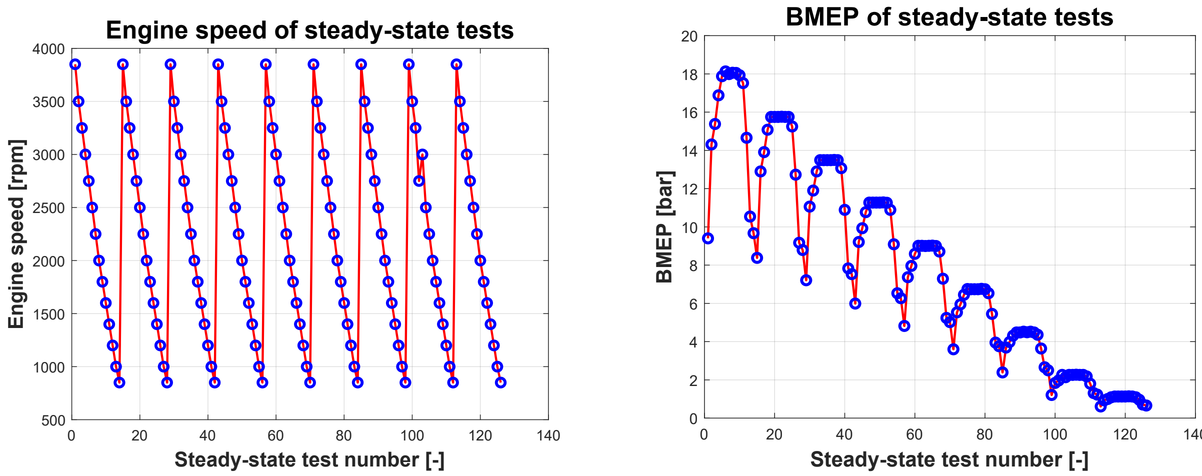

(a) (b)

Figure 2.20: Operating points of the engine speed **(a)** and BMEP **(b)** as a function of the test number.

2.4 Initial simulations

This section shows the analysis of the initial simulations results. The GT-POST environment is exploited, in which every simulation runs and once the run is finished it is possible to visualize the outcomes of all the engine quantities. The data of the quantities considered are exported from GT-POST to Microsoft Excel, where they are collected in tables. Then, to obtain all the related plots, Matlab is used. Before observing the results, it is necessary to explain the method that is used for their analysis and specify which quantities have been selected.

2.4.1 Analysis method

The aim of the results post-processing, as it was stated in the previous section, is to compare the simulation outcomes with the experimental ones. For every selected quantity, two plots can be exploited. The first one shows the chosen quantity as a function of the case number, meaning that the number of the steady-state test. In this chart there are two trends, i.e. the experimental one and the simulated one. The second type of plot exhibits the experimental quantity in the abscissa, while the simulated one in the ordinate. Hence, a cloud of points can be obtained, and a single point is a specific steady-state test. In this diagram two important parameters are reported, very crucial for a quantitative comparison between the experimental and the simulated results: the Squared Correlation Coefficient R^2 and the Root Mean Square Error $RMSE$. The first is defined by equation 2.2.

$$R^2 = \frac{\sum_k \sum_q (A_{kq} - \bar{A})(B_{kq} - \bar{B})}{\sqrt{\sum_k \sum_q (A_{kq} - \bar{A})^2 (B_{kq} - \bar{B})^2}} \tag{2.2}$$

where:

$$\bar{A} = \frac{\sum_{i=1}^{n} A_i}{n} \tag{2.3}$$

$$\bar{B} = \frac{\sum_{i=1}^{n} A_i}{n} \tag{2.4}$$

It is possible to note that A and B are two matrices, both with dimension $k \times q$. However, in this case, they are algebraic vectors, with dimension $n \times 1$, where $n = 126$, i.e. the number of steady-state tests. In fact, A is the vector of the experimental values of the quantity considered, while B

is the vector of the corresponding simulated values. Therefore, referring to the R^2 formulation, A and B are two column vectors, with $k = n = 126$ and $q = 1$.
$\bar{A}$ and $\bar{B}$ are the arithmetic averages of A and B vectors, as it can be observed in the relations 2.3 and 2.4.
Concerning the Root Mean Square Error ($RMSE$), it is defined by the formulation 2.5, where A and B are the same vectors considered in the R^2 definition.

$$RMSE = \sqrt{\frac{1}{n}\sum_{i=1}^{n}|B_i - A_i|^2} \tag{2.5}$$

In all the plots where these two parameters are numerically shown, the corresponding Matlab functions are exploited, "$corr2$" [5] for R^2 and "$rmse$" [6] for $RMSE$. 2.2 and 2.5 are mathematical definitions of the Squared Correlation Coefficient and the Root Mean Square Error. From a concept point of view, these two parameters indicate how much the simulated quantity differs from the experimental one, in terms of correlation, provided by R^2, and in terms of numerical difference, given by $RMSE$. The square correlation coefficient has a range from -1 to 1, and if it increases it means that there is a better correlation between the simulated and experimental quantity. Instead, the $RMSE$ provides values that can go from zero to infinite and if it decreases it means that the simulated quantity is closer to the experimental one.

2.4.2 Analyzed quantities

It is necessary to select the main engine quantities to perform the analysis. The list of these quantities, whose names are directly those of department dictionary, is reported:

- *FB_VAL*: average fuel consumption during the test;
- *mairwet*: wet air mass flow rate;
- *mairdry*: dry air mass flow rate;
- *BMEP*: brake mean effective pressure;
- *p_MAP_Abs*: intake manifold absolute pressure;
- *T_IM_avg*: intake manifold average temperature;
- *p_ExbTC_Abs*: absolute pressure of turbine upstream exhaust gases (exhaust manifold absolute pressure);
- *T_EM_avg*: exhaust manifold average temperature;
- *p_ExaTC_Abs*: absolute pressure of turbine downstream exhaust gases;
- *T_ExaTC*: temperature of turbine downstream exhaust gases;
- *PMAXi*: maximum pressure of cylinder i combustion chamber;
- *IMEPi*: net indicated mean effective pressure of cylinder i;
- *IMEPHi*: gross indicated mean effective pressure of cylinder i;
- *IMEPLi*: pumping mean effective pressure of cylinder i;
- *TFMEPi*: total friction mean effective pressure of cylinder i;
- *N_turbo*: turbo angular speed;
- *Xr_CO2*: EGR percentage;

- *PCR_pDesVal*: boost pressure;

The goal is to obtain an initial overview of the main engine quantities. In the next chapters further quantities will be analyzed, to go more in detail and improve as much as possible such overview. However, for now the listed quantities will be examined.

2.4.3 Initial simulation of the engine model with ATS

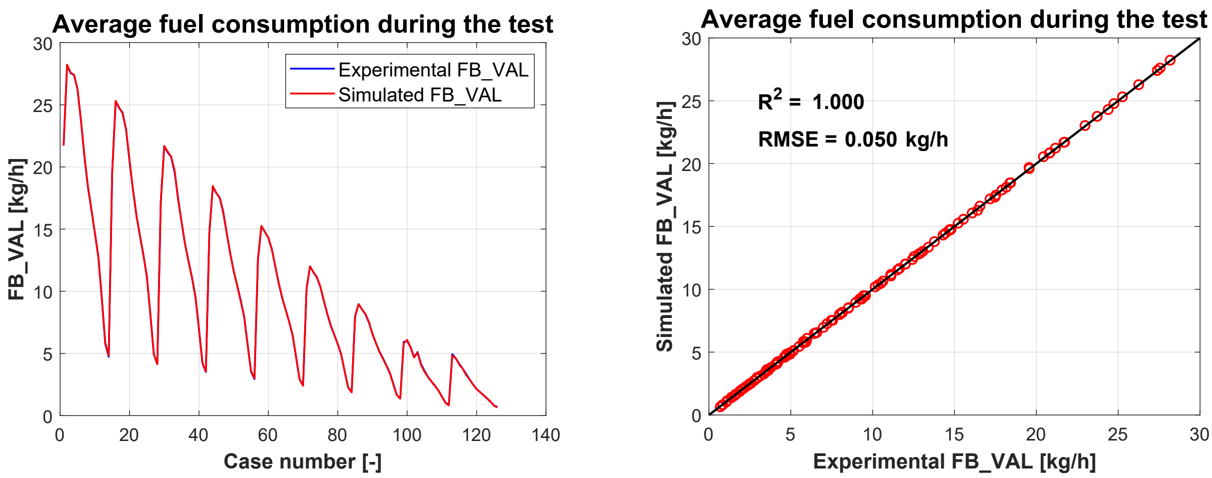

(a) (b)

Figure 2.21: Average fuel consumption during the test of engine model with ATS: **(a)** experimental *FB_VAL* and simulated *FB_VAL* as a function of the case number; **(b)** bisector plot of experimental *FB_VAL* and simulated *FB_VAL*.

Starting with the engine model with ATS, the results of the initial simulation can be observed. No modification has been introduced within the GT-ISE model, and the aim is to look at the behavior of the simulated quantities. The first is the average fuel consumption during the test *FB_VAL*, reported in Figure 2.21. It can be immediately noticed that the experimental and simulated trends overlap, reaching a very good level of correlation and a very small value of $RMSE$. This actually is due to the imposition of the experimental injected fuel mass per pulse inside the injector object of GT-ISE model, which leads to have a simulated fuel flow rate roughly equal to the experimental one.
Subsequently, it is possible to observe the wet and dry air mass flow rates, shown respectively in Figure 2.22 and 2.23. The comparison between the simulated and experimental trend, both for wet and dry air mass flow rates, gives very good results. GT-POST gives only a type of air mass flow rate, which does not take into account the humidity. So, the air mass flow rate provided by GT-POST must be considered as the total air mass flow rate, which in reality coincides with the wet air mass flow rate and must be compared with the latter. Therefore, the simulated dry air mass flow rate must be computed, and this can be carried out using the relation 2.6.

$$mairdry\left[\frac{g}{s}\right] = \frac{mairwet\left[\frac{kg}{h}\right]}{3.6} - \frac{mairwet\left[\frac{kg}{h}\right]\cdot H_{abs,avg}\left[\frac{g}{kg}\right]}{3600} \tag{2.6}$$

The term $H_{abs,avg}$ is the average absolute humidity, obtained by performing the arithmetic average of the absolute humidity vector, present in the experimental data sheet. This array includes the experimental values of the absolute humidity case by case, so it has dimension 126×1. However, the values between the cases do not differ much, so it is suitable to rely on an arithmetic average.

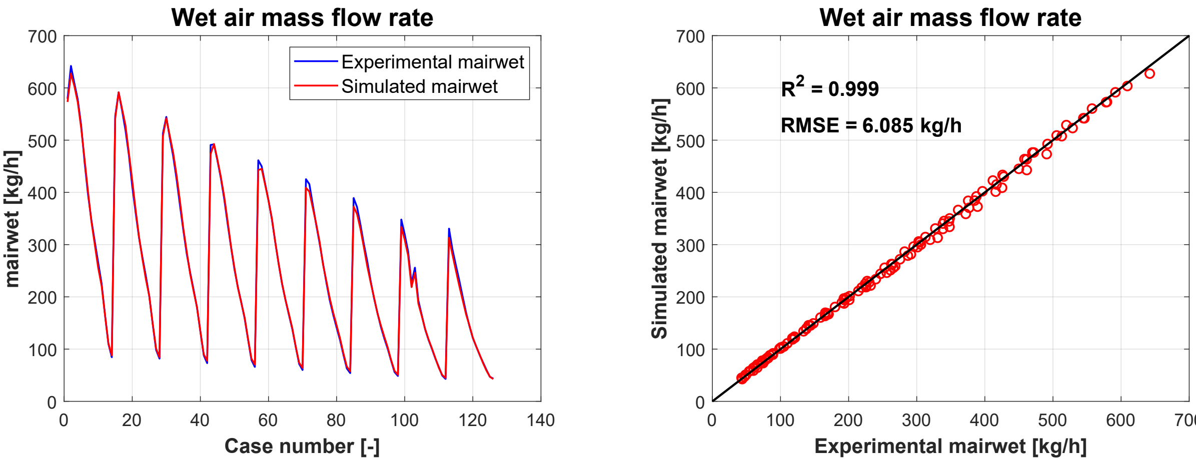

(a) (b)

Figure 2.22: Wet air mass flow rate of engine model with ATS: **(a)** experimental *mairwet* and simulated *mairwet* as a function of the case number; **(b)** bisector plot of experimental *mairwet* and simulated *mairwet*.

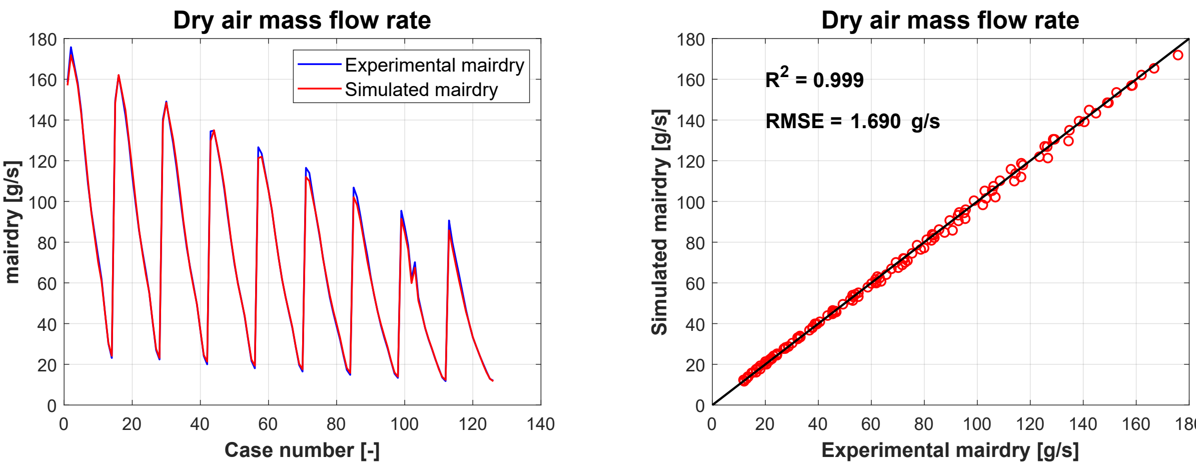

(a) (b)

Figure 2.23: Dry air mass flow rate of engine model with ATS: **(a)** experimental *mairdry* and simulated *mairdry* as a function of the case number; **(b)** bisector plot of experimental *mairdry* and simulated *mairdry*.

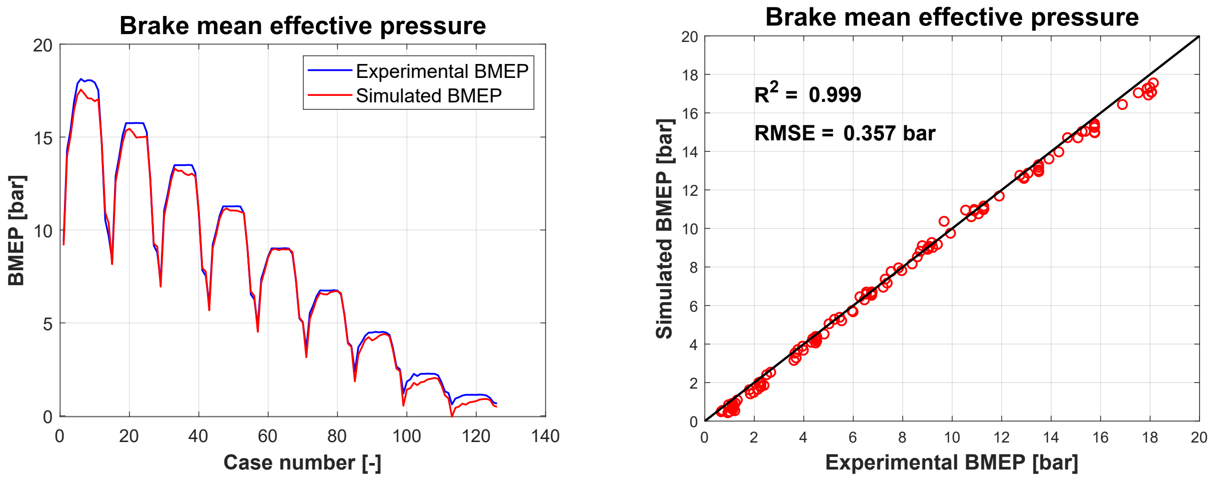

(a) (b)

Figure 2.24: Brake mean effective pressure of engine model with ATS: **(a)** experimental *BMEP* and simulated *BMEP* as a function of the case number; **(b)** bisector plot of experimental *BMEP* and simulated *BMEP*.

Another important quantity to analyze is the Brake Mean Effective Pressure (BMEP), shown in Figure 2.24. It globally follows the corresponding experimental data in an acceptable manner. The only aspect is that, at high loads, there is a slight underestimation. Actually, also at the lowest loads, the simulated *BMEP* is lower than the experimental one, but the difference is minor. Now, the thermodynamic quantities related to the intake manifold must be analyzed, i.e. the absolute pressure and the average temperature. The first is reported in Figure 2.25, where it is possible to note that there is a very good behavior of the simulated trend. Instead, observing the intake manifold temperature in Figure 2.26, the simulated plot does not follow in a good way the experimental trend. This is probably due to the effect of EGR, which determines a more complex thermodynamics of the intake manifold gases, difficult to model.

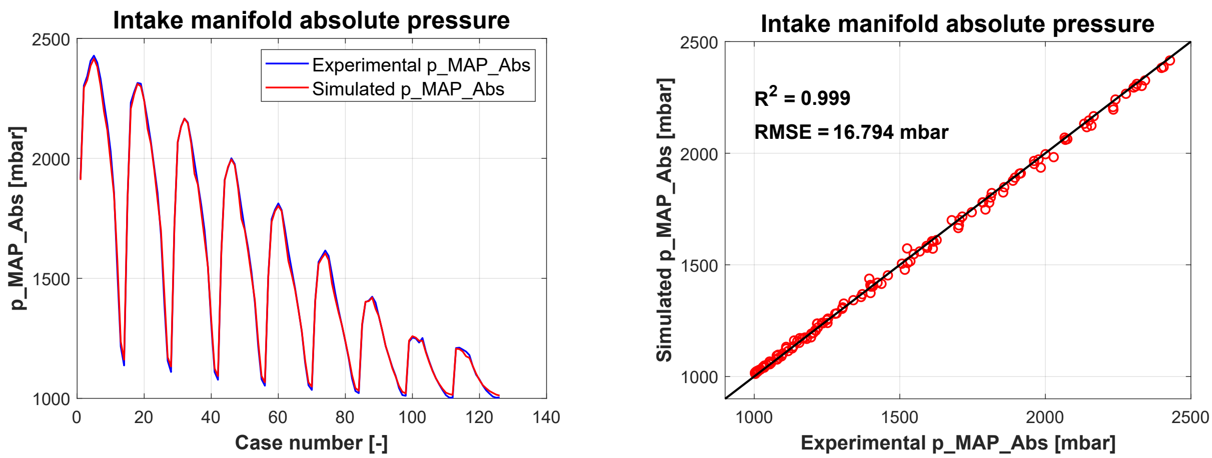

(a) (b)

Figure 2.25: Intake manifold absolute pressure of engine model with ATS: **(a)** experimental *p_MAP_Abs* and simulated *p_MAP_Abs* as a function of the case number; **(b)** bisector plot of experimental *p_MAP_Abs* and simulated *p_MAP_Abs*.

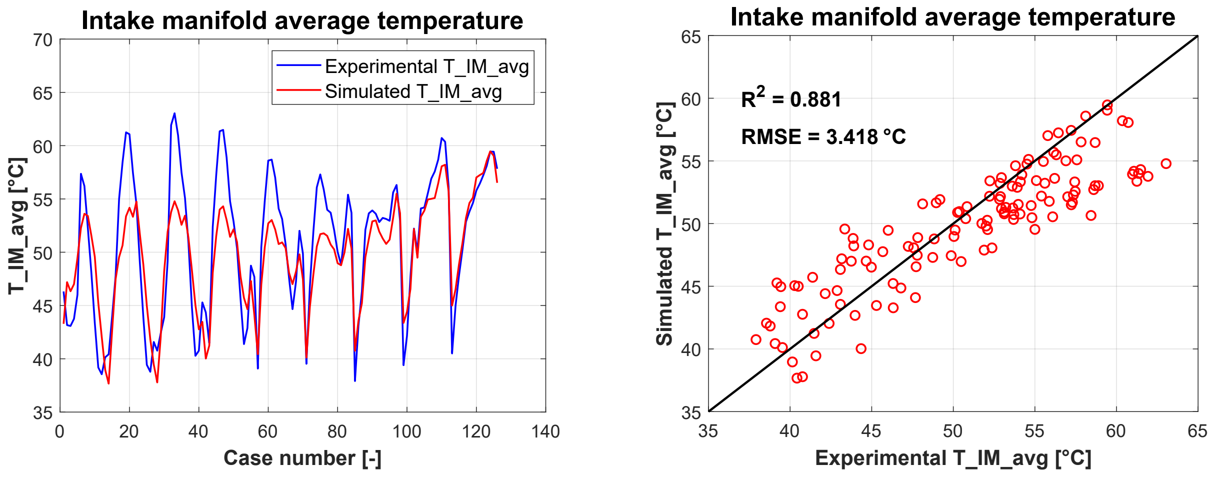

(a) (b)

Figure 2.26: Intake manifold average temperature of engine model with ATS: **(a)** experimental *T_IM_avg* and simulated *T_IM_avg* as a function of the case number; **(b)** bisector plot of experimental *T_IM_avg* and simulated *T_IM_avg*.

In terms of the thermodynamic quantities inside the exhaust manifold, hence the absolute pressure and the average temperature of the exhaust manifold, they are shown respectively in Figure 2.27 and Figure 2.28. Regarding the absolute pressure, it is possible to note that there is an overestimation of this quantity by the engine model, in particular on the upper peaks, for each load level. In fact, this is confirmed by looking at the $RMSE$ value, which is quite high. In contrast, the simulated average temperature of the exhaust manifold is much closer to the experimental values. In some parts of the diagram there is a slight overestimation, while in others an underestimation. The reason for this inconsistency between the behaviors of the pressure and the temperature inside the exhaust manifold will be explained in more depth in the next chapters.

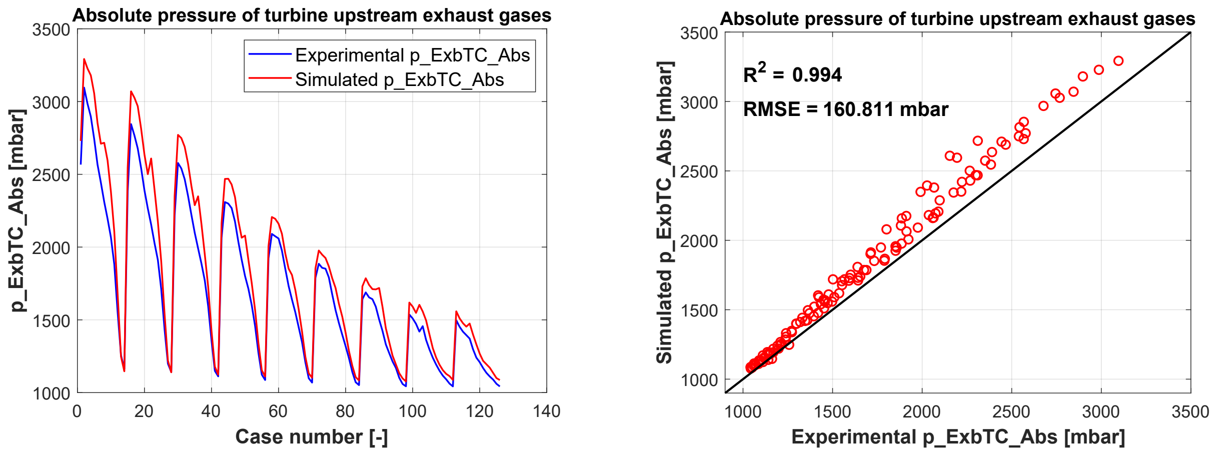

(a) (b)

Figure 2.27: Absolute pressure of turbine upstream exhaust gases of engine model with ATS: **(a)** experimental *p_ExbTC_Abs* and simulated *p_ExbTC_Abs* as a function of the case number; **(b)** bisector plot of experimental *p_ExbTC_Abs* and simulated *p_ExbTC_Abs*.

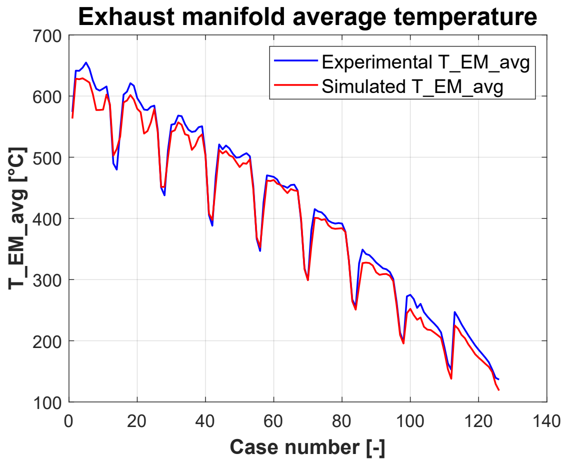

(a)

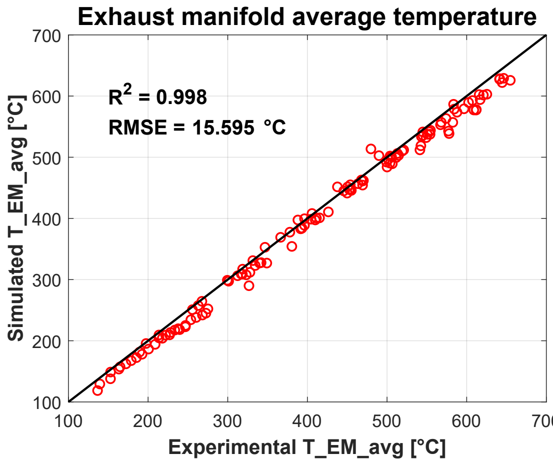

(b)

Figure 2.28: Exhaust manifold average temperature of engine model with ATS: **(a)** experimental *T_EM_avg* and simulated *T_EM_avg* as a function of the case number; **(b)** bisector plot of experimental *T_EM_avg* and simulated *T_EM_avg*.

The Figures 2.29 and 2.30 show respectively the absolute pressure and the average temperature of the exhaust gases at turbine downstream. The first quantity exhibits better behavior than the absolute pressure of the gases inside the exhaust manifolds, as it can be seen by looking at the $RMSE$ value, which is lower. On the peaks at high loads there is a slight overestimation, but globally the simulated quantity follows in a good manner the experimental trend. Regarding the temperature, the same reasoning carried out for the temperature of the exhaust manifold gases holds.

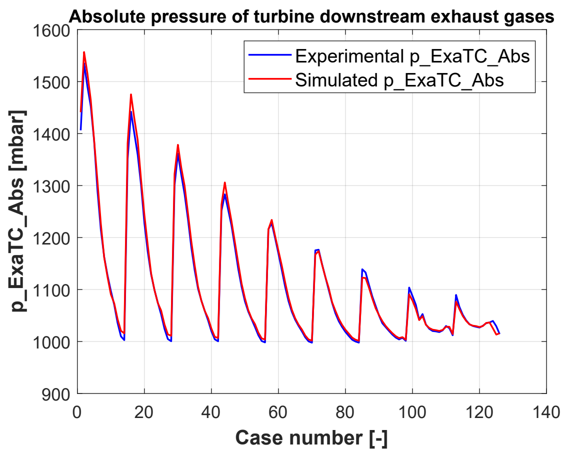

(a)

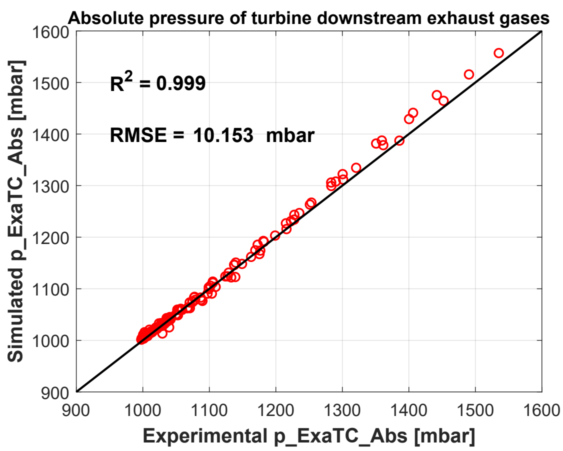

(b)

Figure 2.29: Absolute pressure of turbine downstream exhaust gases of engine model with ATS: **(a)** experimental *p_ExaTC_Abs* and simulated *p_ExaTC_Abs* as a function of the case number; **(b)** bisector plot of experimental *p_ExaTC_Abs* and simulated *p_ExaTC_Abs*.

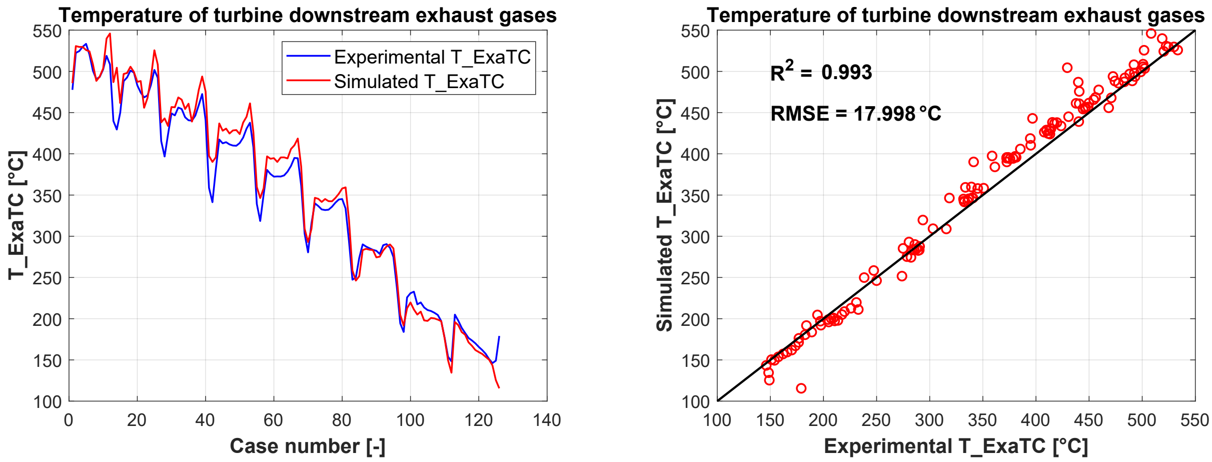

(a) (b)

Figure 2.30: Temperature of turbine downstream exhaust gases of engine model with ATS: **(a)** experimental *T_ExaTC* and simulated *T_ExaTC* as a function of the case number; **(b)** bisector plot of experimental *T_ExaTC* and simulated *T_ExaTC*.

Now, it is necessary to analyze the quantities related to the single cylinder. For all the cylinders the quantities were explored, but in this thesis only the ones related to the third cylinder are shown, due to their better behavior in following the experimental trends. It must be specified that the R^2 and $RMSE$ values do not differ so much from each other, but the third cylinder gives the best results and so it is worth analyzing them. First of all, there is the maximum pressure inside the combustion chamber, reported in Figure 2.31. A certain underestimation can be seen on the upper peaks at high loads, bringing gaps of also 10 bar. This difference reduces with the next engine model. Then the net indicated mean effective pressure is illustrated in Figure 2.32. It is worth remembering what is this quantity: it is the integral of the in-cylinder pressure signal over the entire cycle. Hence, thinking in terms of crank angle and considering that the engine studied is four-stroke, it coincides with the subtended area of the pressure plot as a function of the crank angle from 0 $°CA$ to 720 $°CA$.
It can be noticed that at high loads there is an underestimation of the *IMEP*.

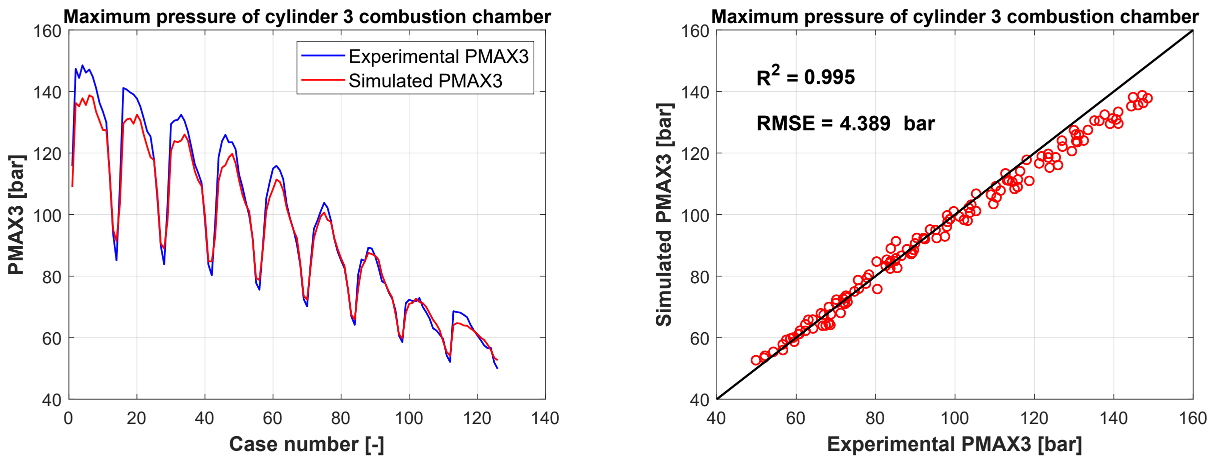

(a) (b)

Figure 2.31: Maximum pressure of cylinder 3 combustion chamber of engine model with ATS: **(a)** experimental *PMAX3* and simulated *PMAX3* as a function of the case number; **(b)** bisector plot of experimental *PMAX3* and simulated *PMAX3*.

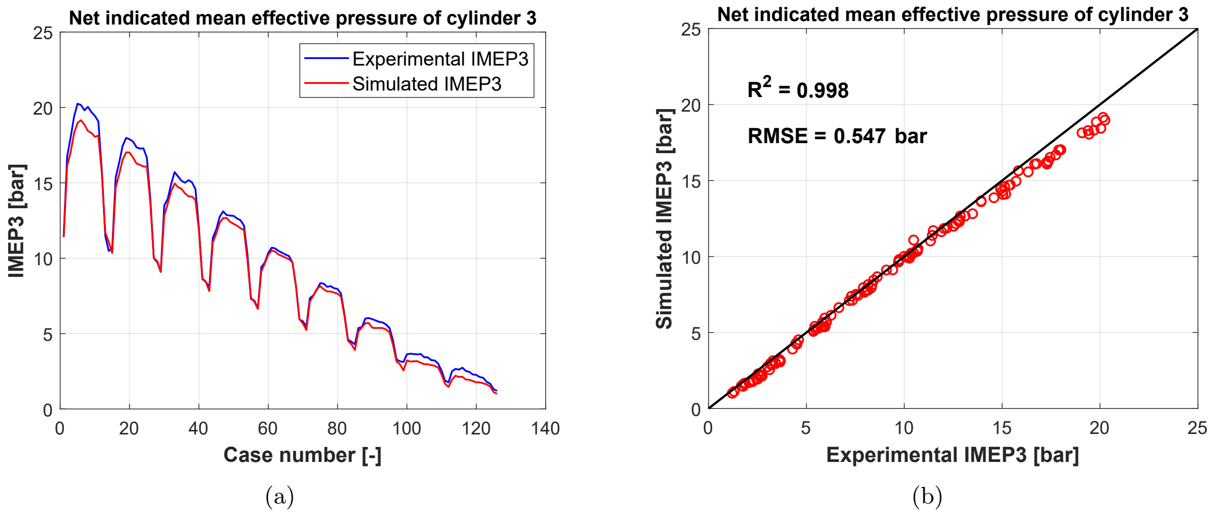

Figure 2.32: Net indicated mean effective pressure of cylinder 3 of engine model with ATS: **(a)** experimental *IMEP3* and simulated *IMEP3* as a function of the case number; **(b)** bisector plot of experimental *IMEP3* and simulated *IMEP3*.

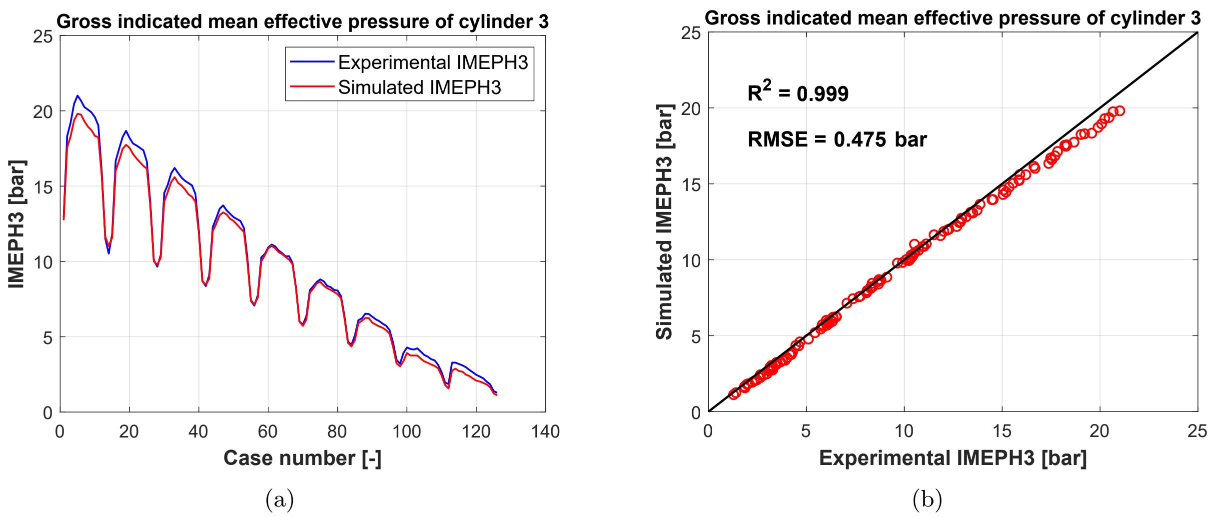

Figure 2.33: Gross indicated mean effective pressure of cylinder 3 of engine model with ATS: **(a)** experimental *IMEPH3* and simulated *IMEPH3* as a function of the case number; **(b)** bisector plot of experimental *IMEPH3* and simulated *IMEPH3*.

In Figure 2.33 the gross indicated mean effective pressure of cylinder 3 is shown. This type of mean effective pressure coincides with the subtended area of the in-cylinder pressure signal over the compression and expansion phases. Hence, thinking again in terms of crank angle, it is the integral of the in-cylinder pressure as a function of the crank angle from $180°CA$ to $540°CA$. This quantity is linked to the net indicated mean effective pressure. In fact, the relation for Turbo-Charged four-stroke engines (2.7) holds.

$$IMEP = IMEPH + IMEPL \tag{2.7}$$

where *IMEPL* represents the pumping losses and it is defined as the integral of the in-cylinder pressure signal as a function of the crank angle over the intake and exhaust phases, i.e. in the ranges $0°CA$ - $180°CA$ (intake) and $540°CA$ - $720°CA$ (exhaust). This quantity will be examined in the next Figure. Concluding with the *IMEPH*, it is expected to have the same behavior of the *IMEP* and, in fact, the simulated trend is lower than the experimental one at higher loads.

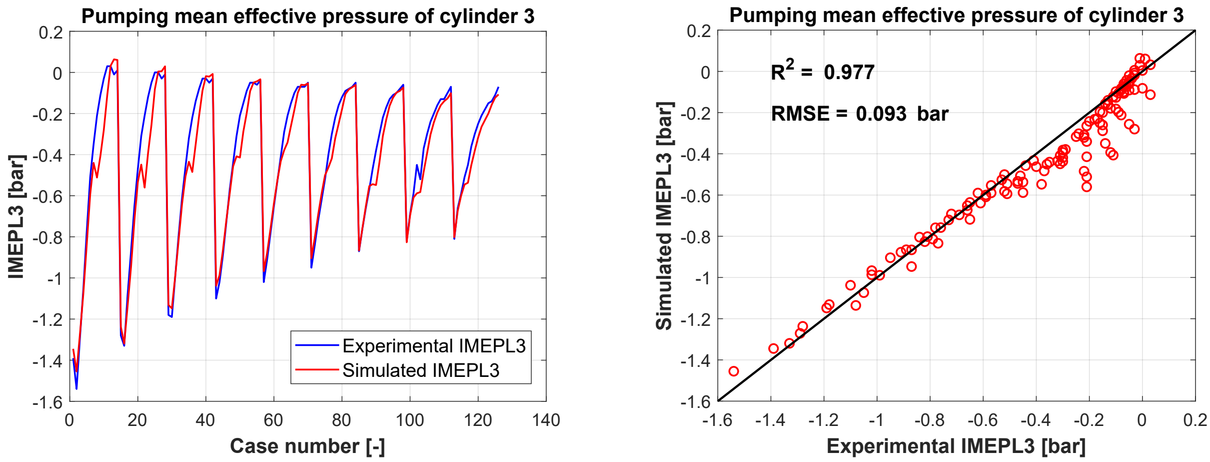

(a) (b)

Figure 2.34: Pumping mean effective pressure of cylinder 3 of engine model with ATS: **(a)** experimental *IMEPL3* and simulated *IMEPL3* as a function of the case number; **(b)** bisector plot of experimental *IMEPL3* and simulated *IMEPL3*.

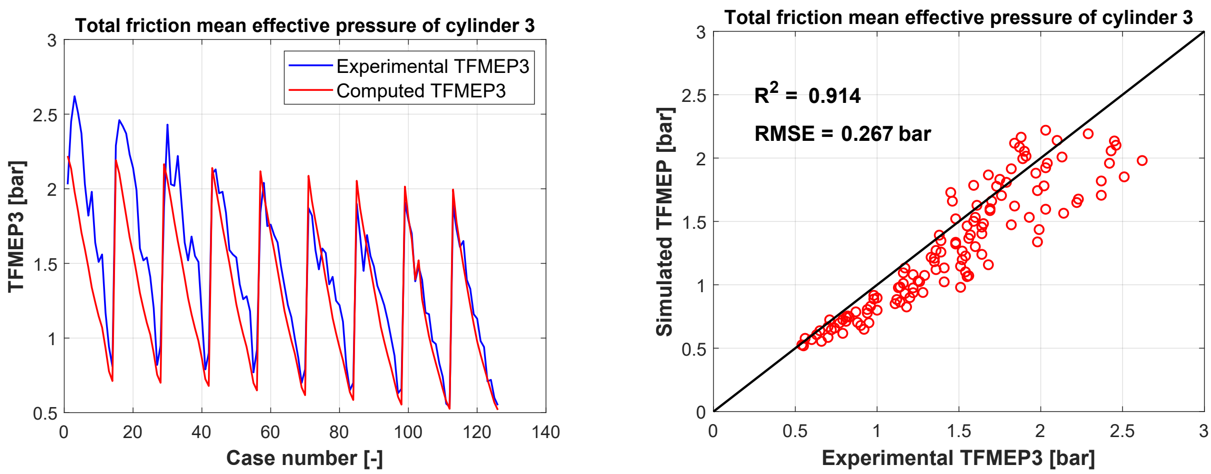

(a) (b)

Figure 2.35: Total friction mean effective pressure of cylinder 3 of engine model with ATS: **(a)** experimental *TFMEP3* and simulated *TFMEP3* as a function of the case number; **(b)** bisector plot of experimental *TFMEP3* and simulated *TFMEP3*.

The pumping mean effective pressure *IMEPL* is reported in Figure 2.34 and it is possible to note that in most cases the simulated trend is lower than the experimental one. There is a slight overestimation only in the upper peaks at higher loads.
Concerning the total friction mean effective pressure *TFMEP*, it is necessary to explain the method with which the experimental quantity was computed. The reference relations are always the ones of the Turbo-Charged four-stroke engine, given by 2.8 and 2.9.

$$TFMEP = MFMEP + AMEP \tag{2.8}$$

$$BMEP = IMEP - TFMEP \tag{2.9}$$

$$TFMEP = IMEP - BMEP \tag{2.10}$$

The *TFMEP* is made up of two contributions, i.e. the mechanical friction and the contribution of the accessories, e.g. pumps, camshafts, alternator etc. In fact, MFMEP means Mechanical Friction Mean Effective Pressure and AMEP Accessory Mean Effective Pressure. By 2.9 it is also possible to know the link between the *BMEP* and the *IMEP*. The difference between them is precisely the total friction mean effective pressure. Therefore, the experimental *TFMEP* can be computed by subtracting to the experimental *IMEP* the experimental *BMEP* (2.10). Instead, GT-SUITE provides the friction mean effective pressure using the Chenn-Flynn model, as it was illustrated in one of the previous sections. It expresses the dependence of the friction on the engine speed. In fact, if the engine speed graph in Figure 2.20(a) is observed, it has the same trend of the simulated *TFMEP3*.

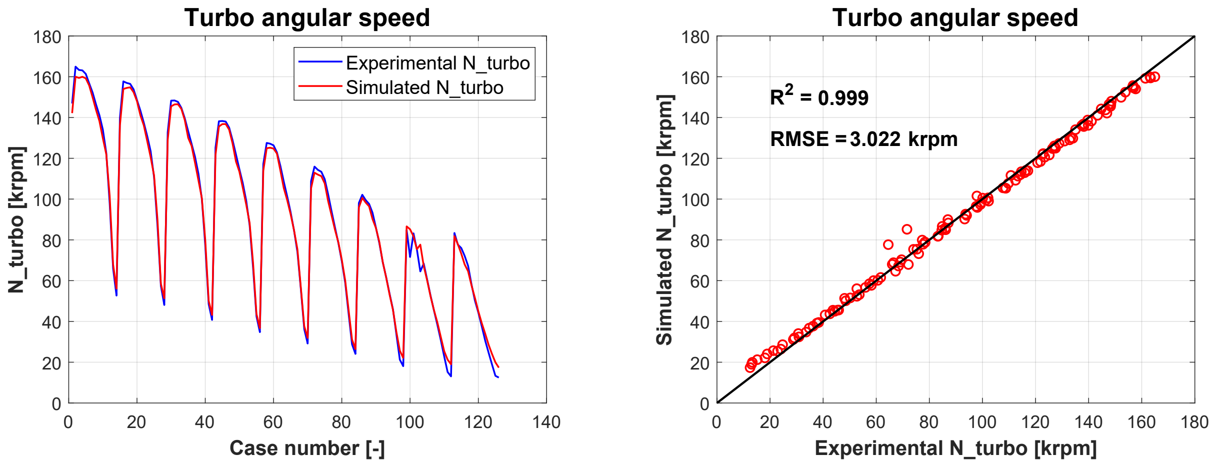

(a) (b)

Figure 2.36: Turbo angular speed of engine model with ATS: **(a)** experimental *N_turbo* and simulated *N_turbo* as a function of the case number; **(b)** bisector plot of experimental *N_turbo* and simulated *N_turbo*.

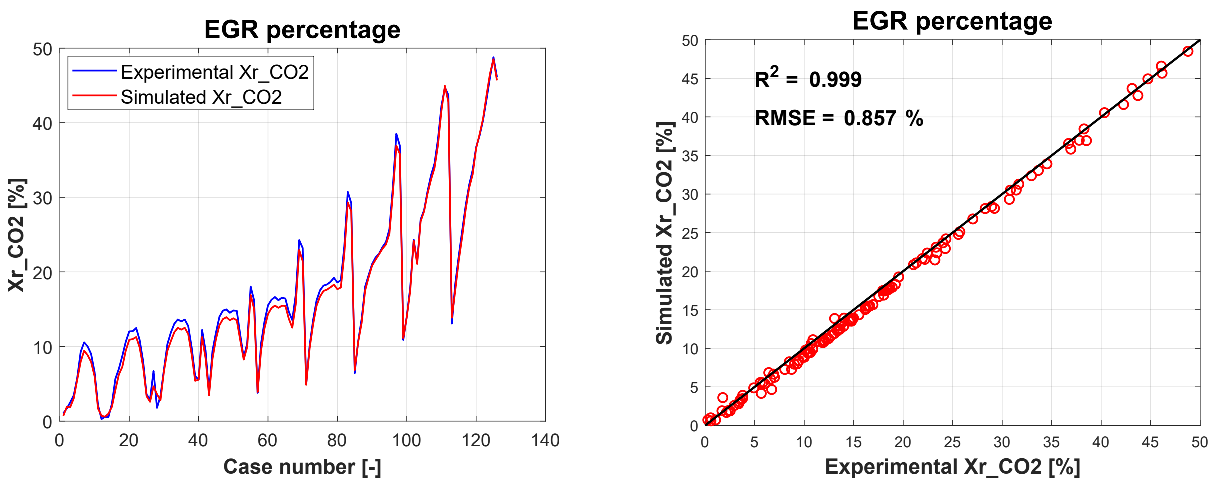

(a) (b)

Figure 2.37: EGR percentage of engine model with ATS: **(a)** experimental *Xr_CO2* and simulated *Xr_CO2* as a function of the case number; **(b)** bisector plot of experimental *Xr_CO2* and simulated *Xr_CO2*.

All the most important quantities about the single cylinder have been shown. The next quantity concerns the turbo group and it is the turbo angular speed *N_turbo*, shown in Figure 2.36. In most cases, there is good accuracy about the prediction of the experimental results.
Another relevant quantity is the percentage of Exhaust Gas Recirculation, reported in Figure 2.37. There is a satisfactory behavior of the simulated quantity, thanks to the presence of the closed-loop controller. Furthermore, it is interesting to note that as the load decreases the EGR percentage enhances. In fact, for high loads a fast combustion is needed, and the EGR effect is detrimental for the combustion velocity. Therefore, in the initial cases where the load is high, the EGR percentage must be low.
The last quantity is the boost pressure *PCR_pDesVal* and can be seen in Figure 2.38. The simulated boost pressure follows in a very good manner the experimental one and the trend is very similar to the absolute pressure inside the intake manifold. In fact, the boost pressure is the pressure at the intercooler outlet, directly connected to the intake manifold. In this case the relative boost pressure is taken into account, to isolate and observe the boost effect provided by the turbo group. The very good estimate of the experimental results is due to the presence of the closed-loop controller of the VGT.

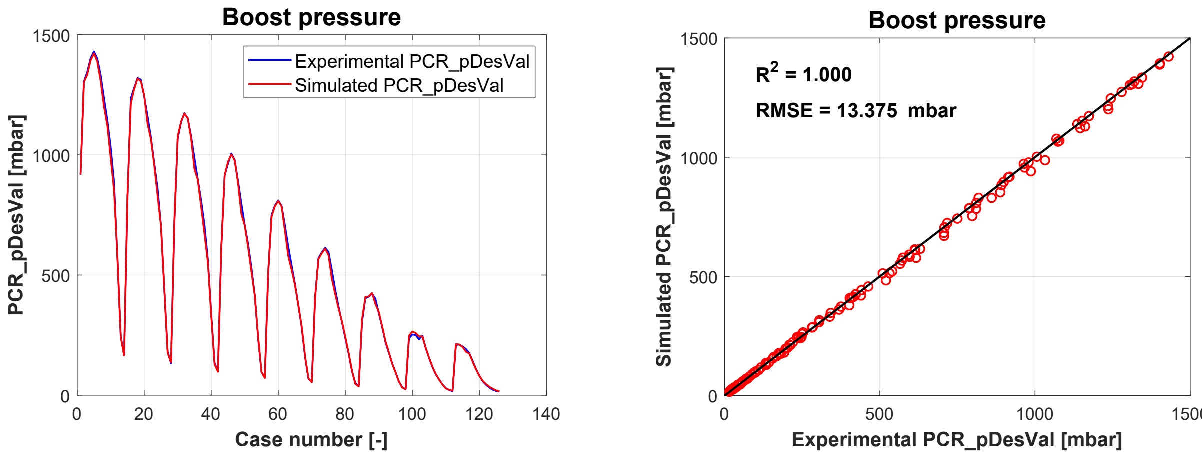

(a) (b)

Figure 2.38: Boost pressure of engine model with ATS: **(a)** experimental *PCR_pDesVal* and simulated *PCR_pDesVal* as a function of the case number; **(b)** bisector plot of experimental *PCR_pDesVal* and simulated *PCR_pDesVal*.

2.4.4 Initial simulation of the engine model without ATS

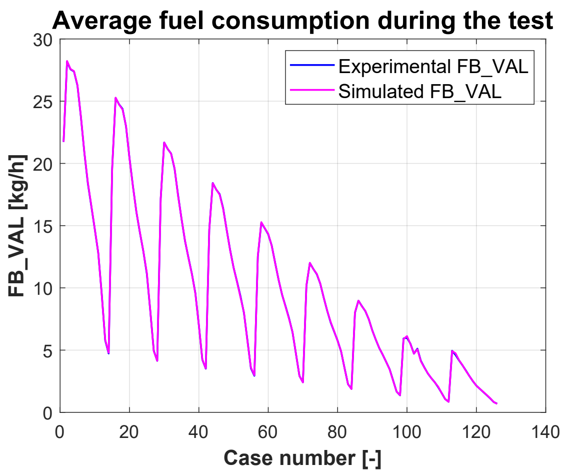

(a)

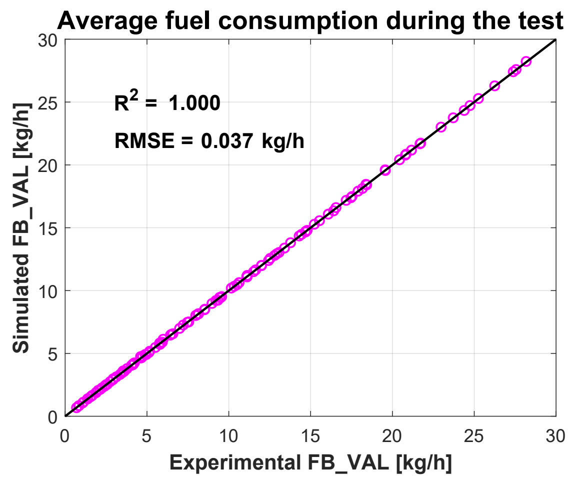

(b)

Figure 2.39: Average fuel consumption during the test of engine model without ATS: **(a)** experimental *FB_VAL* and simulated *FB_VAL* as a function of the case number; **(b)** bisector plot of experimental *FB_VAL* and simulated *FB_VAL*.

A starting simulation was also run for the engine model without ATS and the same quantities of the previous engine model are analyzed now.
The first quantity is again the average fuel consumption during the test, which, as it is possible to observe in Figure 2.39, shows an almost perfect behavior of the simulated quantity with respect to the experimental one. This occurs because the experimental injected mass per pulse is imposed inside the injector block of the engine model.
Observing then the wet and dry air mass flow rates (Figures 2.40 and 2.41), there is a slightly worse behavior than the case of the engine model with ATS. In fact the *RMSE* values are higher. The reason of this is the absence of the closed-loop control of EGR. There is an open-loop chain, well calibrated, but that cannot reach the precision of a closed-loop controller.

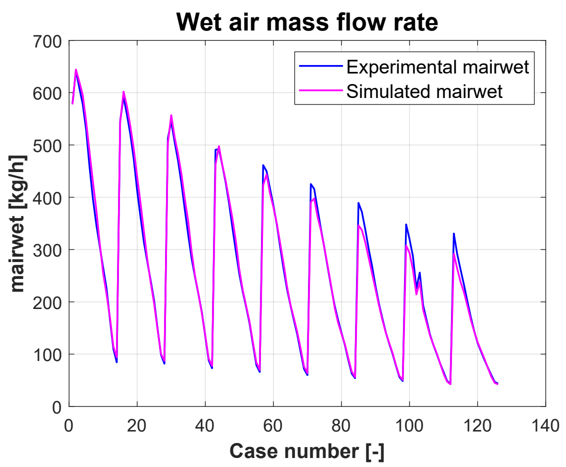

(a)

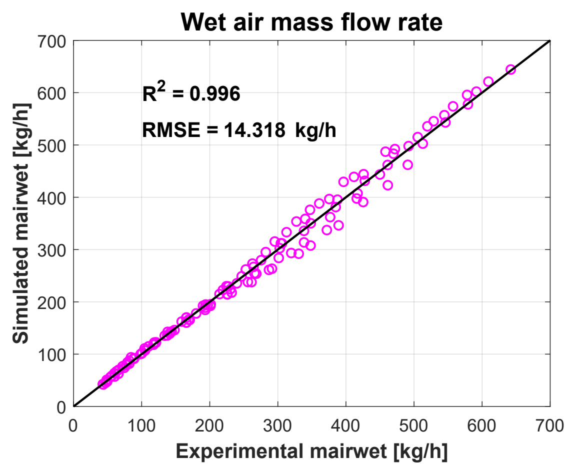

(b)

Figure 2.40: Wet air mass flow rate of engine model without ATS: **(a)** experimental *mairwet* and simulated *mairwet* as a function of the case number; **(b)** bisector plot of experimental *mairwet* and simulated *mairwet*.

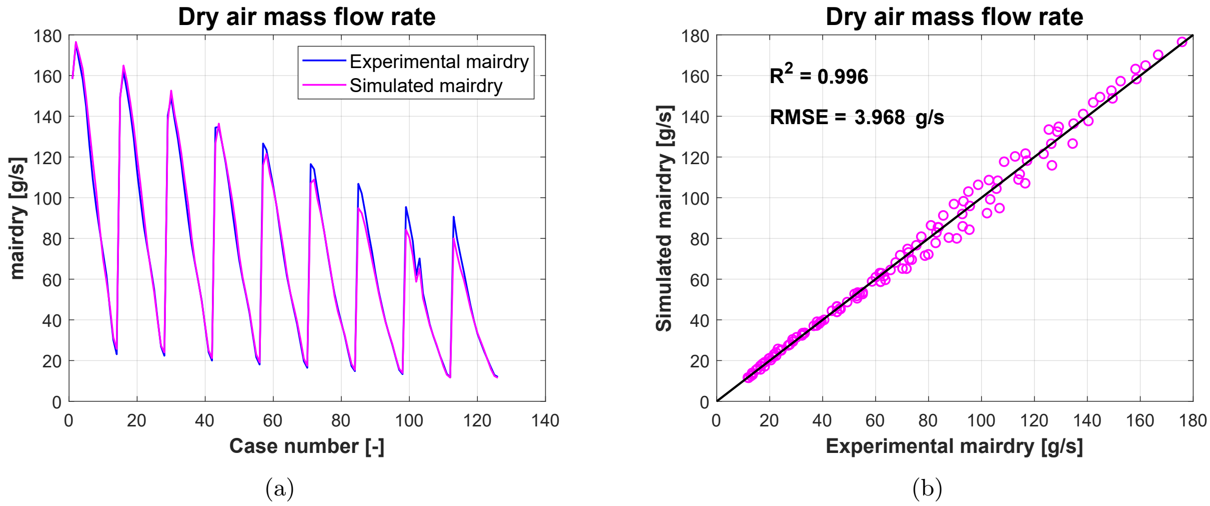

Figure 2.41: Dry air mass flow rate of engine model without ATS: **(a)** experimental *mairdry* and simulated *mairdry* as a function of the case number; **(b)** bisector plot of experimental *mairdry* and simulated *mairdry*.

Regarding the *BMEP*, shown in Figure 2.42, an improvement can be seen about the prediction accuracy of the experimental trend. This engine model is optimized for some quantities, and one of these is the *BMEP*. In the next chapters, the feature which guarantees this improvement will be carefully explained.
The thermodynamic quantities of the intake manifold are reported in Figures 2.43 and 2.44. About the absolute pressure, the simulated *p_MAP_Abs* follows in a worse manner the experimental results than in the previous engine model. The reason is the absence of the closed-loop control of the VGT, which leads to an overestimation at high loads and an underestimation at low loads. The *T_IM_avg* shows as before a difficulty in estimating the experimental results, as can be also observed in the graph on the right, where the cloud of points is very dispersed around the bisector. Actually, there is a further slight worsening with respect to the previous model, but considering this result in proportion with the scale of values covered by this temperature, it is not such a low quality result.

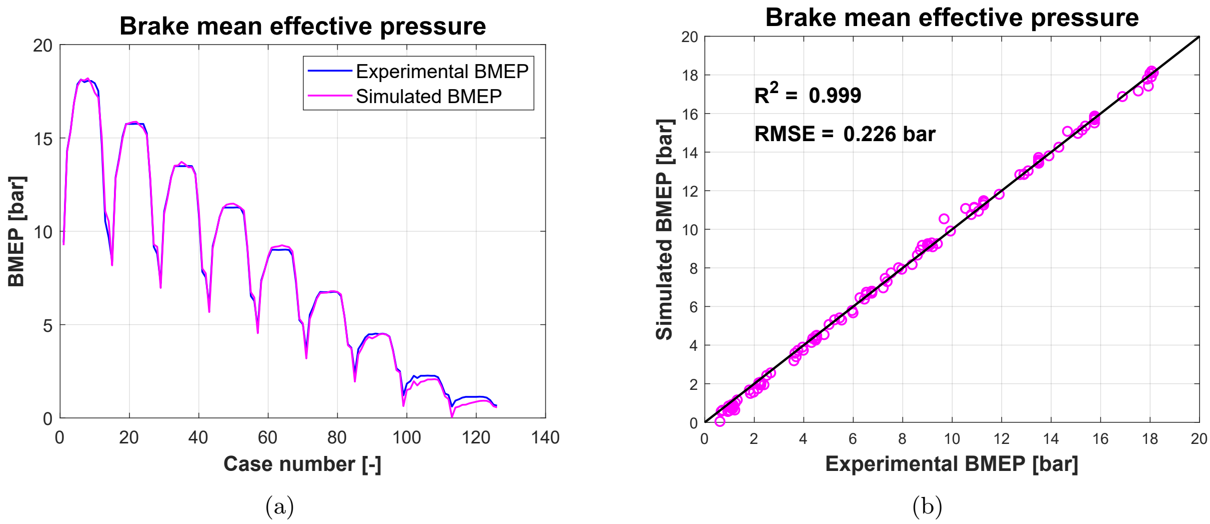

Figure 2.42: Brake mean effective pressure of engine model without ATS: **(a)** experimental *BMEP* and simulated *BMEP* as a function of the case number; **(b)** bisector plot of experimental *BMEP* and simulated *BMEP*.

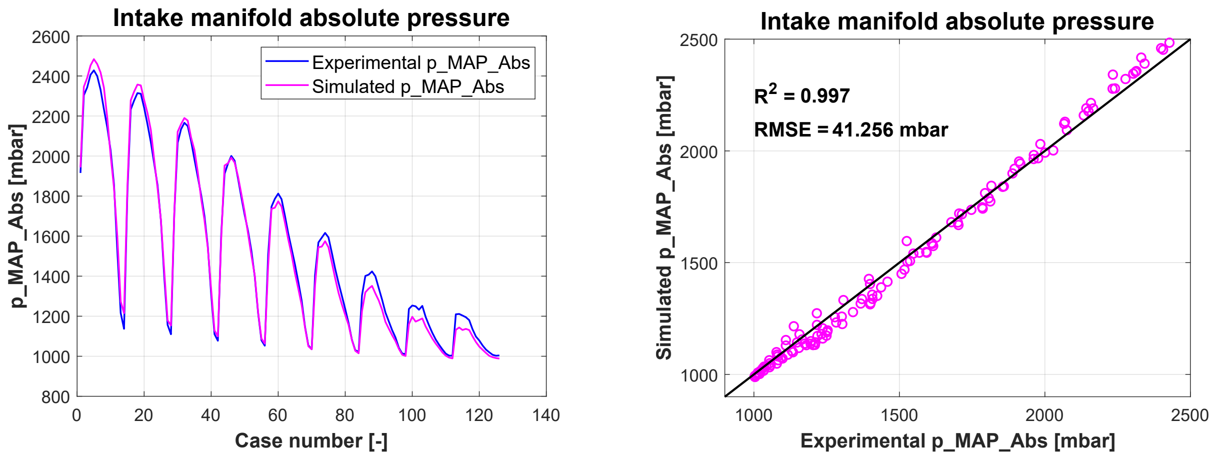

(a) (b)

Figure 2.43: Intake manifold absolute pressure of engine model without ATS: **(a)** experimental *p_MAP_Abs* and simulated *p_MAP_Abs* as a function of the case number; **(b)** bisector plot of experimental *p_MAP_Abs* and simulated *p_MAP_Abs*.

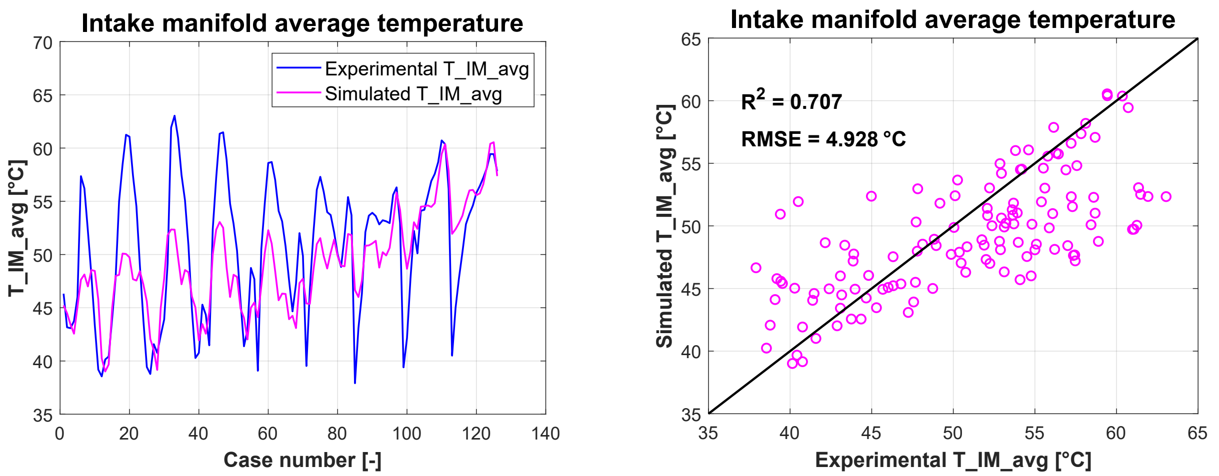

(a) (b)

Figure 2.44: Intake manifold average temperature of engine model without ATS: **(a)** experimental *T_IM_avg* and simulated *T_IM_avg* as a function of the case number; **(b)** bisector plot of experimental *T_IM_avg* and simulated *T_IM_avg*.

Concerning the thermodynamic quantities of the exhaust manifold gases, they are shown in Figures 2.45 and 2.44. The absolute pressure is better than the one of the engine model with ATS, confirmed by the $RMSE$ value that is decreased from 160.811 mbar to 98.068 mbar. At high loads there is an overestimation, reaching gaps of also 300 bar. Instead, at low loads there is an underestimation, anyway lighter than the high loads overestimation. Regarding the average temperature, the simulated *T_EM_avg* is higher than the experimental one, reaching a $RMSE$ of 47.618 °C against the 15.595 °C of the engine model with ATS. The reason, as will be explored on the next chapters, is in the thermal exchange model of the exhaust manifold, which must be improved maintaining at the same time the compliance with the physical limits.

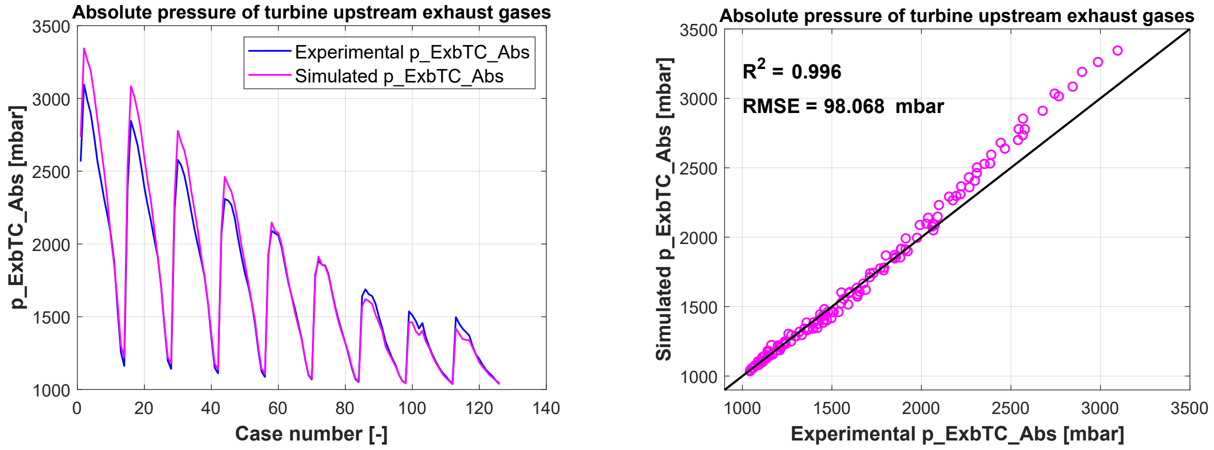

(a) (b)

Figure 2.45: Absolute pressure of turbine upstream exhaust gases of engine model without ATS: **(a)** experimental *p_ExbTC_Abs* and simulated *p_ExbTC_Abs* as a function of the case number; **(b)** bisector plot of experimental *p_ExbTC_Abs* and simulated *p_ExbTC_Abs*.

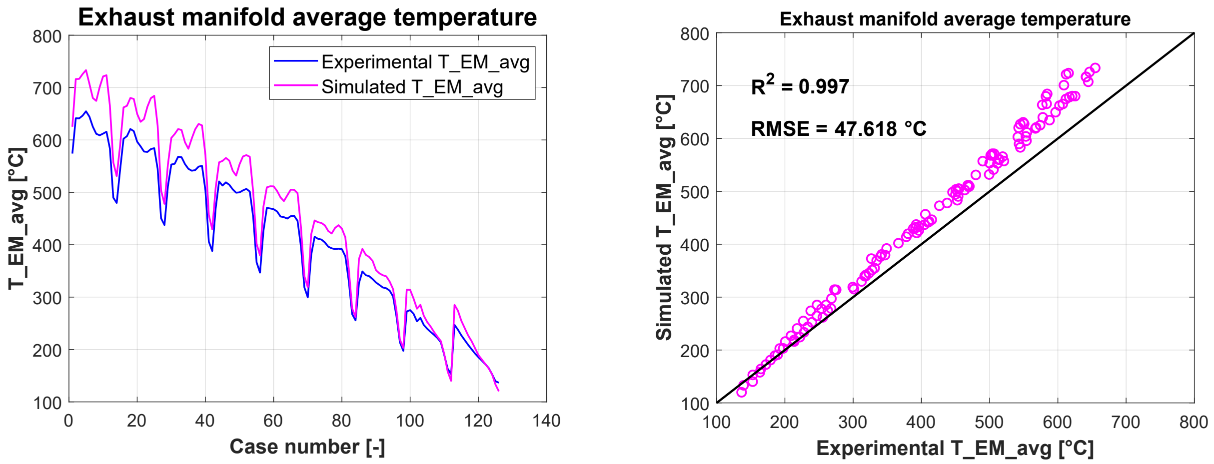

(a) (b)

Figure 2.46: Exhaust manifold average temperature of engine model without ATS: **(a)** experimental *T_EM_avg* and simulated *T_EM_avg* as a function of the case number; **(b)** bisector plot of experimental *T_EM_avg* and simulated *T_EM_avg*.

About the absolute pressure at the turbine downstream (Figure 2.47) the simulated quantity follows the experimental trend in a satisfactory way. Even if there is a slight worsening with respect to the *p_ExaTC_Abs* of the engine model with ATS, the result is suitable and much better than the absolute pressure at the turbine upstream. This means that, as it will be possible to observe in the next chapters, these two pressures do not have a relationship between them. In fact, they depend on different model parameters.
A completely different behavior is assumed by the temperature *T_ExaTC* (Figure 2.48). The simulated quantity greatly overestimates the experimental one, bringing *RMSE* of 68.241 °C, much higher than 17.998 °C of the previous engine model. The same phenomenon of the average temperature within the exhaust manifold occurs, and the reason is again the adopted thermal model, this time the one at the turbine downstream. This reason will be much clearer moving forward with the thesis.

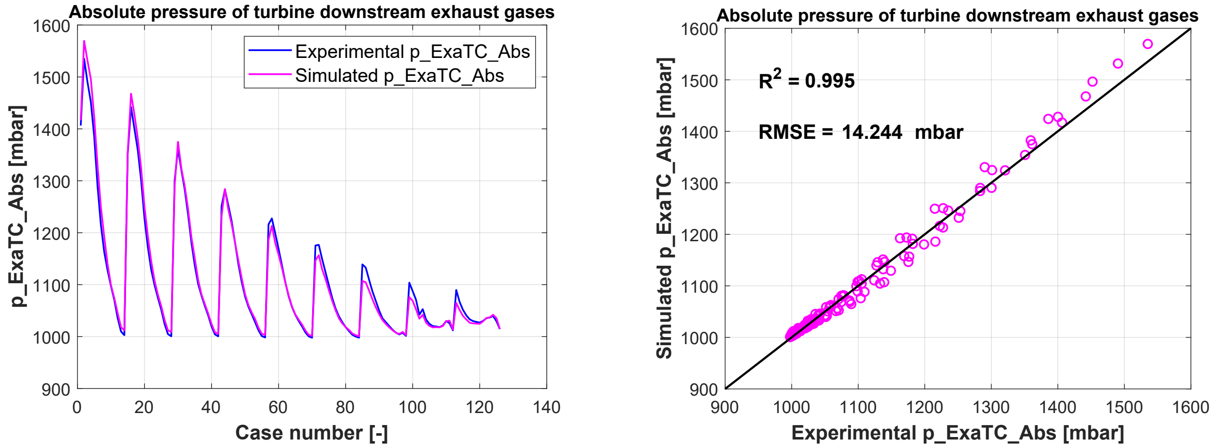

(a) (b)

Figure 2.47: Absolute pressure of turbine downstream exhaust gases of engine model without ATS: **(a)** experimental *p_ExaTC_Abs* and simulated *p_ExaTC_Abs* as a function of the case number; **(b)** bisector plot of experimental *p_ExaTC_Abs* and simulated *p_ExaTC_Abs*.

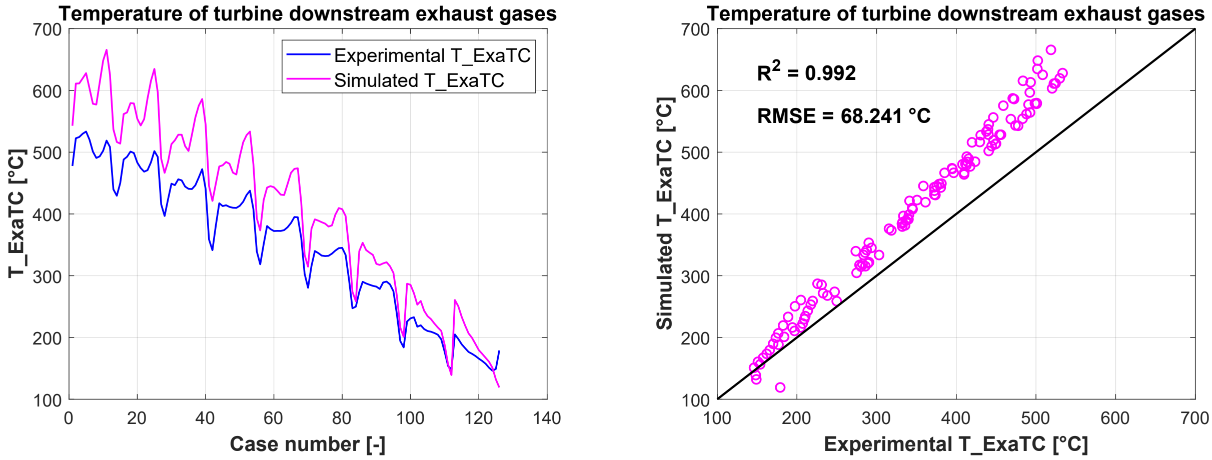

(a) (b)

Figure 2.48: Temperature of turbine downstream exhaust gases of engine model without ATS: **(a)** experimental *T_ExaTC* and simulated *T_ExaTC* as a function of the case number; **(b)** bisector plot of experimental *T_ExaTC* and simulated *T_ExaTC*.

For what concerns the quanties related to the single cylinder, it is anticipated that they all provide a better experimental prediction than the ones of the previous engine model. This feature is due to a precise optimization, whose details will be specified later. Also in this engine model the quantities of the third cylinder have the best outcomes.
Starting from the maximum pressure of cylinder 3 combustion chamber (Figure 2.49), the $RMSE$ is decreased from 4.389 bar of the engine model with ATS to 2.830 bar. The simulated trend at high loads turns out to be closer to the experimental values. The latter behavior is assumed also by *IMEP3* (Figure 2.50) and *IMEPH3* (Figure 2.51). In fact, their $RMSE$ values decrease. The reduction occurs in a more moderate way than the one of maximum pressure *PMAX3*, but also the scale of the values covered by these two mean effective pressure quantities must be considered. The maximum value reached by *IMEP3* and *IMEPH3* is about a seventh of the maximum reached by *PMAX3* and in a proportional way also between the related $RMSE$ values there is approximately this ratio. This happens because of the direct dependence of the net and gross mean effective pressures on the in-cylinder pressure. If the maximum value of the in-cylinder pressure signal increases consequently the subtended area grows, hence the IMEP and IMEPH enhance.

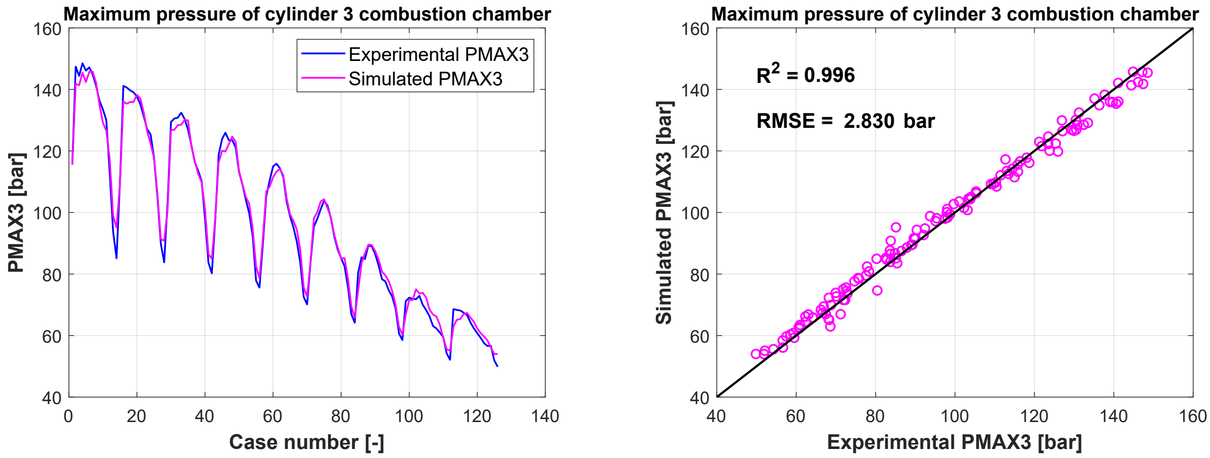

(a) (b)

Figure 2.49: Maximum pressure of cylinder 3 combustion chamber of engine model without ATS: **(a)** experimental *PMAX3* and simulated *PMAX3* as a function of the case number; **(b)** bisector plot of experimental *PMAX3* and simulated *PMAX3*.

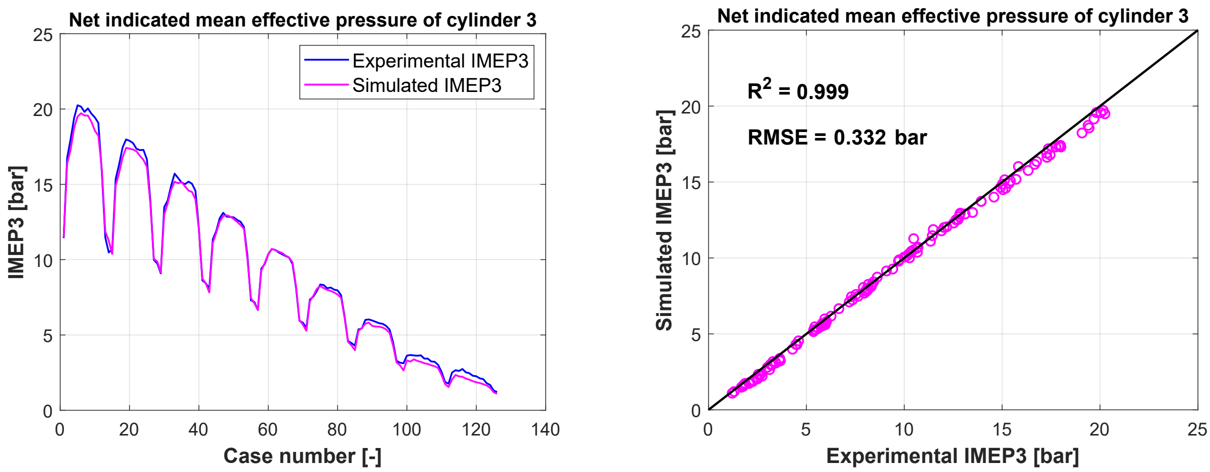

(a) (b)

Figure 2.50: Net indicated mean effective pressure of cylinder 3 of engine model without ATS: **(a)** experimental *IMEP3* and simulated *IMEP3* as a function of the case number; **(b)** bisector plot of experimental *IMEP3* and simulated *IMEP3*.

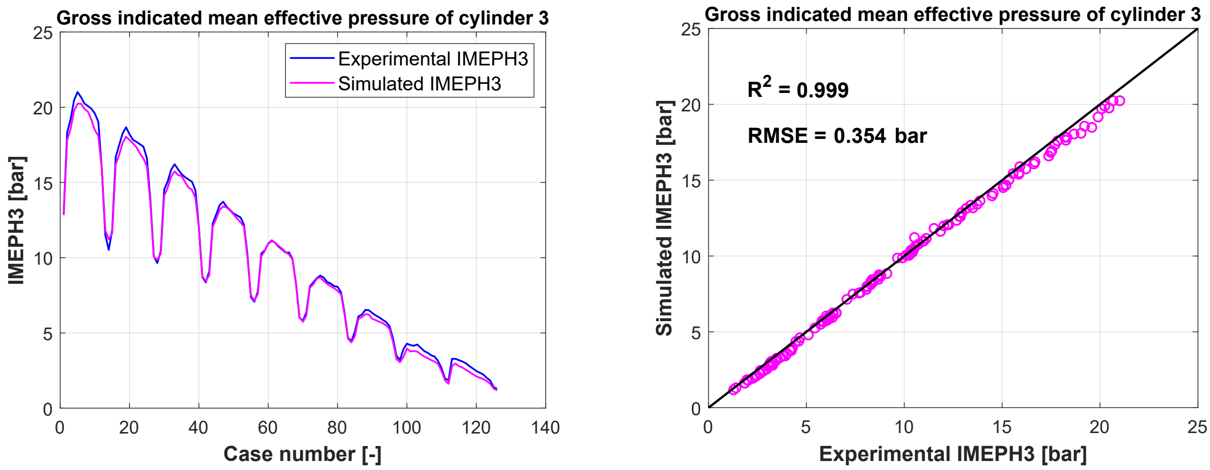

(a) (b)

Figure 2.51: Gross indicated mean effective pressure of cylinder 3 of engine model without ATS: **(a)** experimental *IMEPH3* and simulated *IMEPH3* as a function of the case number; **(b)** bisector plot of experimental *IMEPH3* and simulated *IMEPH3*.

The pumping mean effective pressure is reported in Figure 2.52 and it is possible to observe the same behavior seen for the two previous quantities: the enhancement of the simulated quantity at high loads. This occurs because of the direct dependence of the IMEPL on the net and gross mean effective pressure (2.7). Although here, differently from *IMEP3* and *IMEPH3*, there is an overestimation on the upper peaks at high loads, that however does not compromise the global behavior, which brings a lower $RMSE$ values than the previous engine model.
For concluding, about the quantities related to the single cylinder, the *TFMEP3* is shown in Figure 2.53. The same reasoning performed for the same quantity of the engine model with ATS can be repeated. In fact, the resulting simulated *TFMEP3* of the two models are very similar.

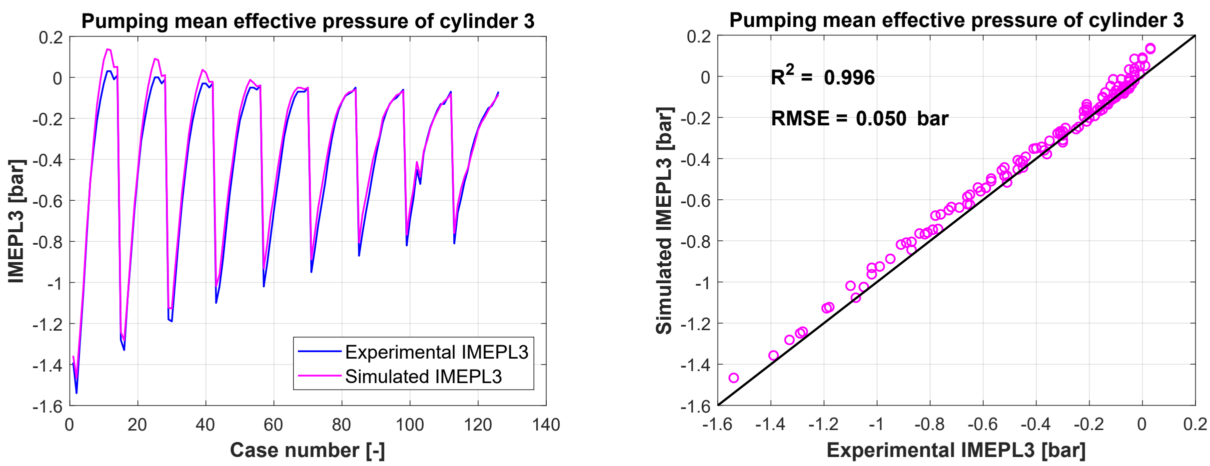

(a) (b)

Figure 2.52: Pumping mean effective pressure of cylinder 3 of engine model without ATS: **(a)** experimental *IMEPL3* and simulated *IMEPL3* as a function of the case number; **(b)** bisector plot of experimental *IMEPL3* and simulated *IMEPL3*.

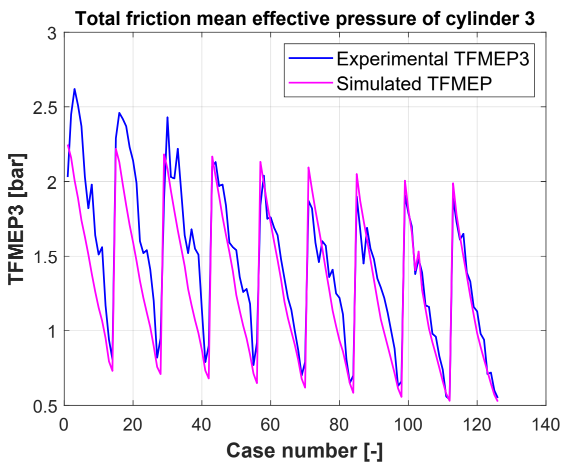

(a)

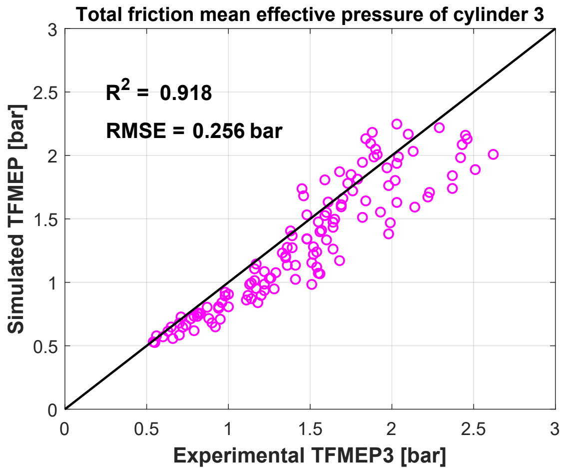

(b)

Figure 2.53: Total friction mean effective pressure of cylinder 3 of engine model without ATS: **(a)** experimental *TFMEP3* and simulated *TFMEP3* as a function of the case number; **(b)** bisector plot of experimental *TFMEP3* and simulated *TFMEP3*.

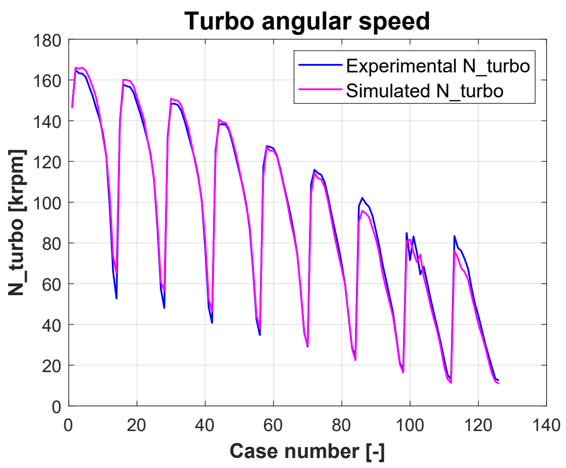

(a)

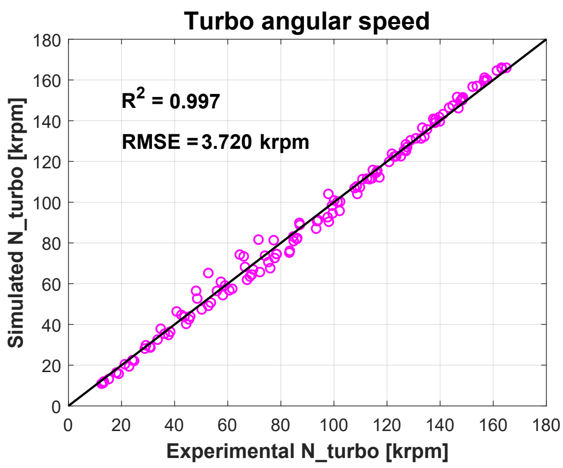

(b)

Figure 2.54: Turbo angular speed of engine model without ATS: **(a)** experimental *N_turbo* and simulated *N_turbo* as a function of the case number; **(b)** bisector plot of experimental *N_turbo* and simulated *N_turbo*.

Moving to the turbo angular speed (Figure 2.54), it is possible to observe an overestimation at high loads and an underestimation at low loads by the simulated *N_turbo*. There is this feature also in the boost pressure (Figure 2.56), and was also observed in the thermodynamic quantities of the intake manifold. In fact, the main reason is again the absence of the closed-loop controller of VGT.
To conclude, the EGR percentage is reported in Figure 2.55 and the simulated *Xr_CO2* globally has more difficulty following the experimental trend, due to the fact that there is not the closed-loop controller of EGR differently from the engine model with ATS.

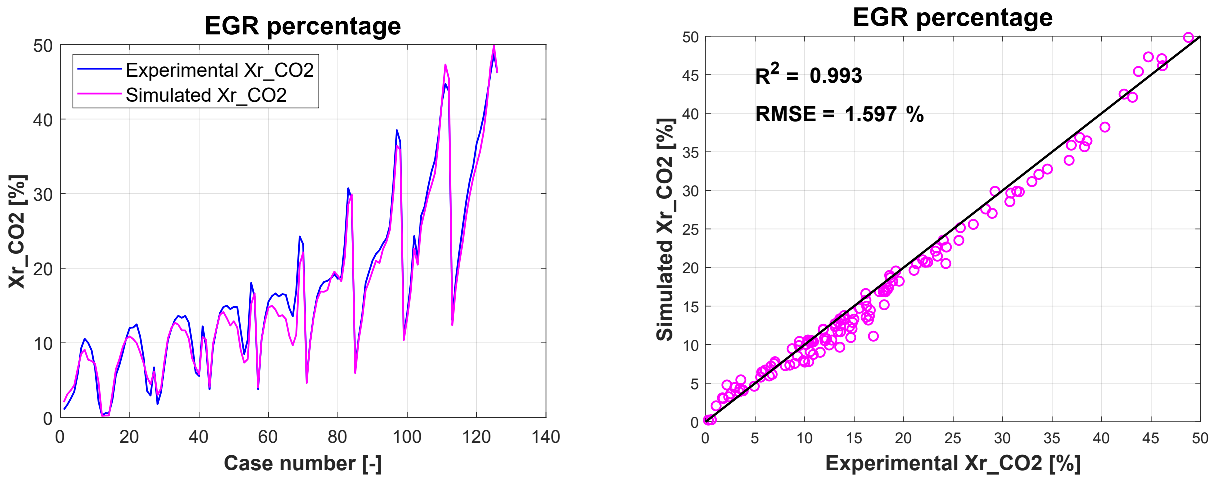

(a) (b)

Figure 2.55: EGR percentage of engine model without ATS: **(a)** experimental *Xr_CO2* and simulated *Xr_CO2* as a function of the case number; **(b)** bisector plot of experimental *Xr_CO2* and simulated *Xr_CO2*.

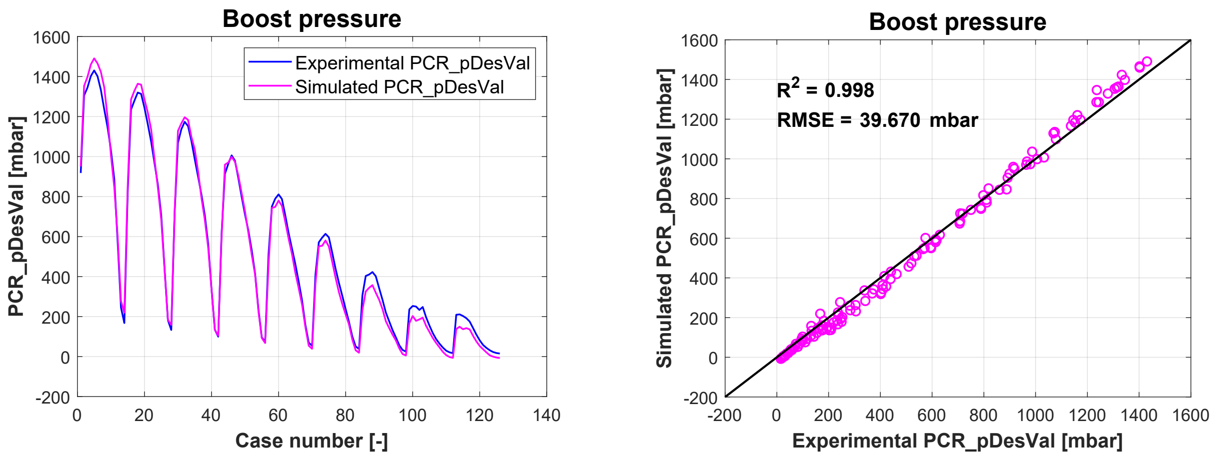

(a) (b)

Figure 2.56: Boost pressure of engine model without ATS: **(a)** experimental *PCR_pDesVal* and simulated *PCR_pDesVal* as a function of the case number; **(b)** bisector plot of experimental *PCR_pDesVal* and simulated *PCR_pDesVal*.

Chapter 3

Integration of the closed-loop controllers into the engine model without ATS

3.1 EGR and VGT controllers

The Exhaust Gas Recirculation and the Variable Geometry Turbine are two very important systems of the diesel engine, which ensure many positive results for some characteristics of this engine type. The EGR guarantees an important reduction of NOx and soot emissions. The VGT brings to an improvement of the engine performances, a reduction of the fuel consumption and also some benefits for the emissions. To obtain a correct operation of these two systems, their control is crucial. Within the engine model, two approaches can be adopted for the EGR and VGT control: the open-loop approach, called also feedforward, and the closed-loop approach, called also feedback.

3.1.1 EGR and VGT open-loop controllers

Before showing the EGR and VGT open-loop controllers in detail, it is necessary to review the basic scheme of an open-loop control (Figure 3.1). This theoretical structure is based on the concept of black box. A black box is a system with one or more inputs and one or more outputs. This system certainly has some features that define itself, but they are internal properties and the important thing is only what the system receives and provides externally.

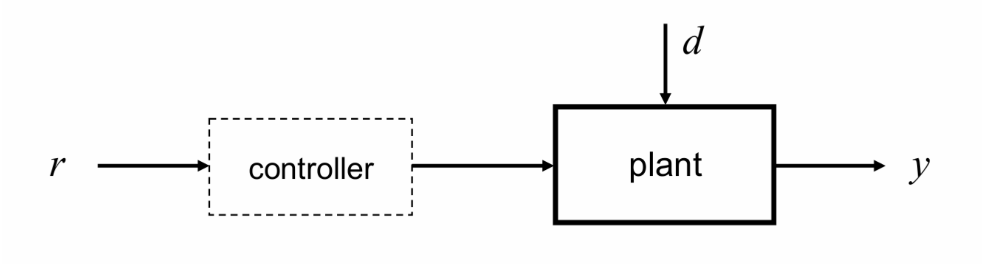

Figure 3.1: Structure of the open-loop control [7].

The structure of the open-loop control is made up of two black boxes: a plant, in this case the engine, and a controller, in this case the EGR and VGT. The controller goal is to provide a command input to the plant such that its output y tracks a desired reference r. The other input d is the disturbance, that cannot be controllable and the controller should be as little as possible sensitive to it.
Starting from the EGR controller in GT-ISE, the open-loop chain is shown in Figure 3.2. It includes three blocks: the signal generator "*EGRexp-opening-1*", the correlation block "*EGRvlv-*

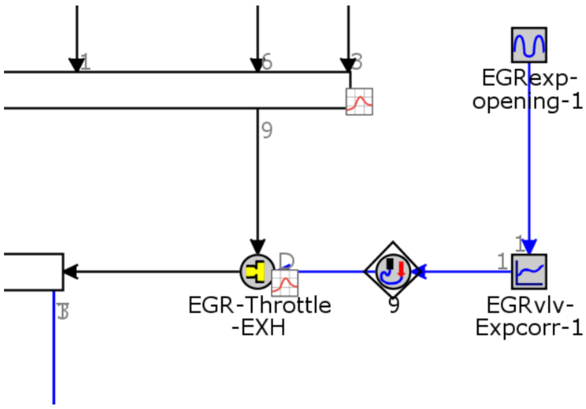

Figure 3.2: Open-loop controller of EGR.

Expcorr-1" and the actuator "*9*". This chain, which represents the controller, acts on the EGR valve called "*EGR-Throttle-EXH*", that directly receives the command input and represents the interface between the controller and the engine, i.e. the plant. The signal generator is the block which provides the desired reference, that is precisely the experimental EGR valve opening, in percentage. The latter is reported in Figure 3.3 and, according to the department dictionary, is named *EGRVlv_rAct*. It is possible to note that this quantity follows in a coherent manner the trend of EGR percentage *Xr_CO2* seen in the previous chapter: at high loads, since it is not suitable to have high EGR amounts, the valve is less open, while at low loads the opening percentage increases reaching also 100 %.

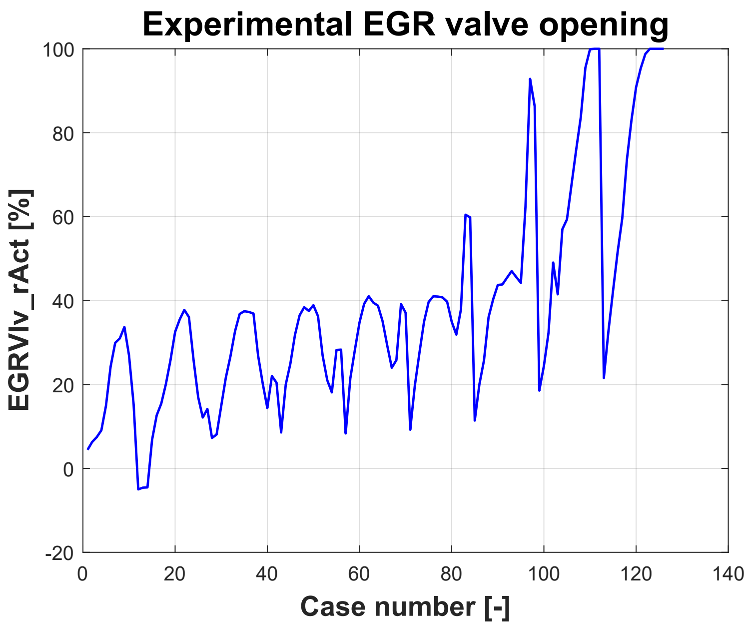

Figure 3.3: Experimental EGR valve opening.

Concerning the EGR correlation block, it has the role of converting the EGR opening percentage into a quantity that is compatible with the GT-ISE block of the EGR throttle valve. This quantity is the hole diameter of the EGR valve. To perform this conversion, a correlation is needed and is inserted directly inside the related block. It is possible to observe this correlation in Figure 3.4. The first feature that can be highlighted is the monotonic trend. The input values are the ones under the name "X data", so a vector with values that go from 0 to 100, the same range covered by the EGR valve opening, i.e. the input of this block. The output values are the ones under the name "Y data", which is the vector of the values of the hole diameter, found through a specific operation of calibration.

Having shown all this mechanism, it is possible to understand that to a precise value of EGR valve opening corresponds a hole diameter value. The latter is imposed to the EGR valve block, by the actuator, which is a widely used GT-ISE block.

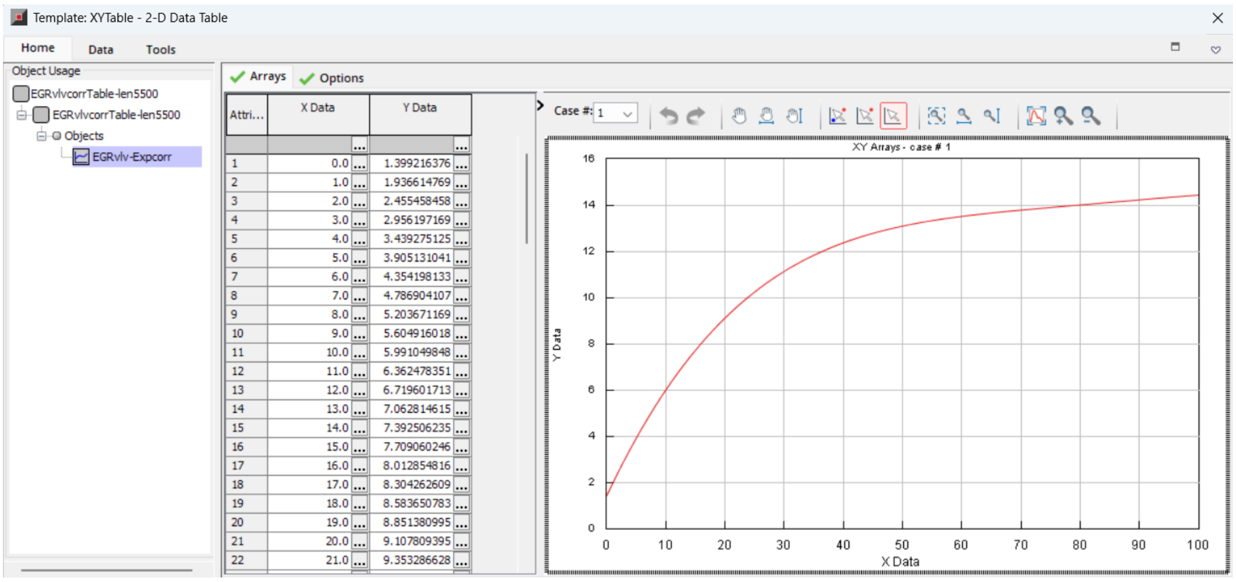

Figure 3.4: EGR correlation.

The other important open-loop controller is the VGT one, whose blocks are shown in Figure 3.5. This controller has the same structure of the EGR open-loop chain. Therefore, there is the signal generator *"VGTexp-op-1"*, the correlation block *"VGT-Expcorr-1"* and the actuator *12*. Within the signal generator, the experimental rack position can be found. The rack position is the quantity through which it is possible to change the geometry of the turbine. This means that to a precise rack position corresponds a precise turbine geometry, so a specific turbine operational characteristic. To understand better the VGT mechanism and what occurs varying the rack position, it is worth going into more detail.

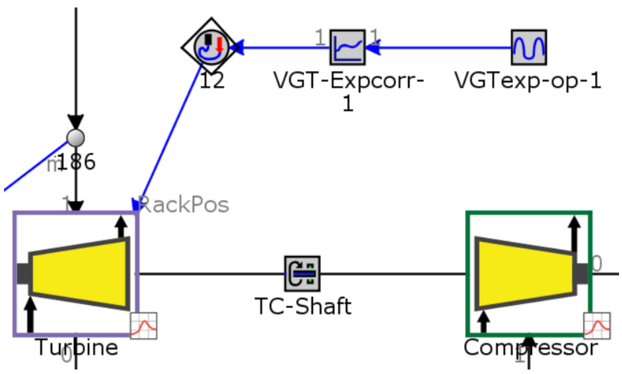

Figure 3.5: Open-loop controller of VGT.

The rack position determines the rotation of the turbine vanes, illustrated in Figure 3.6. At low engine speeds, the vanes are turned to reduce the cross-section. Therefore, the exhaust gases that enter the turbine, considering the same flow rate, flow faster, causing the turbine to rotate faster and consequently also the compressor. In this way more fresh air is introduced, so higher boost level is reached. Instead, at high engine speeds, the vanes are turned to increase the cross-section, so the exhaust gases have less velocity and the boost pressure decreases. It is possible to observe the rack position together with the engine speed in Figure 3.7. So, looking at the diagram, at high engine speeds correspond low percentages of rack position, so the vanes are more open and the turbine cross-section is increased. Instead, at low engine speeds correspond high percentages of rack position, so the vanes are more closed and the turbine cross-section is reduced. At the minimum engine speed the rack position percentage is maximum, i.e. 100 %. This means that the maximum level of vanes closure is reached.

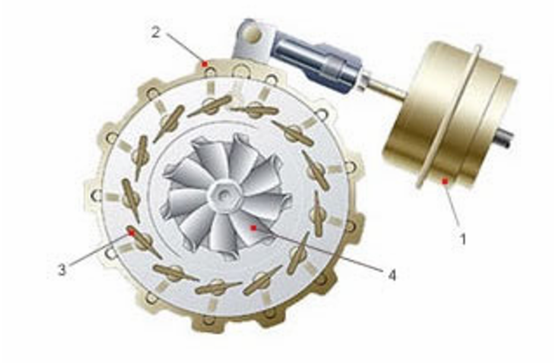

(a)

(b)

Figure 3.6: Variable geometry turbine: **(a)** the vanes are turned to reduce the cross-section, low engine speed configuration; **(b)** the vanes are turned to increase the cross-section, high engine speed configuration [9].

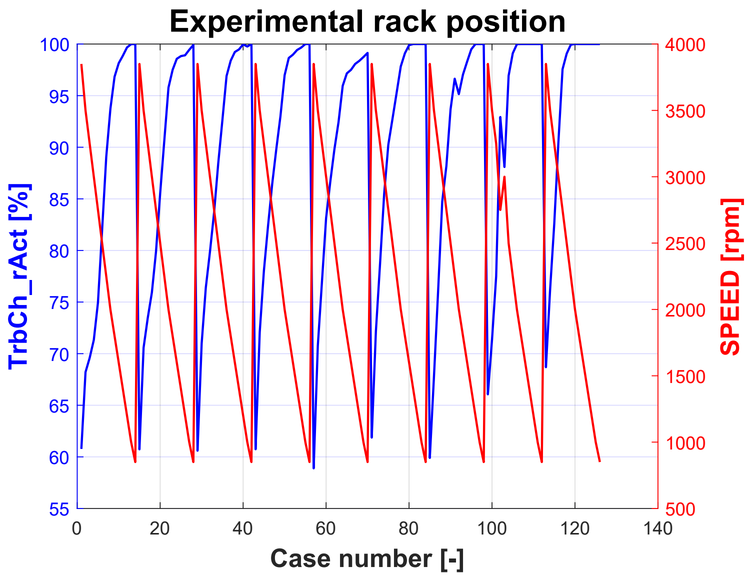

Figure 3.7: Experimental rack position together with the engine speed.

The experimental rack position is the variable required by the turbine block in GT-ISE environment. So, it could be directly delivered to this block, but the software conceives the rack position as the complement to 1 of the experimental one. Therefore, higher percentages of rack position correspond to more open turbine vanes, while lower percentages of it correspond to closer vanes. Because of this difference, a correlation block is needed between the signal generator and the actuator. The correlation function is shown in Figure 3.8. It can be noted that the X data go from 0 to 100, the same range covered by the experimental rack position. The Y data are the corresponding rack position in accordance with the GT-ISE convention. They are given by the function illustrated that, starting from the origin, increases a little until reaching a maximum in $X = 14$ and then decreases very slightly.
Finally, the actuator receives the rack position provided by the correlation function and gives it to the turbine block.

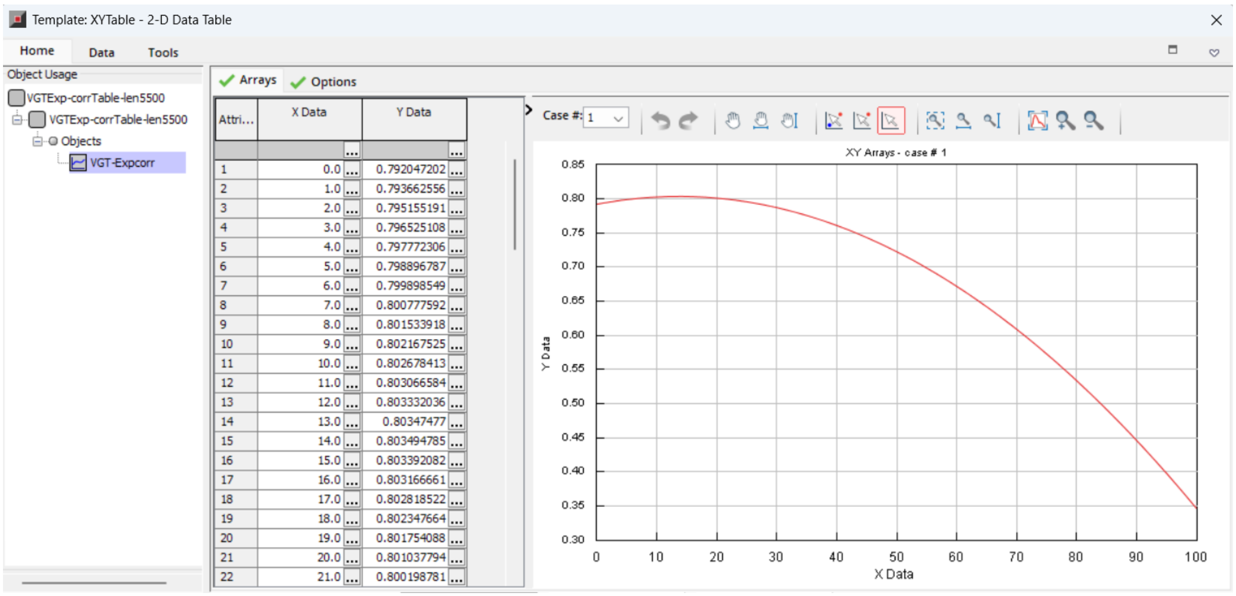

Figure 3.8: VGT correlation.

3.1.2 EGR and VGT closed-loop controllers

The main advantage of the EGR and VGT open-loop controllers is that they allow to understand how the command input can influence the engine. In fact, the correlation function must be chosen and the goal is to find the trend that ensures the engine model the best prediction of the experimental results. However, referring to the previous open-loop structure of Figure 3.1, the controller is not aware of what is actually happening to the output of the plant. Therefore, about the controller design, in particular about the calibration of the correlation function, the behavior of the plant and its outputs must be carefully known. It will be possible to observe and understand how a calibration is performed in the penultimate chapter. For the moment, the only but very important information that is worth knowing is that the closed-loop controllers are exploited.

The theoretical scheme of a closed-loop control is reported in Figure 3.9. There are again the two black boxes, and this time there is a new element, i.e. the red arrow. The latter represents the feedback signal, by which the controller is aware of what is occurring to the plant output. In this way, the controller can compute the instantaneous error between the desired reference and the plant output and give to the plant a command input u such that this error is minimized. Thanks to the feedback, the controller can guarantee the output a very good level of precision, higher than the one reached by an open-loop control.

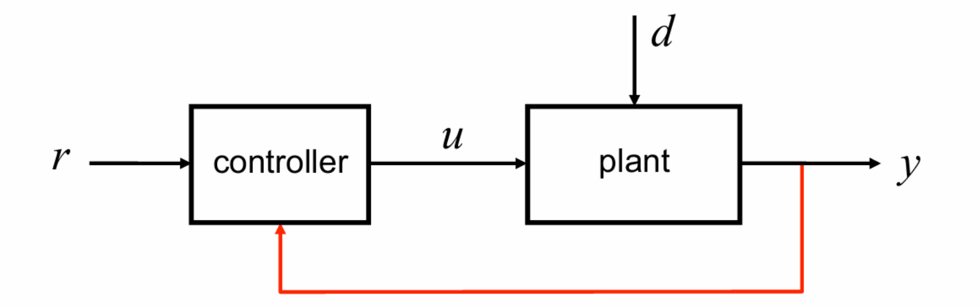

Figure 3.9: Structure of closed-loop control [7].

Many types of closed-loop controllers exist. GT-ISE uses one of the simplest, which is the PID controller, shown in Figure 3.10. It is a controller that performs three actions on the instantaneous error e between the desired reference r and the plant output y: a proportional action, an integral action and a derivative action. In fact, the term PID is the acronym of Proportional Integral Derivative.

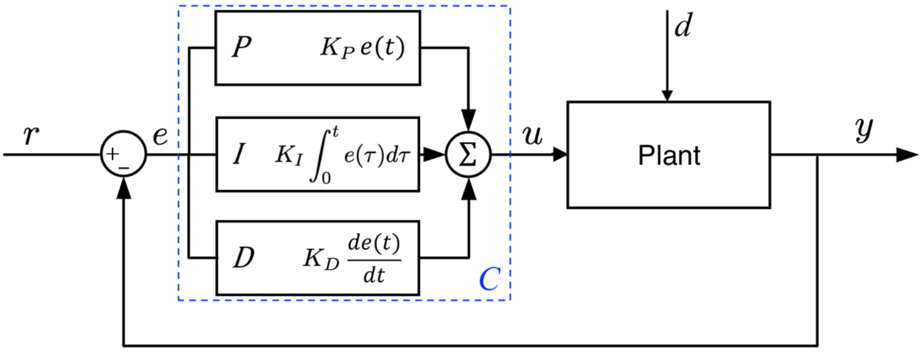

Figure 3.10: Structure of PID closed-loop control [8].

The resulting command input, provided by the PID controller to the plant, is defined by the equation 3.1.

$$u(t) = K_P \cdot e(t) + K_I \cdot \int_0^t e(\tau)d\tau + K_D \cdot \dot{e}(t) \tag{3.1}$$

where

- $e(t) = r(t) - y(t)$: tracking error;
- $K_P \cdot e(t)$: proportional action;
- $K_I \cdot \int_0^t e(\tau)d\tau$: integral action;
- $K_D \cdot \dot{e}(t)$: derivative action;

The proportional action takes into account the present. It supplies a command input to reduce the instantaneous tracking error. The integral action takes into account the past. In fact, the integral is the sum of past values and through it this action ensures a very small tracking error for constant or slowly-varying references. Finally, there is the derivative action. Since the derivative itself expresses the variation of the signal, it takes into account the future. Therefore, its action improves the dynamic performance and robustness of the controller.
The weight of each of these three actions can be tuned through their constants, i.e. K_P, K_I and K_D. It can be a long work to perform, but fortunately GT-ISE provides blocks which execute this operation themselves.
Starting from the EGR closed-loop control (Figure 3.11), the controller is the block called "*ControllerEGR*". It receives two feedbacks from the engine: the EGR mass flow rate, taken from "*EGR-cooler-1*" (Figure 3.11(a)) and provided by the actuator "*31*", and the air mass flow rate, taken from "*Intercooler-1*" (Figure 3.11(b)) and supplied by the actuator "*30*". These two feedback quantities are needed within the controller to compute the instantaneous EGR fraction in percentage, using the formulation 3.2.

$$EGR_{fraction}[\%] = \frac{\dot{m}_{EGR}}{\dot{m}_{air} + \dot{m}_{EGR}} \cdot 100 \tag{3.2}$$

The feedback EGR fraction is subtracted from the target EGR fraction, which is the desired reference. This target is in the form of a 3D map, called "*RLTEGRMap*" (Figure 3.12). This map, which is present inside the controller, is made up of the values of EGR fraction in percentage as a function of the engine speed and BMEP. So, considering a single GT-SUITE case, i.e. for a precise couple of engine speed and BMEP values, the corresponding value of reference EGR

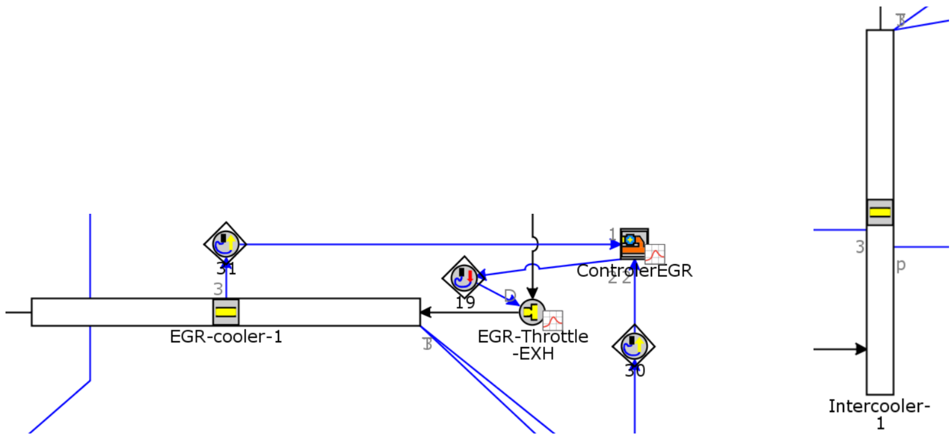

(a) (b)

Figure 3.11: EGR closed-loop control.

fraction is selected, from which the current feedback EGR fraction is subtracted. From this operation the EGR fraction error results, and the aim of the controller is to minimize it, working with the PID logic. The command input is in the form of a hole diameter, provided by the controller to the actuator "*19*", which delivers it to the EGR valve, called "*EGR-Throttle-EXH*".

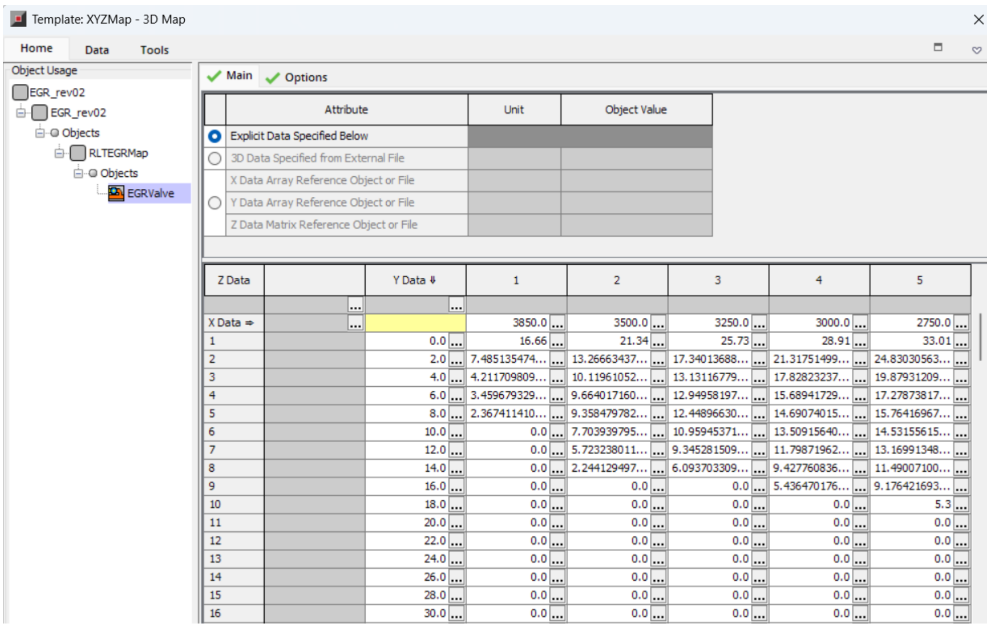

Z Data		Y Data ⇓	1	2	3	4	5
X Data ⇒			3850.0	3500.0	3250.0	3000.0	2750.0
1		0.0	16.66	21.34	25.73	28.91	33.01
2		2.0	7.485135474...	13.26663437...	17.34013688...	21.31751499...	24.83030563...
3		4.0	4.211709809...	10.11961052...	13.13116779...	17.82823237...	19.87931209...
4		6.0	3.459679329...	9.664017160...	12.94958197...	15.68941729...	17.27873817...
5		8.0	2.367411410...	9.358479782...	12.44896630...	14.69074015...	15.76416967...
6		10.0	0.0	7.703939795...	10.95945371...	13.50915640...	14.53155615...
7		12.0	0.0	5.723238011...	9.345281509...	11.79871962...	13.16991348...
8		14.0	0.0	2.244129497...	6.093703309...	9.427760836...	11.49007100...
9		16.0	0.0	0.0	0.0	5.436470176...	9.176421693...
10		18.0	0.0	0.0	0.0	0.0	5.3
11		20.0	0.0	0.0	0.0	0.0	0.0
12		22.0	0.0	0.0	0.0	0.0	0.0
13		24.0	0.0	0.0	0.0	0.0	0.0
14		26.0	0.0	0.0	0.0	0.0	0.0
15		28.0	0.0	0.0	0.0	0.0	0.0
16		30.0	0.0	0.0	0.0	0.0	0.0

Figure 3.12: Target map of EGR closed-loop control.

Concerning the VGT closed-loop control, the group of needed blocks is shown in Figure 3.13. The controller is the block called "*eVGT*", that receives one feedback, which is the current pressure inside the intake manifold. The latter is provided by the actuator "*49*" to the controller. The desired reference is the target boost pressure, also in this case under the form of a 3D map (Figure 3.14). It is made up of boost pressure values in [bar], and as the previous target EGR fraction map can vary with engine speed and BMEP. Hence, considering a precise couple of engine speed and BMEP values, the controller selects a specific value of target boost pressure, from which the feedback pressure is subtracted. The boost pressure error results, and it is essential for the controller to actuate the command input, always through the PID logic. The command input is a specific value of rack position, supplied to the turbine by the actuator "*233*".

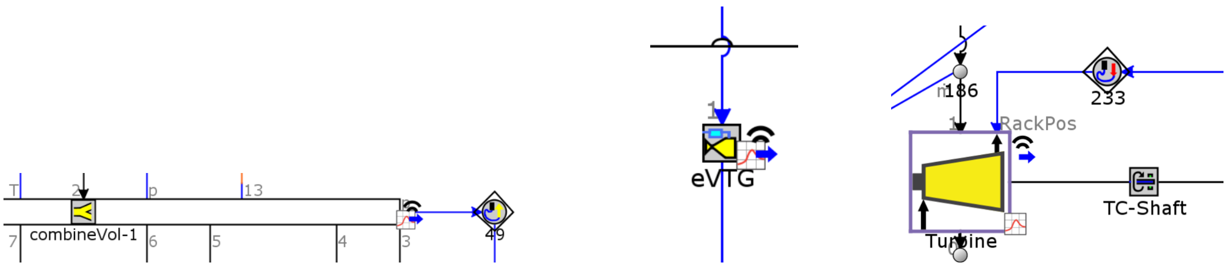

Figure 3.13: VGT closed-loop control.

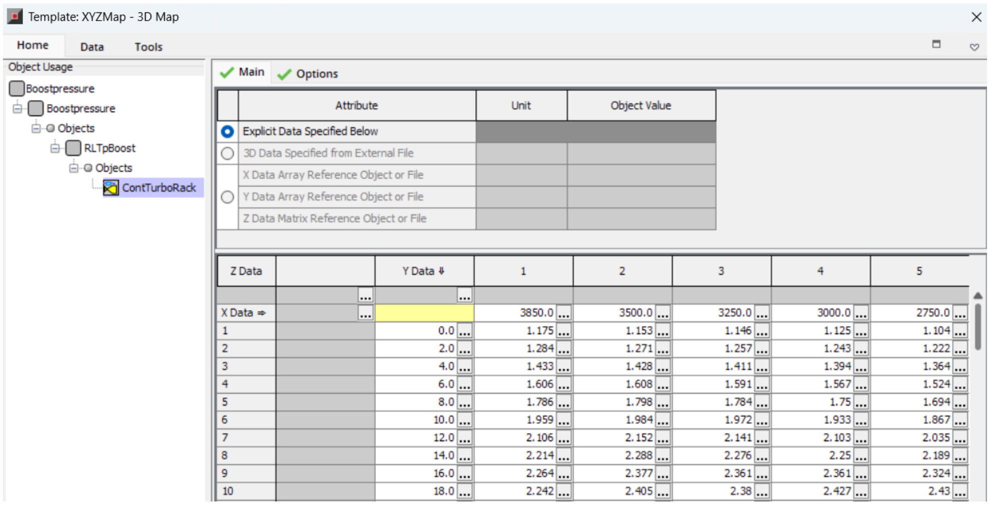

Z Data	Y Data	1	2	3	4	5
X Data		3850.0	3500.0	3250.0	3000.0	2750.0
1	0.0	1.175	1.153	1.146	1.125	1.104
2	2.0	1.284	1.271	1.257	1.243	1.222
3	4.0	1.433	1.428	1.411	1.394	1.364
4	6.0	1.606	1.608	1.591	1.567	1.524
5	8.0	1.786	1.798	1.784	1.75	1.694
6	10.0	1.959	1.984	1.972	1.933	1.867
7	12.0	2.106	2.152	2.141	2.103	2.035
8	14.0	2.214	2.288	2.276	2.25	2.189
9	16.0	2.264	2.377	2.361	2.361	2.324
10	18.0	2.242	2.405	2.38	2.427	2.43

Figure 3.14: Target map of VGT closed-loop control.

The EGR and VGT closed-loop controllers have been described. They surely have the advantage of guaranteeing a high level of precision, and it will be possible to observe this in the next section. However, all the control logic that has been explained occurs inside the blocks of EGR and VGT controllers. Therefore, it is not possible to directly handle the control logic, deciding a precise correlation between the involved variables.

3.2 Integration of the closed-loop controllers into the engine model without ATS and the effects of integration

This section is reserved for the integration of the two closed-loop controllers into the engine model without ATS. This means that the open-loop chains that acted on the EGR valve diameter and on the turbine rack position have been replaced by the EGR and VGT closed-loop structures. Therefore, a new model has been created, i.e. the engine model without ATS equipped with EGR and VGT closed-loop controllers.
This new version of the engine model without ATS is very useful to directly observe what effects have the presence of the closed-loop controllers on the simulation outcomes. However, the main reason is to align this model to the engine configuration with ATS, in order to examine in detail the differences between them. This accurate comparison will be performed in the next chapter.

A simulation with this new engine configuration without ATS was run. All the main engine quantities were examined and compared with the outcomes given by the original model. For sake of simplicity, only the quantities that exhibit the greatest differences are shown, and they are:

- *Xr_CO2*: EGR percentage;
- *PCR_pDesVal*: boost pressure;
- *N_turbo*: turbo angular speed;
- *mairwet*: wet air mass flow rate;
- *mairdry*: dry air mass flow rate;
- *p_MAP_Abs*: intake manifold absolute pressure;
- *p_ExbTC_Abs*: absolute pressure of turbine upstream exhaust gases.

In each diagram there are three trends: the experimental one, the simulated one of the engine configuration equipped with open-loop controllers and the simulated one of the engine layout equipped with closed-loop controllers. Furthermore, two tables are reported, one for the squared correlation coefficients and another for the root mean square errors.
It is worth starting with the analysis of the two quantities directly linked to the EGR and VGT controllers, which are the EGR percentage (Figure 3.15) and the boost pressure (Figure 3.16). Both quantities show an improvement of the experimental prediction through the integration of the closed-loop controllers. The trend of the EGR percentage given by the configuration with closed-loop controllers is slightly lower than the experimental one in many zones, especially at high and medium loads. However, it is certainly improved with respect to the original engine configuration. Instead, about the boost pressure, the new simulated trend follows almost perfectly the experimental one.

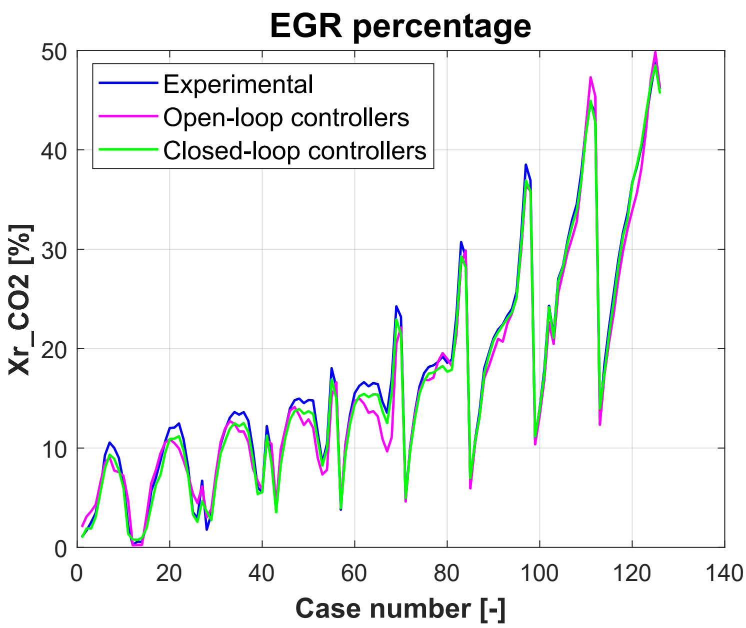

Figure 3.15: EGR percentage of the engine model without ATS: comparison between the original configuration with open-loop controllers and the new configuration with closed-loop ones.

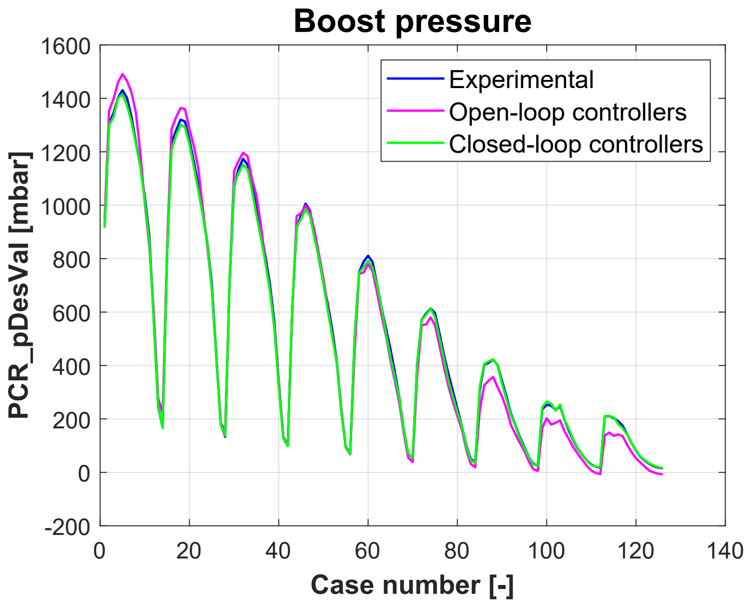

Figure 3.16: Boost pressure of the engine model without ATS: comparison between the original configuration with open-loop controllers and the new configuration with closed-loop ones.

Regarding the speed of the turbo charger, it is shown in Figure 3.17. Again, the introduction of the closed-loop controllers brings more precision in the experimental estimate, especially at the upper peaks.

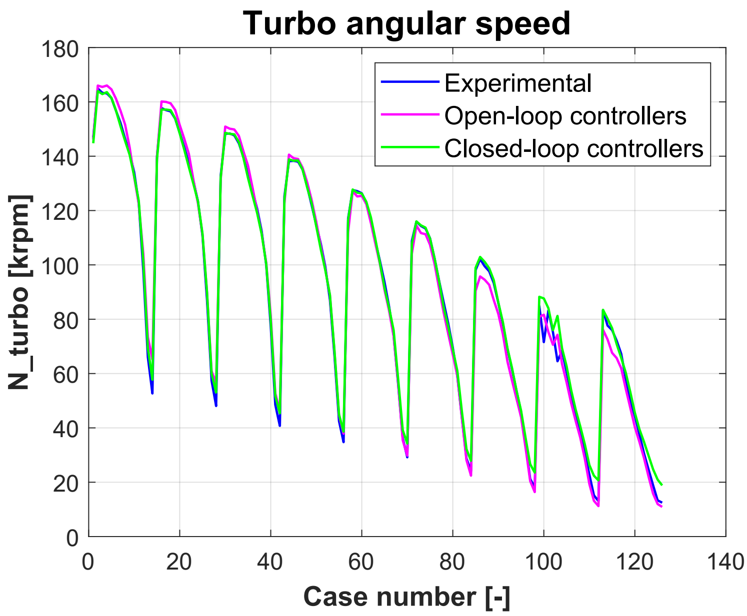

Figure 3.17: Turbo angular speed of the engine model without ATS: comparison between the original configuration with open-loop controllers and the new configuration with closed-loop ones.

The wet and dry air mass flow rates, shown in Figure 3.18 and 3.19 respectively, follow in better way the corresponding experimental trends. It cannot be immediately noticed by looking at the diagram, because the improvement is not so high. However, observing later the $RMSE$ values it will be possible to detect the closed-loop controllers effect.

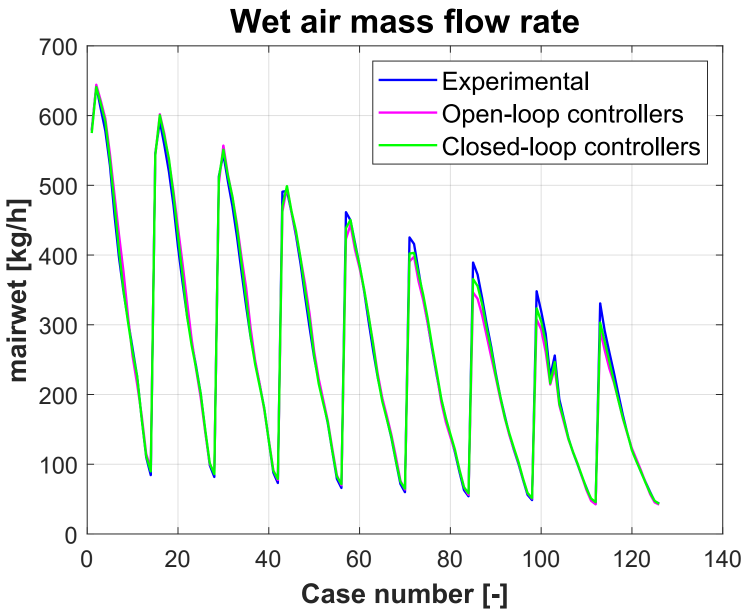

Figure 3.18: Wet air mass flow rate of the engine model without ATS: comparison between the original configuration with open-loop controllers and the new configuration with closed-loop ones.

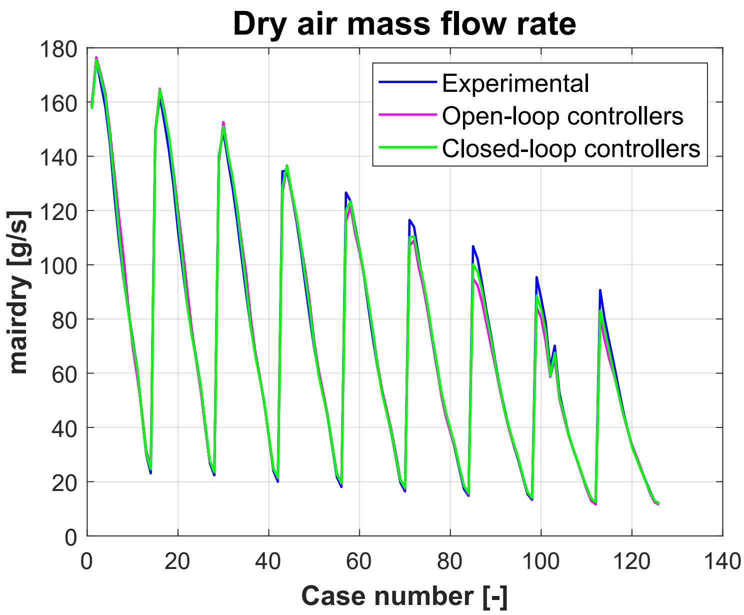

Figure 3.19: Dry air mass flow rate of the engine model without ATS: comparison between the original configuration with open-loop controllers and the new configuration with closed-loop ones.

The simulated intake manifold absolute pressure *p_MAP_Abs* of the engine model with closed-loop controllers (Figure 3.20) no longer has evident gaps with the experimental trend at high and low loads. This quantity is above all linked to the boost pressure, and since the experimental prediction of the latter is improved thanks to the introduction of the closed-loop controllers, the pressure of the intake manifold behaves equally.
Finally, about the absolute pressure of the exhaust manifold (Figure 3.21) the new simulated trend has the same variation direction of the intake manifold pressure. In fact, at high loads the values decrease, while at low loads the values grow, even in greater extent. However, a satisfactory behavior of the simulated quantity is not reached yet, due to the fact that this quantity depends on other factors, as it will be possible to observe in the next chapters.

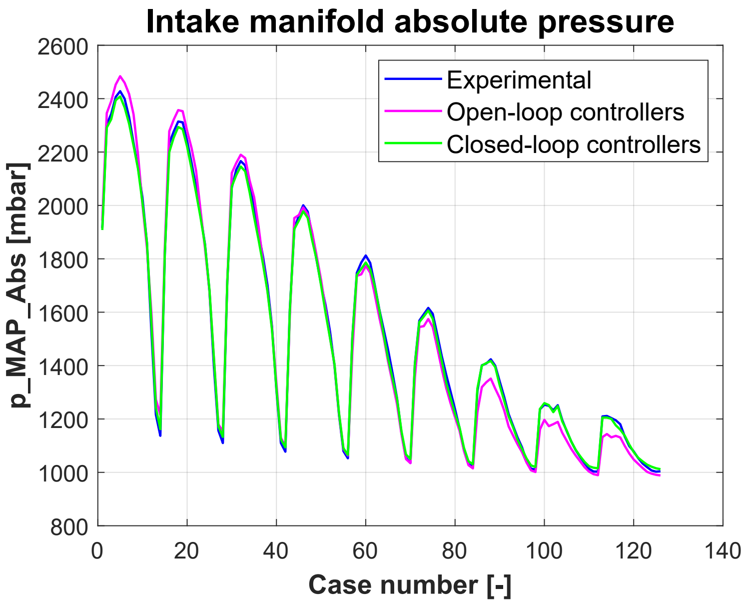

Figure 3.20: Intake manifold absolute pressure of the engine model without ATS: comparison between the original configuration with open-loop controllers and the new configuration with closed-loop ones.

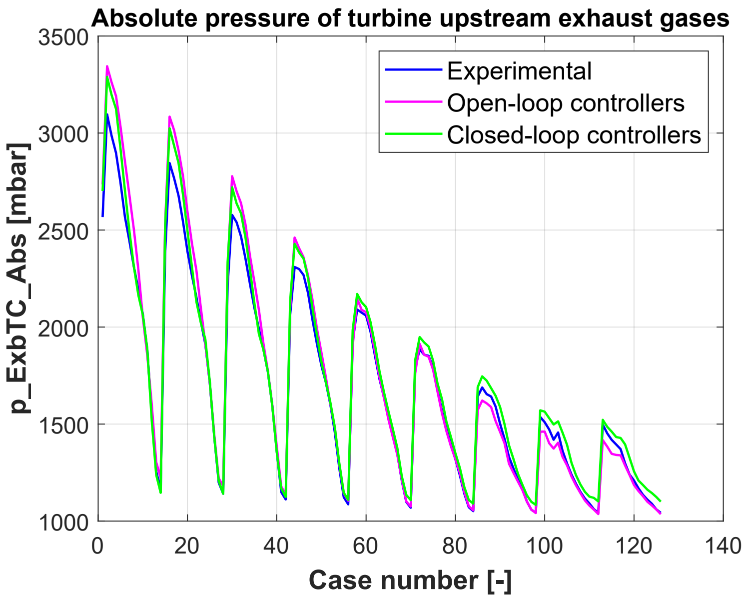

Figure 3.21: Exhaust manifold absolute pressure of the engine model without ATS: comparison between the original configuration with open-loop controllers and the new configuration with closed-loop ones.

The Table 3.1 shows the squared correlation coefficients R^2 of the simulated trends of both the original open-loop and the new closed-loop engine configuration. It can be noted that the correlation between the simulated and the experimental trend improves introducing the closed-loop controllers, but in a negligible way. The real effect can be observed by looking at the root mean squared errors $RMSE$, reported in Table 3.2. All the $RMSE$ values reduce from open-loop to closed-loop configuration, therefore, as expected, the closed-loop controllers ensure more accuracy to the engine quantities about the experimental prediction. Through these values it is also possible to understand which quantities improve more. The greatest improvement, always paying attention to the scale of values that is covered, is shown by the boost pressure and the absolute pressure of the intake manifold. Then, there is the EGR percentage, whose $RMSE$ value decreases of almost 50 %. Hence, the greatest variation is shown by the quantities directly linked to the controllers. Instead, a less variation is exhibited by the other quantities, which anyway are subjected to a discrete improvement.

	Open-loop controllers	**Closed-loop controllers**
Xr_CO2	0.993	0.999
PCR_pDesVal	0.998	1.000
N_turbo	0.997	0.998
mairwet	0.996	0.999
mairdry	0.996	0.999
p_MAP_Abs	0.997	1.000
p_ExbTC_Abs	0.996	0.998

Table 3.1: Squared correlation coefficients R^2 of the engine configuration with open-loop controllers and the engine configuration with closed-loop ones.

	Open-loop controllers	**Closed-loop controllers**
Xr_CO2	1.597 %	0.865 %
PCR_pDesVal	39.670 mbar	12.865 mbar
N_turbo	3.720 krpm	3.153 krpm
mairwet	14.318 kg/h	8.385 kg/h
mairdry	3.968 g/s	2.336 g/s
p_MAP_Abs	41.256 mbar	15.775 mbar
p_ExbTC_Abs	98.068 mbar	72.539 mbar

Table 3.2: Root mean square errors $RMSE$ of the engine configuration with open-loop controllers and the engine configuration with closed-loop ones.

Chapter 4

Analysis of the differences between the two engine models

4.1 Injectors modification inside the engine model with ATS

Before executing a direct comparison of the two engine models, it is necessary to perform an alignment operation of the two configurations. A step of this process has already been executed in the previous chapter, in which the closed-loop controllers of EGR and VGT have been integrated into the engine model without ATS, to associate it more with the version equipped with ATS. In this section, the aim is to carry out another step of this alignment execution, i.e. to modify the features of the injectors of the engine model with ATS. The injector blocks are highlighted in Figure 4.1 and two elements of the injector object are involved in this change: the rail pressure and the injection profiles.

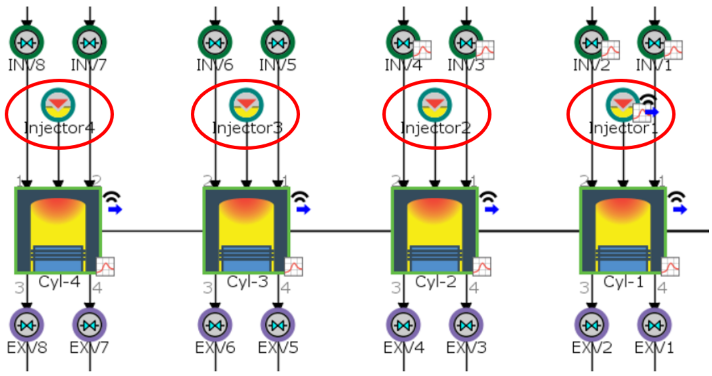

Figure 4.1: Injectors of the engine model with ATS.

Starting from the rail pressure, the related modification is shown in Figure 4.2. In the original configuration of the engine model with ATS, the rail pressure is defined by a 3D map in which the rail pressure values are as a function of the engine speed and BMEP. So, considering a precise couple of engine speed and BMEP values, a specific rail pressure value can be selected. This map, highlighted in red in Figure 4.2(a), was replaced by the experimental values of the rail pressure (Figure 4.2(b)), imposed by the "Case Setup" section of GT-ISE. In fact, this is a feature that is own of the engine model without ATS, and after this change the degree of alignment between the two models is enhanced.
The second modification regards the "Profiles" section of the injector object. First of all, it is possible to observe in Figure 4.3 that the engine model with ATS already has an imposition of the experimental values, which is about the injected mass per pulse of the main injection. This feature, as observed in the Chapter 2, ensures the simulated average fuel consumption during the test an almost perfect prediction of the related experimental values. About the injection timing of the main injection and about the injection mass per pulse and injection timing of the two pilot

injections, the injector object of the engine model with ATS shows 3D maps. The latter operate in the same way as the rail pressure map, but their values are the fuel mass quantities and the crank angles of Start Of Injection (SOI). To also align this feature with the engine model without ATS, these five maps, highlighted in Figure 4.3(a), are replaced with the corresponding experimental values (Figure 4.3(b)), always imposed by the "Case Setup" section.

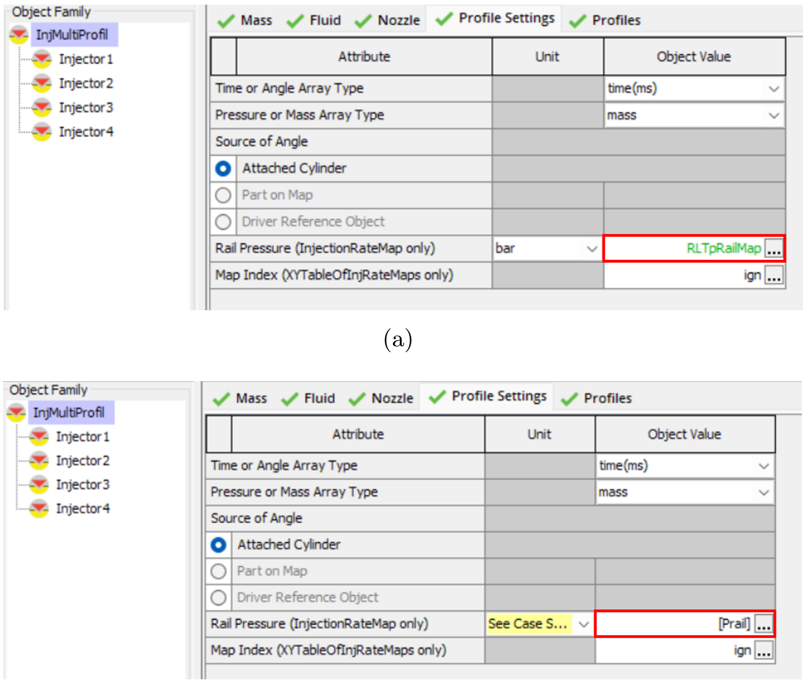

(a)

(b)

Figure 4.2: Rail pressure modification inside the injector object of the engine model with ATS: the rail pressure map **(a)** has been replaced by the experimental rail pressure values **(b)**.

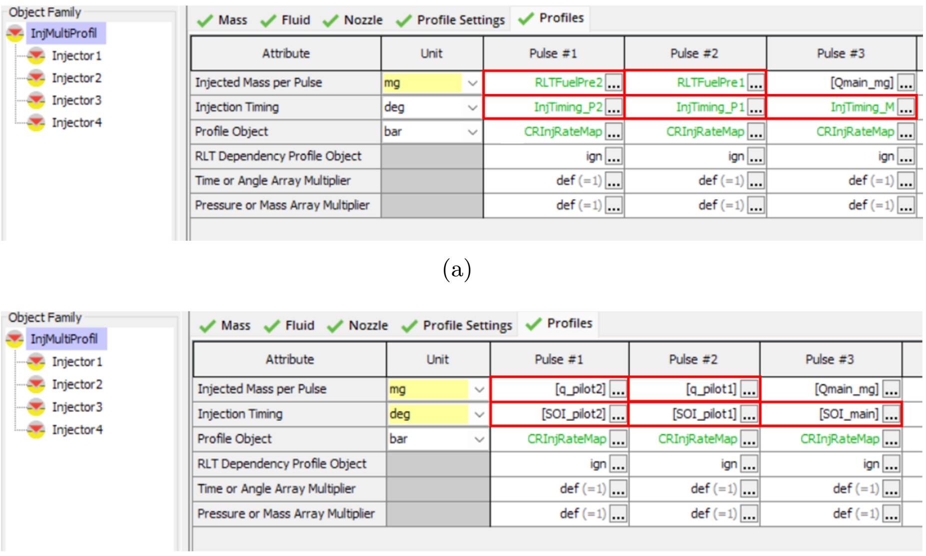

(a)

(b)

Figure 4.3: Profiles modification inside the injector object of the engine model with ATS: the highlighted maps **(a)** have been replaced by the experimental values of injected mass per pulse and injection timing **(b)**.

The presence of pilot injections is very important. In fact, they are needed to reduce the combustion noise, linked to the in-cylinder pressure gradient. The pilot injections work on the Heat Release Rate (HRR) of the premixed phase, which is the phase of the diesel engine combustion where there is the highest burning rate. The HRR is shaped in such a way that it no longer has a single high peak but more peaks of lower intensity. This leads to a reduction of the in-cylinder pressure gradient, resulting in a decrease of combustion noise.

4.2 Comparison of the two engine models

Having aligned the two engine models, it is now possible to make a direct comparison between them. Therefore, the engine model with ATS and with the new injector object and the engine model without ATS and equipped with closed-loop controllers are subjected to a simulation and their outcomes are compared.
The engine quantities that exhibit the greatest differences are reported. In each chart it is possible to observe the experimental trend, the simulated trend of the engine model with ATS and the simulated trend of the engine model without ATS.
Starting with the brake mean effective pressure (Figure 4.4), the differences between the results of the two engine models are detectable at high and medium loads. In particular, at high loads it is possible to observe that the engine model with ATS underestimates the *BMEP*, while the engine model without ATS has a very good behavior. This is consistent with what was shown in Chapter 2, i.e. the fact that the engine model without ATS is optimized for the *BMEP* and for all the quantities regarding the single cylinder. The reasons will be explained in the next section, reserved for the differences between the two engine models.

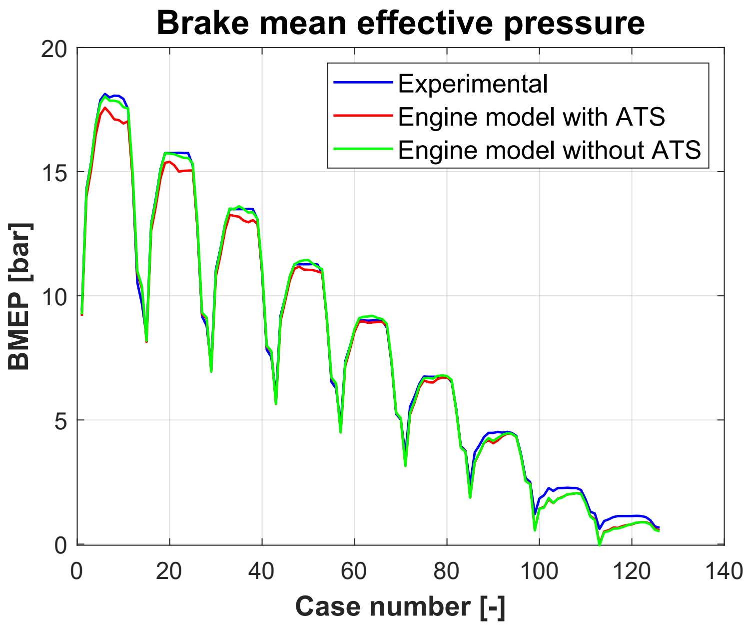

Figure 4.4: Comparison of *BMEP* of the two engine models.

Another quantity that shows an evident difference is the intake manifold average temperature, reported in Figure 4.5. Both the simulated trends do not follow well the experimental one. As it was enounced in the Chapter 2, this issue is probably due to the complex thermodynamics determined by the EGR, and it is hard to develop a suitable model for describing it carefully. In the engine model without ATS the experimental estimate is also worse, but, considering the scale of covered values and the difficulty related to this quantity, it is an acceptable result.

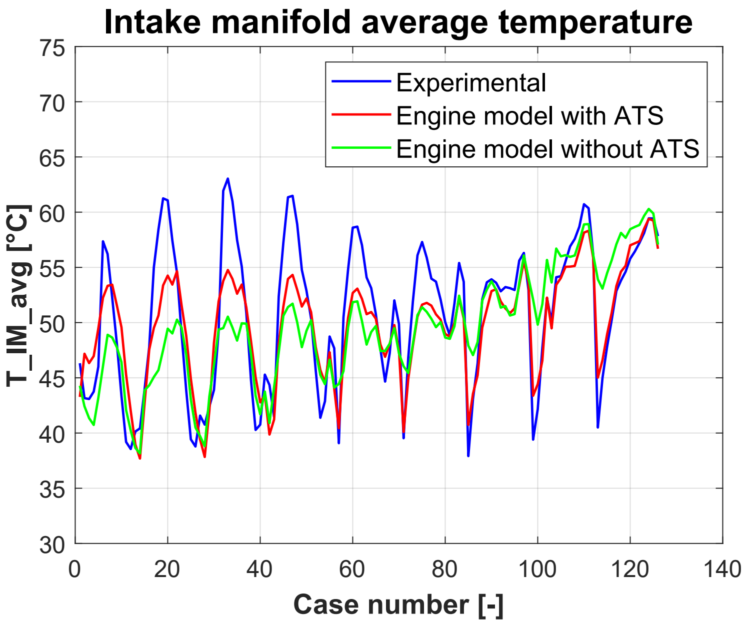

Figure 4.5: Comparison of T_IM_avg of the two engine models.

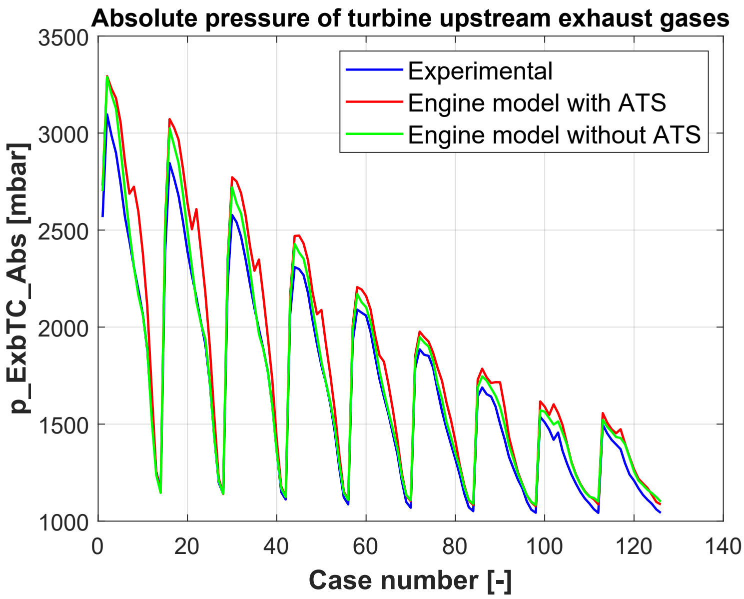

Figure 4.6: Comparison of p_ExbTC_Abs of the two engine models.

Concerning the absolute pressure inside the exhaust manifold (Figure 4.6), the simulated trends of both the engine model with ATS and the engine model without ATS are higher than the experimental one. In particular, the red trend is higher than the green one in many zones, exhibiting some singularities in the first four decreasing slopes. The responsible thing of this behavior, as it will be possible to observe in one of the next sections, is the thermal model adopted inside the exhaust pipes of the engine model with ATS. This thermal model is focused on the temperatures optimization, as can be seen in the next diagram, which shows the average temperature of the exhaust manifold (Figure 4.7). The red trend follows well the experimental one, even if in some parts there is a little underestimation and in others a little overestimation. However, it is surely better than the simulated trend given by the engine model without ATS, that overestimates a lot the temperature inside the exhaust manifold. The same reasoning can be extended to the temperature of the gases at the turbine downstream (Figure 4.8), which is estimated much better by the engine model with ATS.

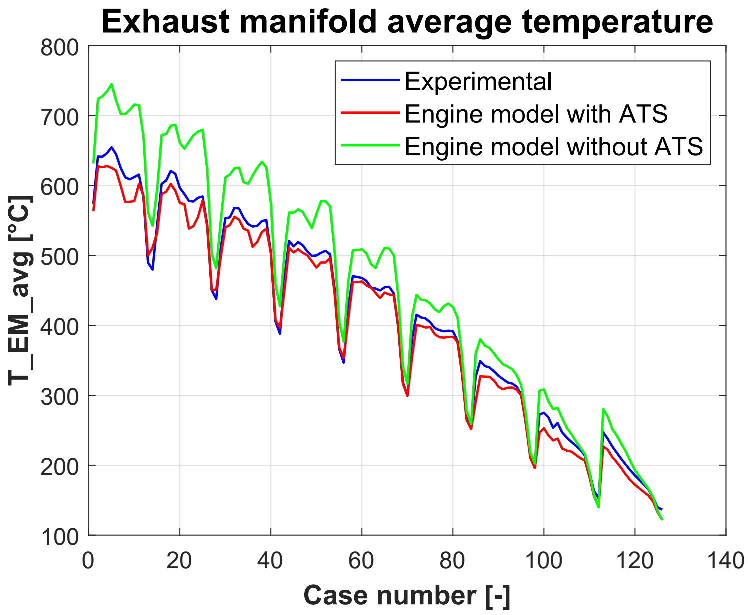

Figure 4.7: Comparison of *T_EM_avg* of the two engine models.

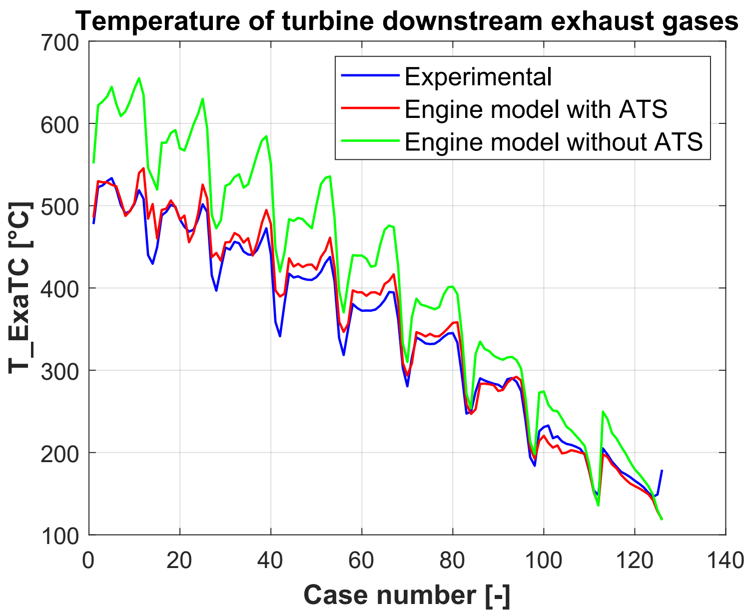

Figure 4.8: Comparison of *T_ExaTC* of the two engine models.

Having seen directly the comparison between the two engine models about these two temperatures, it is worth remembering that one of the main goals of this thesis is to improve the estimate of these temperatures provided by the engine model without ATS. However, this improvement will be realized exploiting a more physical approach about the thermal modeling adopted inside the exhaust pipes.
The next group of quantities that exhibit a relevant difference between the two engine models regards three quantities related to the single cylinder: the maximum pressure inside the combustion chamber, the net indicated mean effective pressure and the pumping mean effective pressure. Even this time the priority is given to the third cylinder, which shows the best estimate of the experimental trends. These three quantities are estimated better by the engine model without ATS, and this is confirmed by looking at the *RMSE* values, reported in Table 4.2. The *PMAX3* simulated trend (Figure 4.9) given by the engine model with ATS underestimates more than the green trend in many zones, especially in the upper peaks at high loads. Even about the *IMEP3* (Figure 4.10) it is possible to do the same reasoning, with the only difference that at low loads

the two simulated trends overlap and both give a slight underestimation of the quantity.
About the pumping mean effective pressure *IMEPL3*, reported in Figure 4.11, an interesting detail can be observed. Looking at the related $RMSE$ values, the engine model without ATS gives a better estimate. However, focusing on the first three upper peaks, the green trend is higher than the red and the experimental ones. Furthermore, on these peaks, the green trend assumes positive values. Since the gross indicated mean effective pressure is given by the difference between the net indicated and the pumping mean effective pressure, it is not closer to the experimental results like the *IMEP3*, but it is more or less equivalent to the one of the engine model with ATS. In fact, the *IMEPH3* of the engine model without ATS roughly overlaps with the one of the other engine model, giving the same level of underestimation, because it is decreased by the *IMEPL3* that, on the contrary of the *IMEP3*, is overestimated in these first three peaks. For this reason, the plot of *IMEPH3* is not shown, because of the insignificant difference between the two simulated trends, not even at high loads.

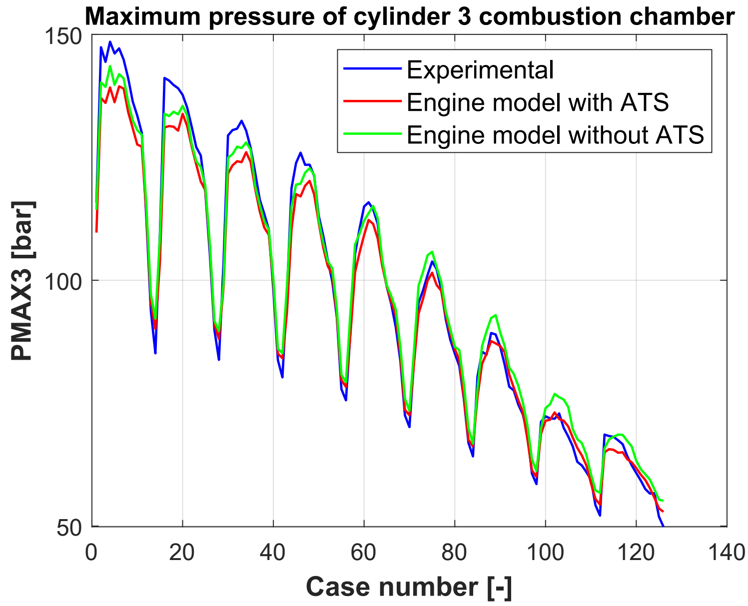

Figure 4.9: Comparison of *PMAX3* of the two engine models.

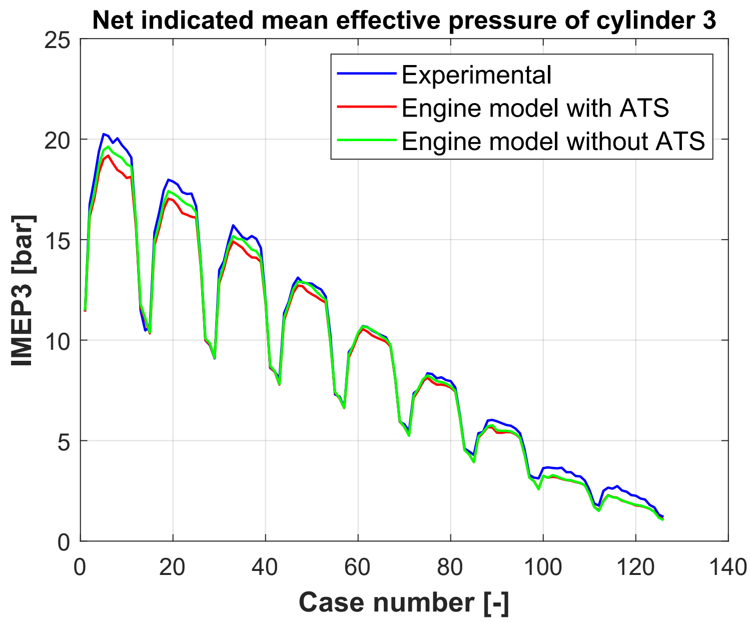

Figure 4.10: Comparison of *IMEP3* of the two engine models.

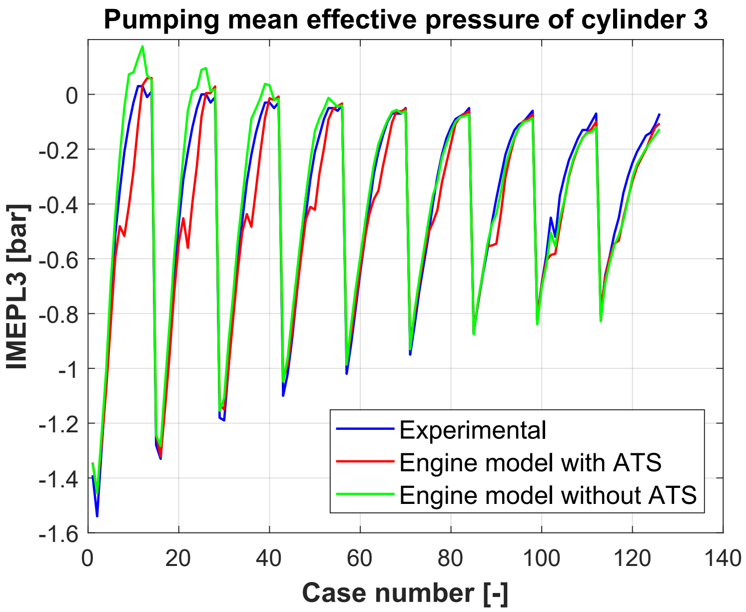

Figure 4.11: Comparison of *IMEPL3* of the two engine models.

	Engine model with ATS	Engine model without ATS
BMEP	0.999	0.999
T_IM_avg	0.881	0.668
p_ExbTC_Abs	0.995	0.998
T_EM_avg	0.998	0.998
T_ExaTC	0.993	0.994
PMAX3	0.996	0.997
IMEP3	0.999	0.999
IMEPL3	0.977	0.988

Table 4.1: Squared correlation coefficients R^2 of the engine model with ATS and of the engine model without ATS.

	Engine model with ATS	Engine model without ATS
BMEP	0.343 bar	0.242 bar
T_IM_avg	3.415 °C	5.127 °C
p_ExbTC_Abs	161.145 mbar	72.539 mbar
T_EM_avg	15.608 °C	50.337 °C
T_ExaTC	17.424 °C	71.272 °C
PMAX3	3.987 bar	3.401 bar
IMEP3	0.535 bar	0.353 bar
IMEPL3	0.094 bar	0.062 bar

Table 4.2: Root mean square errors $RMSE$ of the engine model with ATS and of the engine model without ATS.

Regarding the R^2 and the $RMSE$ values, they are respectively reported in Tables 3.1 and 3.2. The squared correlation coefficients, with the only exception of the average temperature inside the intake manifold, turn out to be very similar between the two engine models. The evidence of the difference between the two engine models can be detected by observing the $RMSE$ values, that are all consistent with the reasonings carried out in the previous diagrams analysis. In summary, looking at these values, the engine model with ATS estimates the temperatures much better. Instead, the other model gives more reliable results about the remaining quantities that have been analyzed above, i.e. the *BMEP* and the quantities related to the single cylinder. About the quantities that are not reported, it is possible to state that they have a very similar behavior between the two engine models, so understanding which ones are estimated better by a model or another is less important.

4.3 Differences between the two engine models

Since the comparison between the two engine models was executed and some important differences were noticed about the simulation results, it is necessary to investigate to which causes these dissimilarities are due. The causes coincide with some differences inside the two engine models themselves, which were carefully researched inside the GT-ISE environment, comparing block by block. The main diversities that have been found regard:

- The thermal model inside the exhaust pipes;
- the open-loop chain of the flap;
- the imposed length of the intercooler pipes;
- the engine effective rotating inertia.

Each of these differences will be analyzed, showing directly the content of each GT-ISE block involved for both the engine models.

4.3.1 Thermal model inside the exhaust pipes

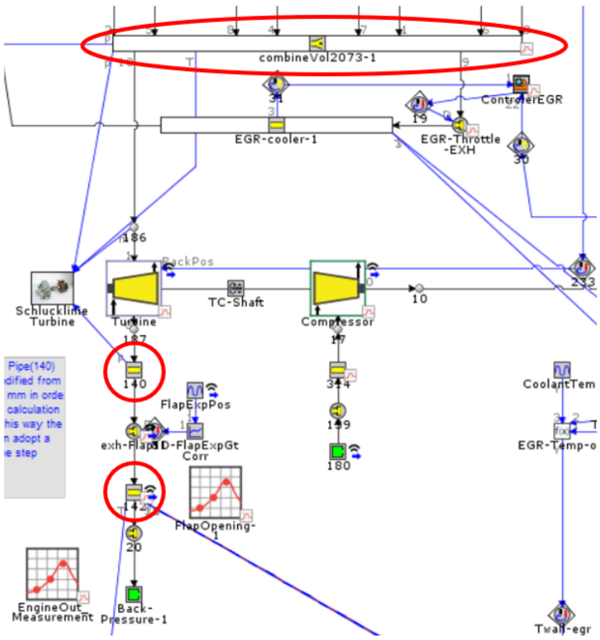

Figure 4.12: Exhaust pipes blocks.

The first difference concerns the thermal model inside the exhaust pipes. The latter are highlighted in Figure 4.12 and are the exhaust manifold, which is the block called "*combineVol2073-1*", the pipe "*140*" downstream of the turbine and the pipe "*142*" downstream of the flap. These three blocks have equivalent fields inside the thermal section, shown in Figure 4.13. In particular, in Figure 4.13(a), the thermal section of the exhaust pipes of the engine model with ATS is reported, while in Figure 4.13(b) there is the one of the exhaust pipes of the other engine model. The difference between them is directly highlighted, and it regards the *Wall External Boundary Conditions*

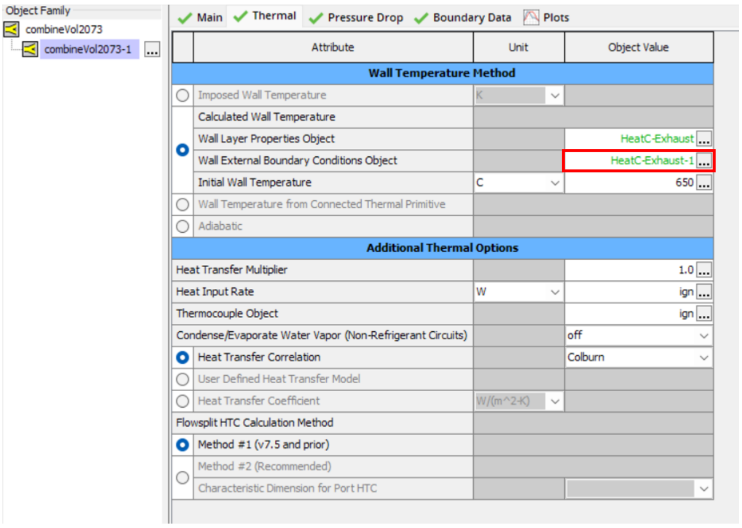

(a)

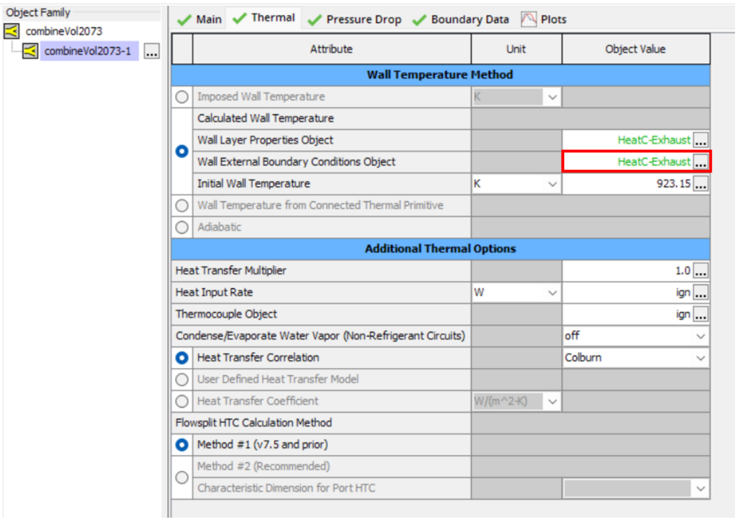

(b)

Figure 4.13: Thermal section of the exhaust pipes of the engine model with ATS **(a)** and of the engine model without ATS **(b)**.

Object. This field is dedicated to the definition of the external environment temperature and of the coefficient of the heat convective exchange with the surroundings.
The two wall external boundary conditions objects are shown in Figure 4.14. This type of object is made up of three fields. The first two concern the convective and radiation temperature of the external environment, while the remainder regards the external convection coefficient. Between the two engine models both the convective and radiation temperatures differ of 5 °C. In fact, the convective temperatures are respectively 80 °C and 85 °C, while the radiation ones 85 °C and 90 °C. However, the main difference lies in the External Convection Coefficient (ECC). This coefficient for the engine model with ATS is defined by a three-dimensional map, while for the engine model without ATS by a single numerical value. For simplicity it is better to start discussing about the external convection coefficient of the second model, because the one of the engine model with ATS requires further investigation.
The wall external boundary conditions object of the engine model without ATS has as external convection coefficient a value equal to $7.5\frac{W}{m^2K}$, which is included in the experimental range of the convective heat transfer coefficient for the air in natural convection, i.e. $5 \div 25\frac{W}{m^2K}$. The air is the fluid that surrounds the exhaust pipes of the engine and therefore it must be taken into account.

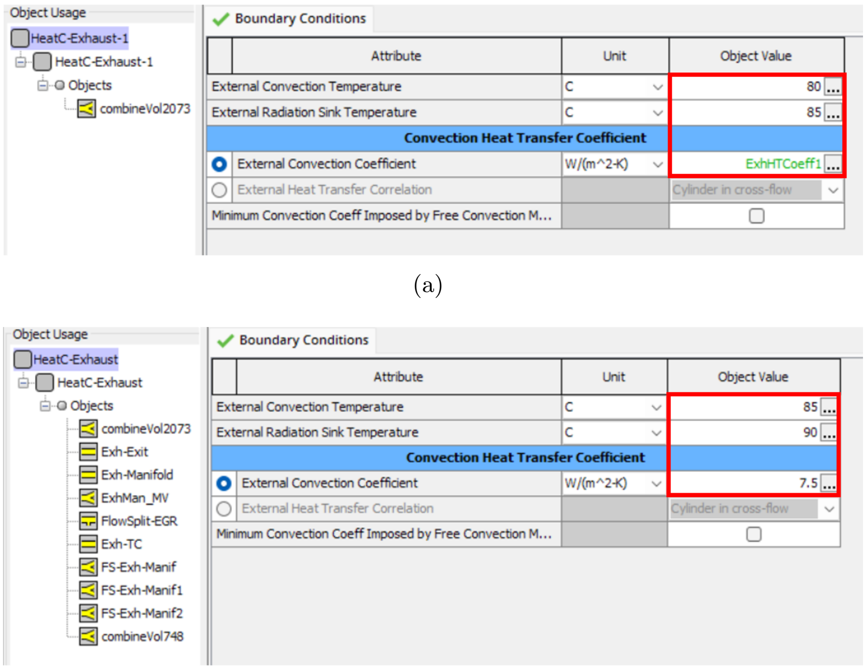

(a)

(b)

Figure 4.14: Wall external boundary conditions object of the engine model with ATS **(a)** and of the engine model without ATS **(b)**.

Regarding the wall external boundary conditions object of the engine model with ATS, rather than a single numerical value, a three-dimensional map is adopted for the external convection coefficient. This map is shown in Figure 4.15 and it exhibits the numerical values of the external convection coefficient as a function of the engine speed and BMEP. However, many of these values are not included in the experimental range of natural convection of the air, but are much higher. In this way, they do not have a physical consistency. To realize the order of magnitude reached by this group of values, it can be useful to examine the related diagram.

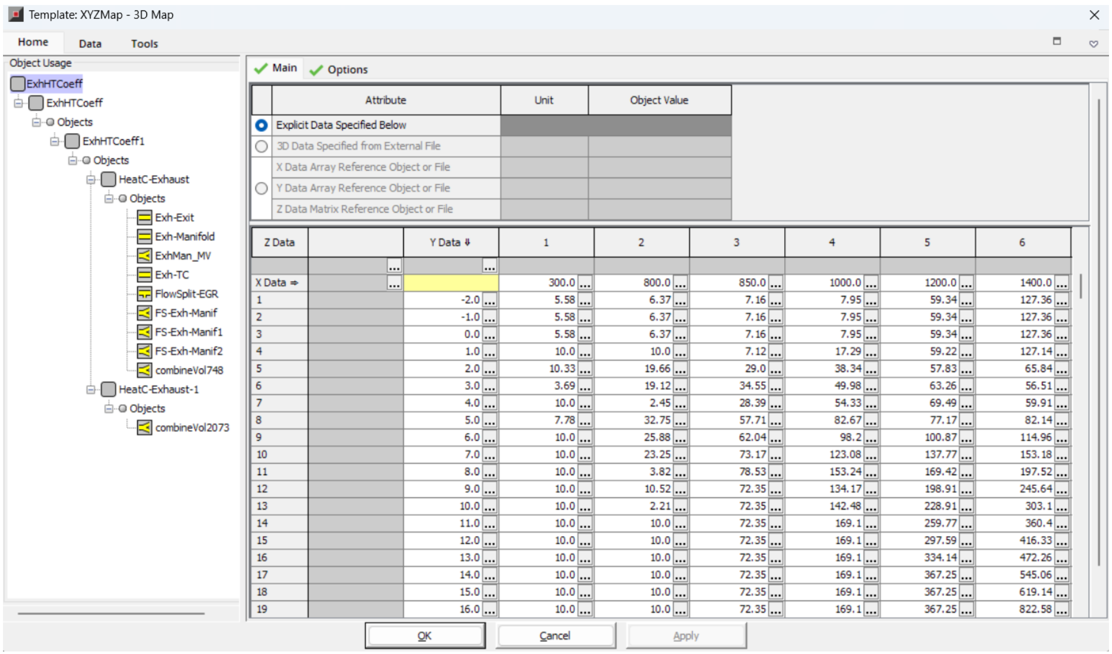

Z Data		Y Data ⇓	1	2	3	4	5	6
X Data ⇒			300.0	800.0	850.0	1000.0	1200.0	1400.0
1		-2.0	5.58	6.37	7.16	7.95	59.34	127.36
2		-1.0	5.58	6.37	7.16	7.95	59.34	127.36
3		0.0	5.58	6.37	7.16	7.95	59.34	127.36
4		1.0	10.0	10.0	7.12	17.29	59.22	127.14
5		2.0	10.33	19.66	29.0	38.34	57.83	65.84
6		3.0	3.69	19.12	34.55	49.98	63.26	56.51
7		4.0	10.0	2.45	28.39	54.33	69.49	59.91
8		5.0	7.78	32.75	57.71	82.67	77.17	82.14
9		6.0	10.0	25.88	62.04	98.2	100.87	114.96
10		7.0	10.0	23.25	73.17	123.08	137.77	153.18
11		8.0	10.0	3.82	78.53	153.24	169.42	197.52
12		9.0	10.0	10.52	72.35	134.17	198.91	245.64
13		10.0	10.0	2.21	72.35	142.48	228.91	303.1
14		11.0	10.0	10.0	72.35	169.1	259.77	360.4
15		12.0	10.0	10.0	72.35	169.1	297.59	416.33
16		13.0	10.0	10.0	72.35	169.1	334.14	472.26
17		14.0	10.0	10.0	72.35	169.1	367.25	545.06
18		15.0	10.0	10.0	72.35	169.1	367.25	619.14
19		16.0	10.0	10.0	72.35	169.1	367.25	822.58

Figure 4.15: Map of the external convection coefficients.

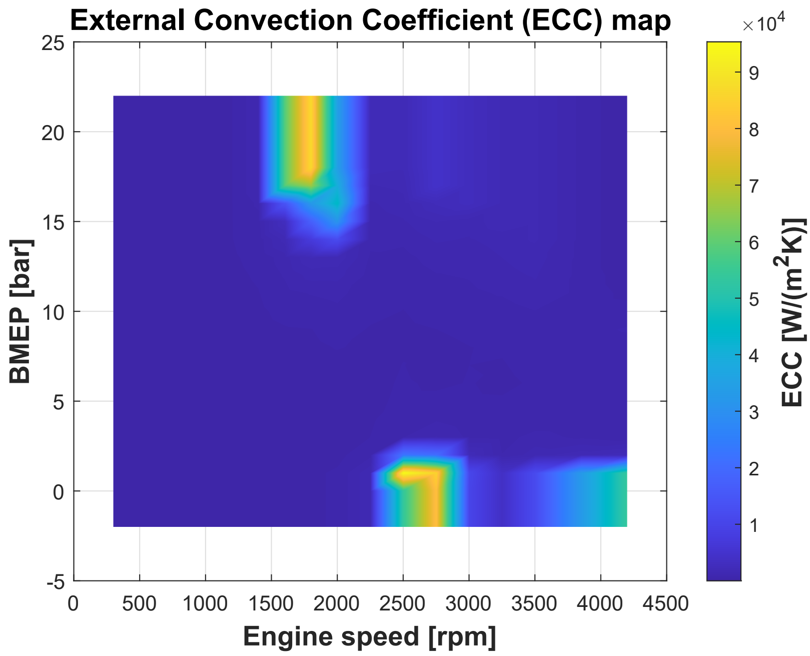

Figure 4.16: Diagram of the external convection coefficients.

The diagram of the external convection coefficients (Figure 4.16) is a plot of the map shown in Figure 4.15. Hence, in the abscissa there is the engine speed, while in the ordinate the *BMEP*. Subsequently, the third quantity is the external convection coefficient, in the form of a color map, whose bar on the right includes upper values that are greater than 9×10^4. The aim of this diagram is not to show the ECC values point by point, but to provide in a qualitative way the order of magnitude that these values reach. It is also interesting to note that the highest external convection coefficients are in an engine speed range of $1500 \div 3000$ rpm and at high and low loads. In this way, the temperatures are optimized consistently. In fact, in the cases characterized by high and low speeds and medium loads, the simulated temperatures overestimate the corresponding experimental trends, due to the lower amount of heat exchange with the surroundings.
The values of external convection coefficient exploited in the engine model with ATS do not have a physical consistency, but can be defined as ignorance coefficients, with the aim to optimize as much as possible the simulated temperatures behavior, simulating a huge heat transfer towards the external environment far from the physical reality. Since in this engine model there is an After Treatment System, it is very important to ensure an optimal prediction of the experimental temperatures, and for this reason this approach is used.

4.3.2 Open-loop chain of the flap

Another relevant difference that was detected between the two engine models is in the open-loop chain of the flap, highlighted in Figure 4.17. The flap valve is a very important device of the turbo-group, because it has the aim to control the back-pressure waves of the exhaust gases. These waves cause a resistance against a flow rate, in this case the exhaust gases one. The main cause of this phenomenon is the presence of restrictions, which are of the tailpipe and all the components of ATS. The presence of back-pressure waves determines an incorrect engine operation, causing an increase in fuel consumption. These waves also bring an enhancement of the emissions, due to an irregular flow rate inside the ATS, which consequently do not operate correctly. How the flap system is modeled in the GT-ISE environment was explained in Chapter 2. Here the focus is on the dissimilarities that this sub-system has between the two engine models. The first difference is inside the signal generator block, shown in Figure 4.18.
In the signal generator of the engine model with ATS the reference object is a three-dimensional map, with the same dependence of all three-dimensional maps described so far, i.e. on the engine

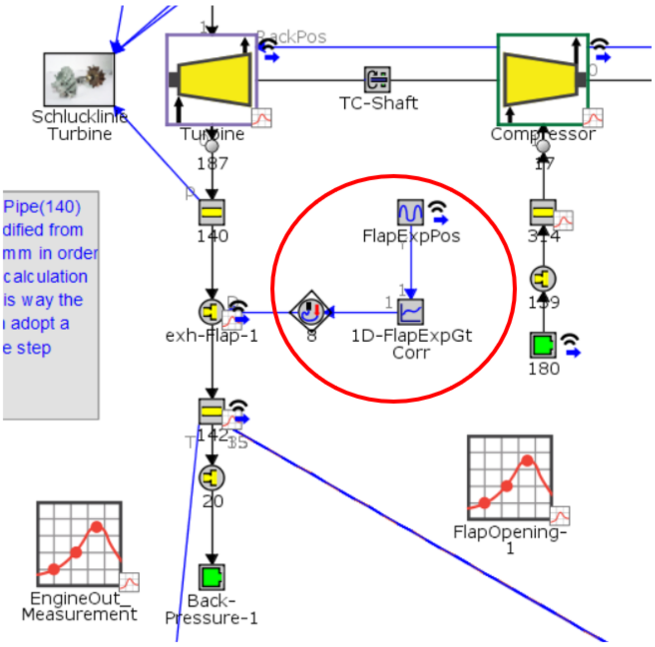

Figure 4.17: Flap open-loop chain.

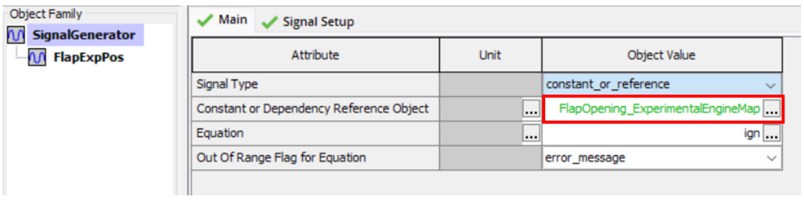

(a)

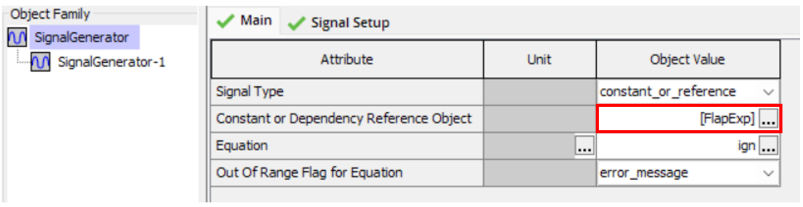

(b)

Figure 4.18: Flap signal generator of the engine model with ATS **(a)** and of the engine model without ATS **(b)**.

speed and *BMEP*. As values, there are the relative flap closing, included in the range between 0 and 1.

The engine model without ATS exhibits directly the experimental flap closing, in this case in percentage, inside the flap signal generator. It is about the percentage values of the flap valve closing test by test, so case by case. These are shown in Figure 4.19 and it can be noted that the trend is characterized by a series of peaks. There is a global increase of the peak values, which can be explained by the decrease of the mass flow rate of the exhaust gases. The latter, even if they have not been shown, are substantially characterized by the same trend of the wet and dry air mass flow rates. As shown in the previous chapters, this trend globally decreases with the increase of the case number. When the mass flow rate is low, there is priority to preserve it from the back-pressure waves with a greater closing of the flap valve. The flap closing peaks, especially the ones that have a greater magnitude than the ones at lower case numbers, coincide with the minima of the exhaust gases mass flow rate and of the pressure at the flap upstream, hence of the pressure of exhaust gases at turbine downstream. In fact, even with a low pressure at the flap upstream, there is less thrust on the exhaust gases flow rate, which is already small. Therefore, the flap must be closer so that the exhaust gases are not hindered by the back-pressure waves.

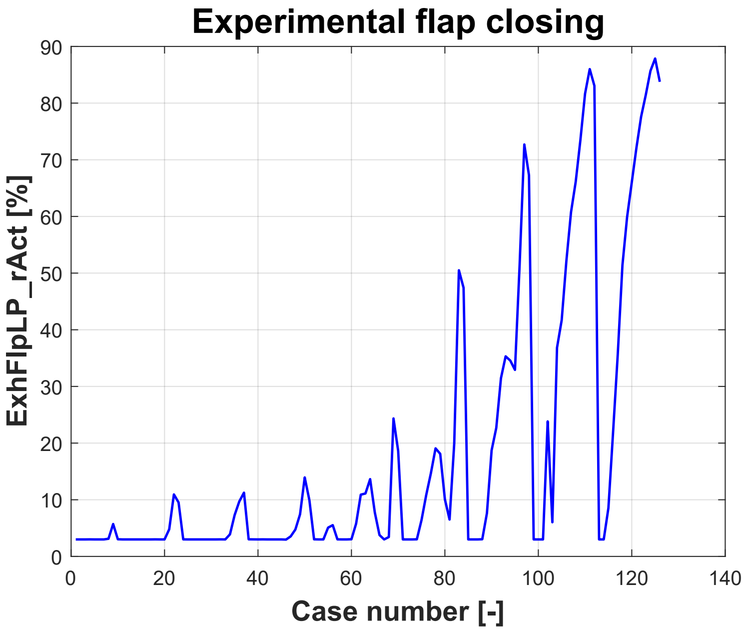

Figure 4.19: Experimental flap closing.

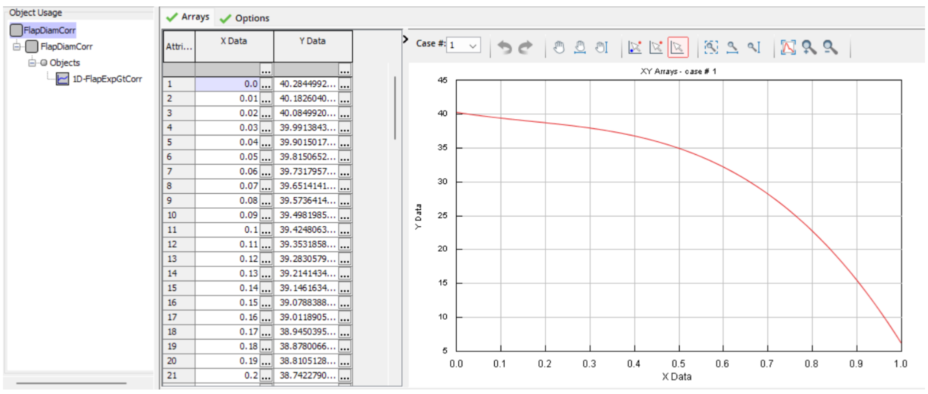

(a)

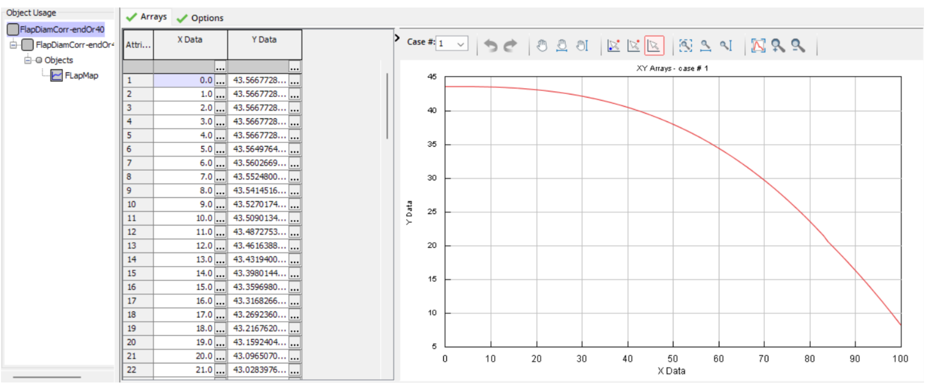

(b)

Figure 4.20: Flap correlation of the engine model with ATS **(a)** and of the engine model without ATS **(b)**.

The second difference that characterizes the open-loop chain of the flap is the correlation block, reported in Figure 4.20. In particular, the dissimilarity consists in the correlation function. This

function is necessary to convert the input of the correlation block, which is the flap closing signal, into a hole diameter, whose value is supplied to the valve block by the actuator.
Analyzing more in detail, the X data of the correlation function of the engine model with ATS are from 0 to 1, while the ones of the engine model without ATS are from 0 to 100. There is only a difference in the numerical definition, but the meaning is the same. Both functions have a monotonical trend, which decreases enhancing the flap closing. The correlation of the second model (Figure 4.20(b)) shows a higher curvature and greater diameter values both for high and low flap closing. This is another element of optimization that characterizes the engine model without ATS.

4.3.3 Imposed length of the intercooler pipes

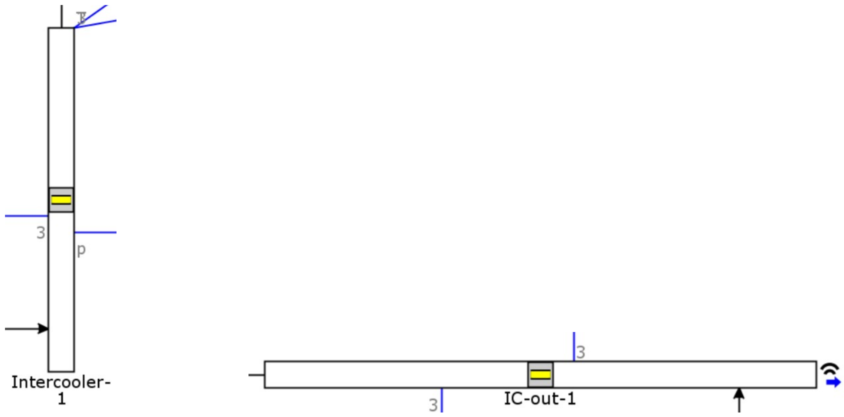

(a) (b)

Figure 4.21: Intercooler:**(a)** first pipe object; **(b)** second pipe object.

The third difference between the two engine models regards the length of the intercooler pipes (Figure4.21). As observed in chapter 2, in the GT-ISE environment the intercooler system is made up of two pipes: the first pipe is called "*Intercooler-1*", while the second one is named "*IC-out-1*". The intercooler pipe object has already been analyzed, describing all its fields. Here the focus is on the difference that this object exhibits between the two engine configurations. The dissimilarity is about the pipe length, which increases for both intercooler pipes going from the engine model with ATS to the one without ATS.

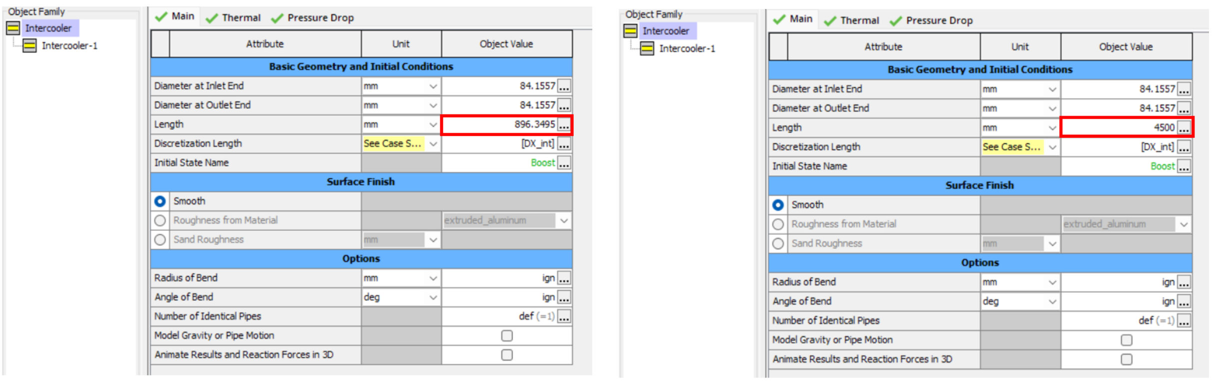

(a) (b)

Figure 4.22: "*Intercooler-1*" block of the engine model with ATS **(a)** of the engine model without ATS **(b)**.

Considering the "*Intercooler-1*" pipe (Figure 4.22), the length is 896.3495 mm for the engine model with ATS, while for the other model is 4500 mm. Instead, regarding the "*IC-out-1*" pipe

(Figure 4.23), there is a length of 1017.0353 mm for the first engine model, while a length of 1500 mm for the second one. Therefore, the amount of variation between the lengths is greater for the first intercooler pipe. It will be possible to observe the influence of this difference of the intercooler pipes length, as the one of all the other diversities, in the next section.

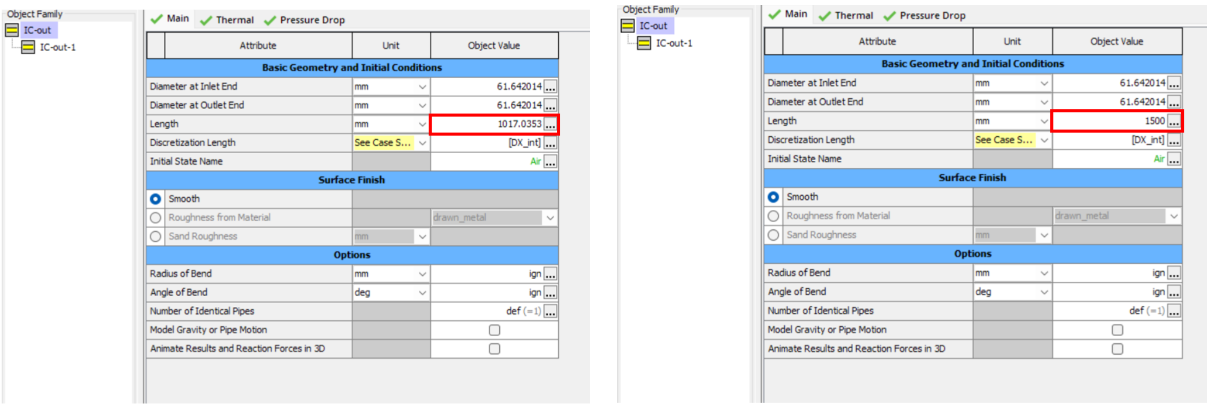

(a) (b)

Figure 4.23: "*IC-out-1*" block of the engine model with ATS **(a)** of the engine model without ATS **(b)**

4.3.4 Engine effective rotating inertia

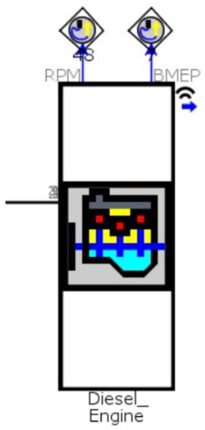

Figure 4.24: Engine cranktrain.

The last difference is inside the cranktrain block (Figure 4.24), in particular, into the section reserved for the engine inertia. This section has as field the "Engine Effective Rotating Inertia", which must be specified by a numerical value. This parameter represents the stored kinetic energy of the engine before the application of a braking torque. Actually, this parameter, in the case of a simulation with a prescribed constant speed, can be ignored. In both engine models a constant speed is imposed in each steady-state test, and no influence is expected about the engine effective rotating inertia. In the next section this behavior will be confirmed. However, these two models are suitable also for a simulation in transient conditions, where the engine effective rotating inertia becomes relevant and for this reason is not ignored but is specified with a numerical value.
The engine model with ATS has the inertia value equal to 0.3 $kg \cdot m^2$ (Figure 4.25(a)), while in the second engine model it is equal to 1.5 $kg \cdot m^2$ (Figure 4.25(b)).

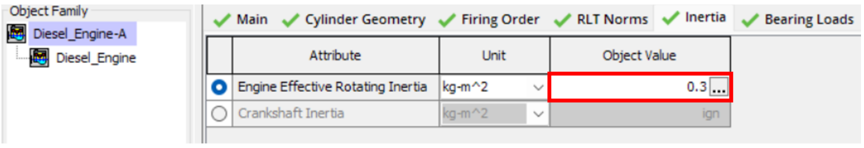

(a)

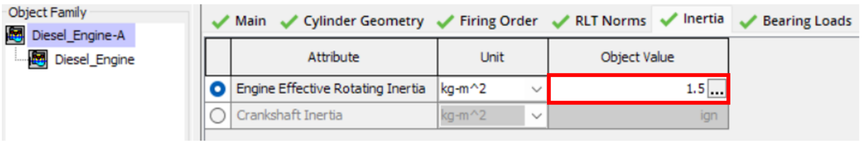

(b)

Figure 4.25: Engine cranktrain object of the engine model with ATS **(a)** and of the engine model without ATS **(b)**.

4.4 Effect of each difference on each engine model

Now that the four differences have been carefully examined, it is very useful to understand which impact they have on each engine configuration. This effect can be evaluated separately for each difference through a reciprocal exchange between the two engine models.
For instance, considering the first difference, the wall external boundary conditions object of the engine model with ATS is inserted into the engine model without ATS, creating in this way a new configuration without ATS. Viceversa, the wall external boundary conditions object of the engine model without ATS is inserted inside the engine model with ATS, making a new configuration of the latter. So, a simulation can be run with each one of these new engine layouts.
The same logic can be adopted for the other three differences. Therefore, the open-loop chains of the flap, the length of the two intercooler pipes, the values of the engine effective rotating inertia can be interchanged, creating two new engine configurations for each difference.
The new engine configurations are eight, since the evaluated differences are four. Hence, eight simulations were run, and for each of them all the important engine quantities can be analyzed. Furthermore, to detect the impact of every difference on the engine model with ATS and on the one without ATS, the relative variations in percentage of R^2 and $RMSE$ were computed according to the equations 4.1 and 4.2.

$$\Delta R^2[\%] = \frac{R^2_{final} - R^2_{initial}}{R^2_{initial}} \cdot 100 \tag{4.1}$$

$$\Delta RMSE[\%] = \frac{RMSE_{final} - RMSE_{initial}}{RMSE_{initial}} \cdot 100 \tag{4.2}$$

$R^2_{initial}$ and $RMSE_{initial}$ values refer to the starting engine configuration, where no modification about the differences has been actuated. Instead, R^2_{final} and $RMSE_{final}$ values refer to each of the new engine configurations.
Some diagrams in which these variations can be visualized for each engine quantity were made. However, only the ones about the $RMSE$ relative variations are reported, because the R^2 ones are negligible in magnitude and consequently are not representative of the differences influence. According to their definitions, a positive $\Delta RMSE$ means a worsening of the related quantity, while a negative $\Delta RMSE$ indicates an improvement of it.
In Figure 4.26 the $RMSE$ relative variations in percentage for the first ten engine variables are shown. There are two diagrams, one reserved for the engine model with ATS (Figure 4.26(a)) and the other for the engine model without ATS (Figure 4.26(b)). Every difference is indicated with a specific color and with a precise denomination. The first difference, i.e. the one related to the thermal model of the exhaust pipes, is indicated as "Exh_Thermal". The difference related to the open-loop control of the flap is displayed as "Flap". The diversity about the length of the

intercooler pipes in the legend has the name "ICL". Finally, the difference linked to the engine effective rotating inertia is indicated simply with the name "Inertia".

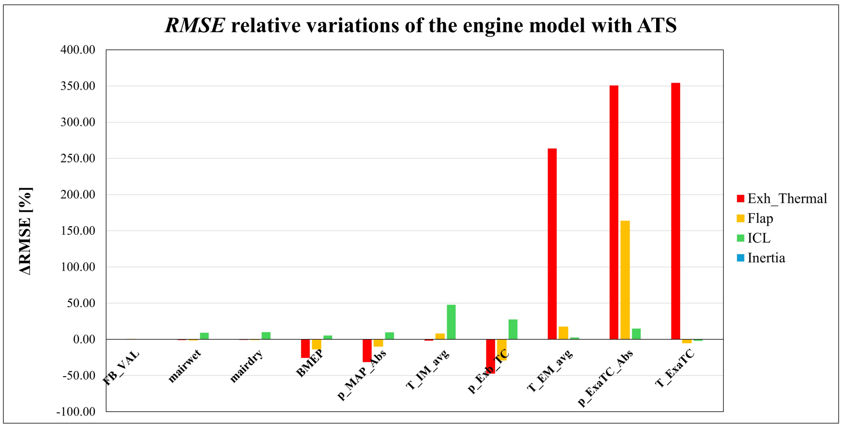

(a)

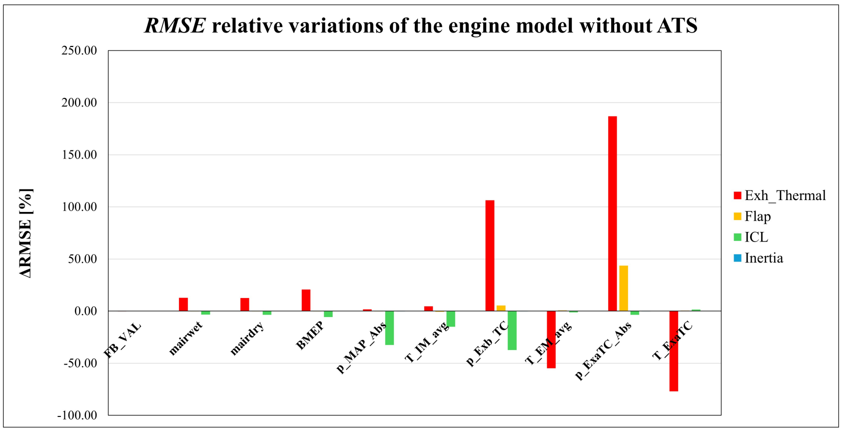

(b)

Figure 4.26: *RMSE* relative variations due to the four differences of the first ten quantities of the engine model with ATS **(a)** and of the one without ATS **(b)**.

Analyzing both plots, it can be noted that the most influent difference is the thermal model of the exhaust pipes. In particular, the greatest amount of variation is detected for the thermodynamic quantities of the exhaust pipes, i.e. the pressures and the temperatures at the turbine upstream and downstream. The thermal model adopted in the engine configuration without ATS leads to a worsening of the experimental estimate for the pressure at the turbine downstream and for the temperatures at the turbine upstream and downstream of the engine model with ATS. In fact, the map of the heat exchange coefficients was adopted with the main goal to align the simulated temperatures with the experimental ones. A so different model like the one adopted in the engine layout with ATS leads to a result very far from the beginning one. In contrast, the thermal model of the engine configuration with ATS improves the pressure at the turbine upstream. The map of the heat exchange coefficients did not give priority to the pressure inside the exhaust manifold, but only to the temperatures, so the pressure of the exhaust manifold did not follow well the experimental trend.
It can be noted that also the *BMEP* is improved by the thermal model based on a single numerical value, so this is the reason why the engine layout without ATS is optimized for the experimental prediction of this quantity. Hence, it is possible to appreciate the performance of this differences analysis: adopting the method of reciprocal exchange of each difference, the advantages and disadvantages of each of the two engine models can be discovered.
The thermal model based on the map of coefficients consistently improves the temperatures at the turbine upstream and downstream, observing the reduction of *RMSE*, but deteriorates the

pressures, since this thermal model is not optimized for the latter. Even the air mass flow rates and the *BMEP* are made worse.
Regarding the flap difference, the open-loop chain of the engine model without ATS deteriorates the pressure at the turbine downstream of the engine configuration with ATS. The open-loop chain of the layout with ATS also makes worse the *p_ExaTC_Abs* of the model without ATS, but in less extent.
Concerning the other two differences, the influence is minor, especially for the inertia, confirming what was said above: the engine effective rotating inertia, in a simulation with imposed speed in steady-state conditions, has a negligible effect. About the pipe length of the intercooler blocks, having longer pipes like in the engine model without ATS causes a worse experimental estimate of the reported quantities of the layout with ATS. In contrast, a shorter length is beneficial, seeing the effect on the engine configuration without ATS.
The only quantity that is immune to each difference is the average fuel consumption *FB_VAL*, since it is imposed in both engine models.

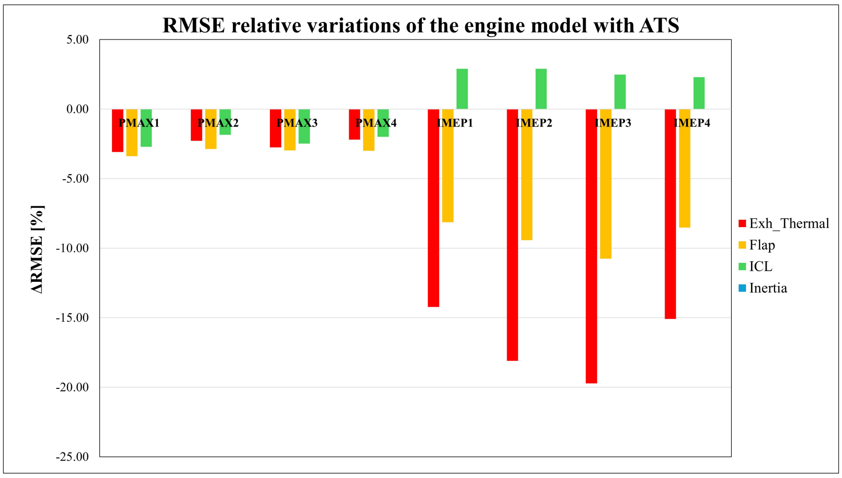

(a)

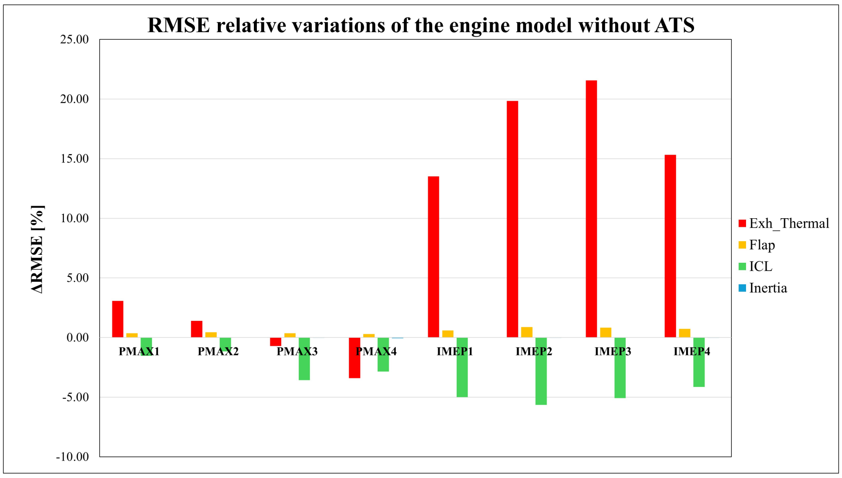

(b)

Figure 4.27: *RMSE* relative variations due to the four differences of the *PMAXi* and *IMEPi* quantities of the engine model with ATS **(a)** and of the one without ATS **(b)**.

In Figure 4.27 the *RMSE* variations of the maximum in-cylinder pressures and of the net indicated mean effective pressures of all cylinders are shown. It can be immediately noticed in Figure 4.27(a) that the thermal model of the exhaust pipes, the open-loop control of the flap and the intercooler pipes length of the engine model without ATS is beneficial for the *PMAX* of all cylinders. Hence, this is the reason why the engine layout without ATS has a better behavior for this quantity. Even

the net indicated mean effective pressures exhibit an improvement, much higher than the $PMAX$ of all cylinders. This reduction of the $RMSE$ values is due to the thermal model of the exhaust pipes and the flap open-loop chain. Instead, the length of the intercooler pipes deteriorates the $IMEP$ of all cylinders.
Observing the diagram of Figure 4.27(b), there is only a partial coherence with the plot reserved to $\Delta RMSE$ of the engine model with ATS. In fact, the thermal model of the exhaust pipes based on the map of heat exchange coefficients makes worse the $IMEP$ quantities, but on the maximum pressure of the cylinders combustion chamber it does not have a univocal effect. Some of $PMAX$ quantities are a bit worsened and others a bit improved. Furthermore, the shorter length of the intercooler pipes is beneficial for all the quantities shown. Instead, the flap open-loop chain deteriorates a bit these engine quantities, consistently with the above diagram.

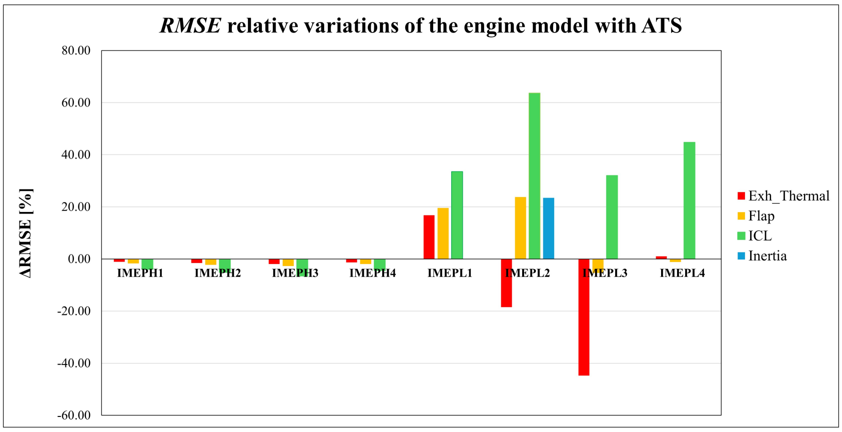

(a)

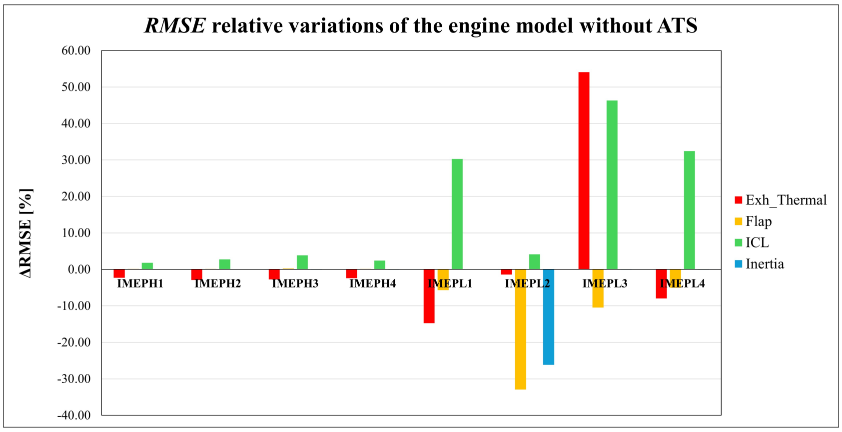

(b)

Figure 4.28: $RMSE$ relative variations due to the four differences of the $IMEPHi$ and $IMEPLi$ quantities of the engine model with ATS **(a)** and of the one without ATS **(b)**.

In the diagrams of the Figure 4.28 the differences effect on the gross mean effective pressures and on the pumping mean effective pressures of all cylinders is shown. Starting with $IMEPH$ quantities of the engine model with ATS, the characteristics of the other engine layout have a positive effect on them, even if the amount of improvement is small. The longer length of the intercooler pipes deteriorates the pumping mean effective pressures, while for the other differences there is not a univocal effect. Always about both $IMEPH$ and $IMEPL$, it is difficult to find a relation with the other diagram (Figure 4.28(b)). In fact, the characteristics of the engine layout with ATS do not have a consistent effect on the engine model without ATS, taking as reference the opposite case, reported in 4.28(a).
Analyzing the last couple of diagrams (Figure4.29), the total friction mean effective pressure of all cylinders substantially is not subjected to the influence of the four differences. This was expected

since the simulated quantity of *TFMEP* is defined by a dedicated computational model, that is the Chen-Flynn method, depending only on the engine speed. The turbo angular speed and the EGR percentages turn out to be enough robust to the differences. Instead, the boost pressure is pretty influenced. In particular, the thermal model based on a single numerical value of the external convection coefficient leads to a relevant improvement of the experimental prediction of *PCR_pDesVal*. This great improvement is also brought by the short length of the intercooler pipes, observing the diagram in Figure 4.29(b).

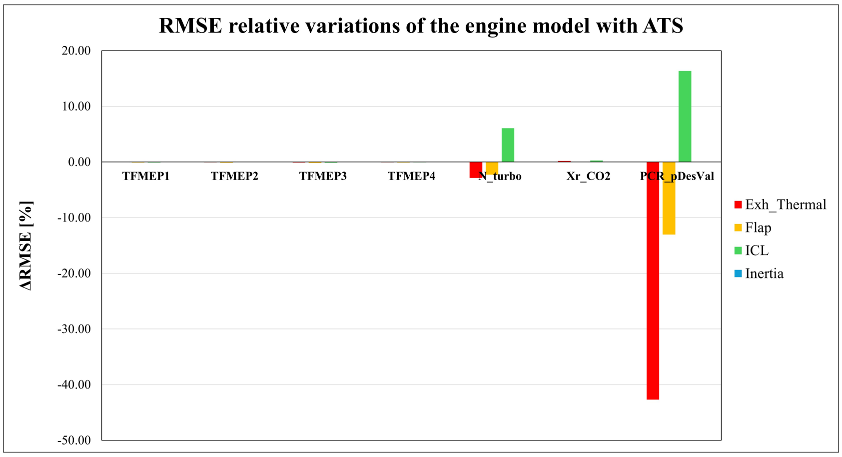

(a)

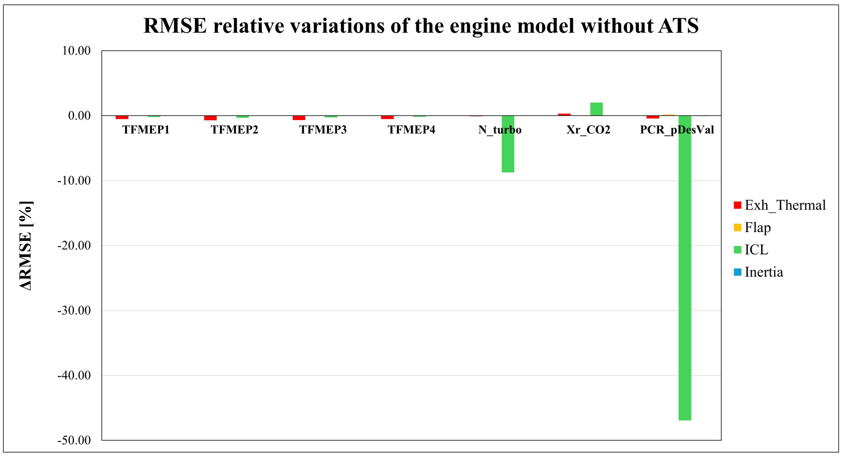

(b)

Figure 4.29: *RMSE* relative variations due to the four differences of the *TFMEPi* and last three quantities of the engine model with ATS **(a)** and of the one without ATS **(b)**.

Among all the engine quantities, the ones that show the greatest amount of variation are the absolute pressure of the exhaust manifold *p_ExbTC_Abs*, the exhaust manifold average temperature *T_EM_avg*, the absolute pressure of the exhaust gases at turbine downstream *p_ExaTC_Abs* and the average temperature of the exhaust gases at turbine downstream *T_ExaTC*. This great variation is due to the difference of the thermal model inside the exhaust pipes. Therefore, it is worth observing the trends of these variables as a function of the case number. In each plot, three trends are shown: the experimental one, the simulated one of the engine layout unchanged and the simulated one of the modified engine configuration. The modification regards the wall external boundary conditions object, following always the logic of reciprocal exchange between the two engine models, as explained previously.
In Figure 4.30 the exhaust manifold pressure of both engine configurations is shown. It can be noticed in Figure 4.30(a) that the thermal model based on a single numerical value is beneficial for the experimental estimate, in particular among the decreasing slopes of the trend and at the

upper peaks of low loads. Consistently, observing the Figure 4.30(b), the thermal model based on the map of the heat exchange coefficients leads to a worsening of the simulated trend behavior.

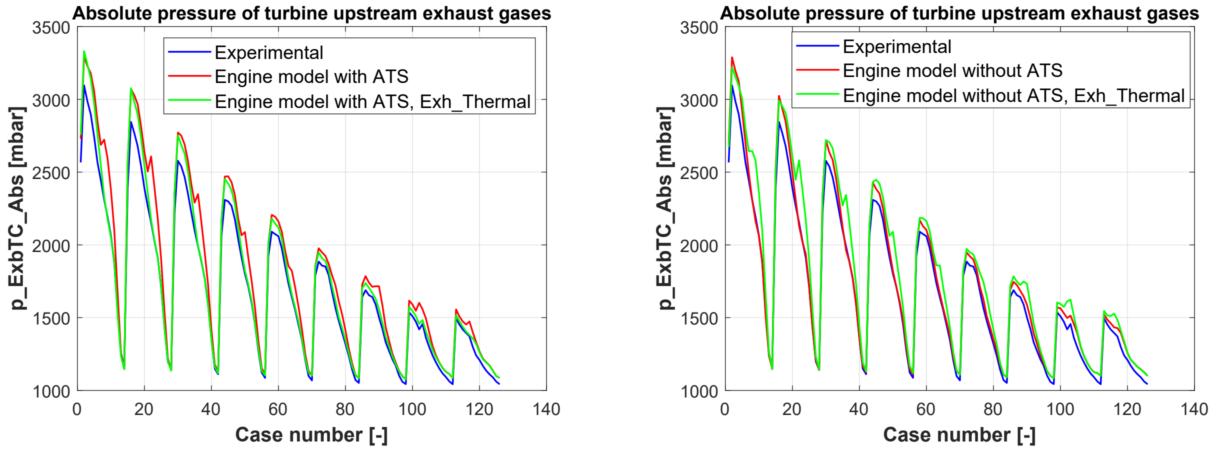

(a) (b)

Figure 4.30: Thermal model influence on *p_ExbTC_Abs* of the engine model with ATS **(a)** and of the engine model without ATS **(b)**

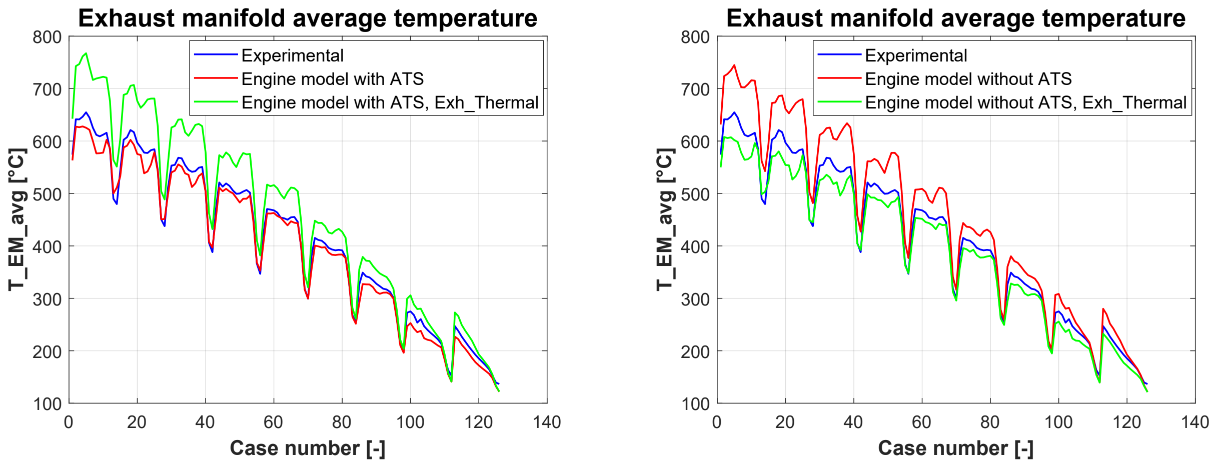

(a) (b)

Figure 4.31: Thermal model influence on *T_EM_avg* of the engine model with ATS **(a)** and of the engine model without ATS **(b)**

Regarding the average temperature of the exhaust manifold (Figure 4.31), the thermal model of the engine layout without ATS enhances the simulated temperature (Figure 4.31(a)), overestimating a lot the experimental quantity. Instead, the map of coefficients, optimized for the experimental prediction of the temperature, brings the simulated temperature of the engine model without ATS much closer to the experimental trend (Figure 4.31(b)).
Differently from the absolute pressure within the exhaust manifold, the absolute pressure at turbine downstream of both engine models is worsened by the thermal modification (Figure 4.32). In fact, the thermal model based on a single numerical value increases the simulated pressure of the engine layout with ATS (Figure 4.32(a)), increasing the gap from the experimental trend. Instead, the thermal model with the map of coefficients applied on the engine layout with ATS decreases the simulated pressure (Figure 4.32(b)), leading equally to an enhancement of the gap from the experimental values. So in both cases there is a worsening of the simulated *p_ExaTC_Abs*. The initial engine configurations exhibit a good experimental estimate of this quantity, and in fact they were not shown in the previous section reserved for the comparison of the two engine

models. Probably, this pressure was already optimized with the conditions of the initial engine configurations, and the use of another thermal model inside the exhaust pipes compromises the already good results.

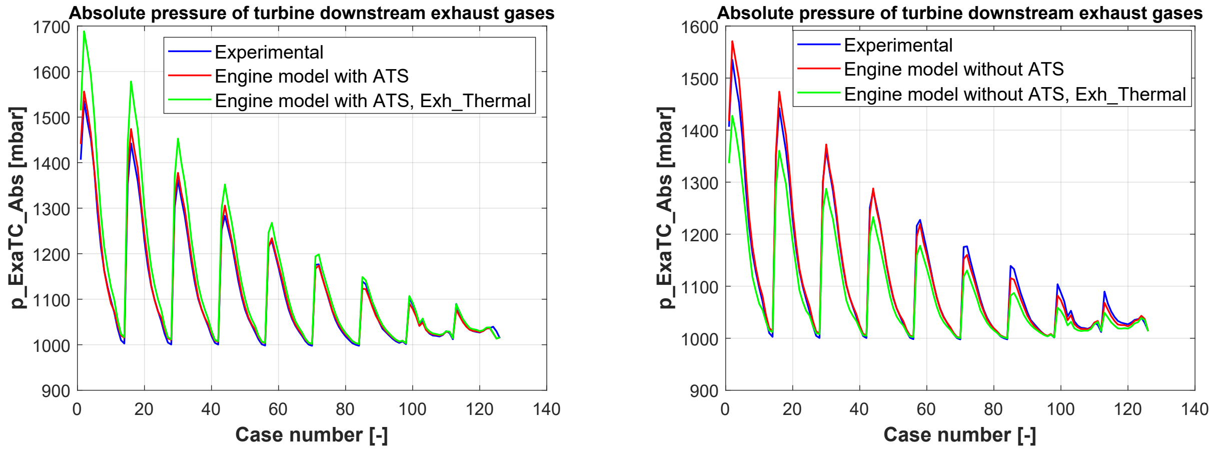

(a) (b)

Figure 4.32: Thermal model influence on *p_ExaTC_Abs* of the engine model with ATS **(a)** and of the engine model without ATS **(b)**

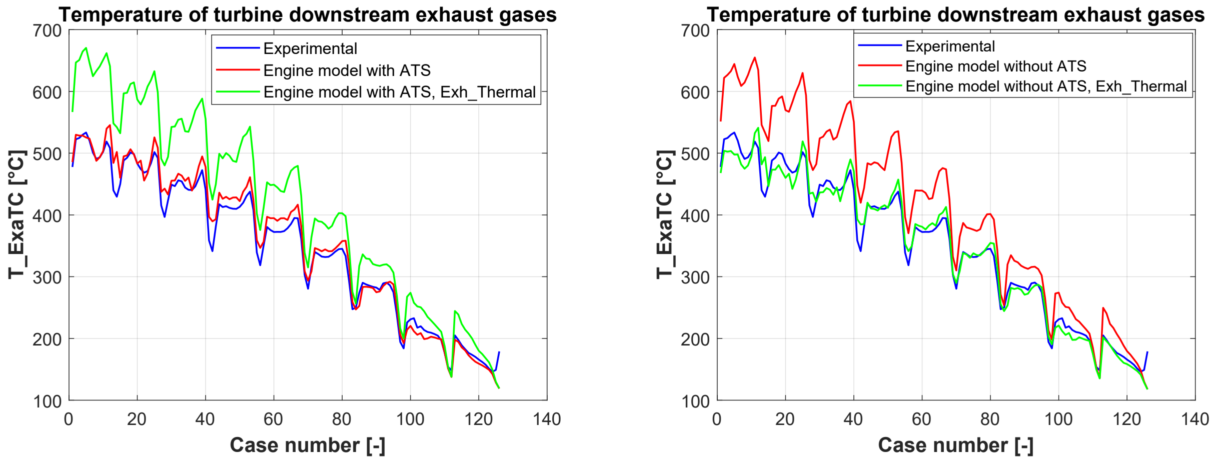

(a) (b)

Figure 4.33: Thermal model influence on *T_ExaTC* of the engine model with ATS **(a)** and of the engine model without ATS **(b)**

Finally, about the temperature at turbine downstream (Figure 4.33), the same phenomenon observed about the average temperature inside the exhaust manifold occurs, showing also a greater variation with the application of a different thermal model. It is possible to observe this in the next tables, where the $RMSE$ values and their relative variations in percentage are reported.
The tables of the R^2 values related to the engine model with ATS and the ones related to the engine configuration without ATS are 4.3 and 4.4 respectively. In each of these tables, the first column is dedicated to the initial engine configuration, while the second to the modified engine layout, where the thermal model has been changed. The R^2 values cannot represent the extent of the change, because their variation is almost negligible. However, they are reported for sake of completeness. To detect in a quantitative way the influence of the thermal model change it is possible to rely on the tables of the $RMSE$ values, i.e. 4.5 and 4.6. They have the same structural organization of the R^2 tables, but also showing a further column, in which there are the relative variations in percentage of the $RMSE$ values. The ΔR^2 values are not reported in the previous

R^2 tables due to their negligible amounts.

	Initial configuration	**Thermal model change**
p_ExbTC_Abs	0.995	0.998
T_EM_avg	0.998	0.998
p_ExaTC_Abs	0.999	0.997
T_ExaTC	0.993	0.996

Table 4.3: Squared correlation coefficients R^2 of the engine model with ATS: initial configuration (first column) and modified configuration (second column).

	Initial configuration	**Thermal model change**
p_ExbTC_Abs	0.998	0.993
T_EM_avg	0.998	0.997
p_ExaTC_Abs	0.997	0.997
T_ExaTC	0.994	0.990

Table 4.4: Squared correlation coefficients R^2 of the engine model without ATS: initial configuration (first column) and modified configuration (second column).

	Initial configuration	**Thermal model change**	**ΔRMSE**
p_ExbTC_Abs	161.415 mbar	85.278 mbar	-47.1687 %
T_EM_avg	15.608 °C	56.736 °C	+263.499 %
p_ExaTC_Abs	9.930 mbar	44.746 mbar	+350.618 %
T_ExaTC	17.424 °C	79.167 °C	+354.354 %

Table 4.5: Root mean square errors $RMSE$ of the engine model with ATS: initial configuration (first column), modified configuration (second column) and $RMSE$ relative variation (third column).

	Initial configuration	**Thermal model change**	**ΔRMSE**
p_ExbTC_Abs	72.539 mbar	149.697 mbar	+106.368 %
T_EM_avg	50.337 °C	22.735 °C	-54.835 %
p_ExaTC_Abs	12.226 mbar	35.082 mbar	+186.949 %
T_ExaTC	71.272 °C	16.434 °C	-76.942 %

Table 4.6: Root mean square errors $RMSE$ of the engine model without ATS: initial configuration (first column), modified configuration (second column) and $RMSE$ relative variation (third column).

Now that the differences between the two engine models have been carefully analyzed and their impact has been evaluated, it is possible to state that the most relevant dissimilarity is the thermal model inside the exhaust pipes. The thermal model based on the map of the heat exchange coefficients surely optimizes the exhaust side temperatures, which are very important quantities for a correct functioning of the After Treatment System. However, it has been shown that they do not have a physical consistency, in contrast to the thermal model based on a single numerical value. The use of this map-based strategy to model the thermal exchange in the exhaust side of the engine has the main objective of developing the ATS. Instead, the main goal of this thesis is to give a physical consistency to the engine model, improving at the same time the experimental prediction of the engine quantities, in particular the exhaust gas temperatures. Therefore, from now on, the engine model with ATS will be forsaken, focusing exclusively on the other layout and improving it.

Chapter 5

Study of some GT-ISE parameters and their influence on the engine model without ATS

From now on, the reference engine model is the one without ATS, equipped with EGR and VGT closed-loop controllers. The aim of this chapter is to study some GT-ISE parameters, understanding what are they for and which effect they have on the results of the considered engine model. In particular, the aim is to improve the pressures and temperatures trend with respect to the experimental values, and it is important to know if some of these parameter can help to achieve this goal. Before starting this analysis, it is necessary to make some preliminary changes. The latter regard the two closed-loop controllers and the hole diameter of orifice "20", i.e. the orifice at the flap downstream.

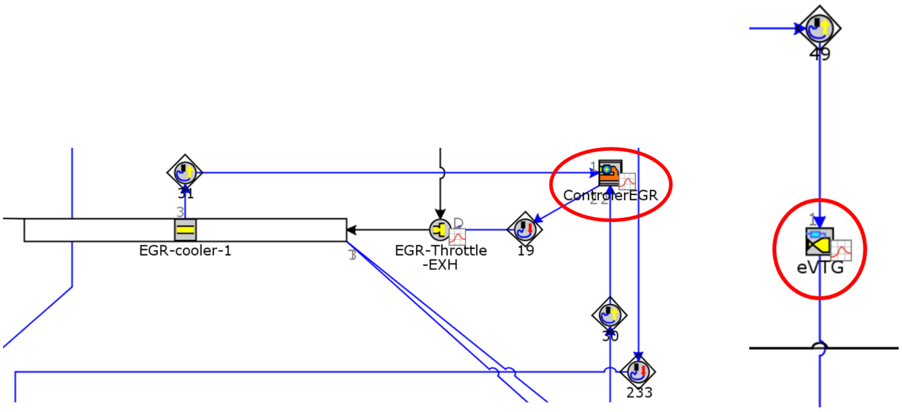

(a) (b)

Figure 5.1: Block of the EGR **(a)** and VGT **(b)** closed-loop control inside which the change is actuated.

Starting with the EGR closed-loop controller, the block within which the change is actuated is reported in Figure 5.1(a). It is the EGR controller block, where the three-dimensional map of the target EGR fraction is replaced by the corresponding experimental values, imposed in the "Case Setup" section. Then also the VGT closed-loop controller is subjected to a modification. The block of the VGT controller that implies the change is highlighted in Figure 5.1(b). The same logic of change of the EGR controller is actuated: the three-dimensional map of the boost pressure is replaced by the corresponding experimental values, always set in "Case Setup". Hence, the VGT target is now based on the experimental values of the boost pressure.
These changes for the EGR and VGT controllers are reported respectively in Figures 5.2 and 5.3. In the first, the 3D map "*RLTEGRMap*" is substituted by the experimental values of the EGR

fraction "*Xr_CO2*", and, with the same logic, in the second one the 3D map "*RLTpBoost*" is replaced by the experimental values of the boost pressure "*Boost*".
The reason of this modification about the target of both controllers can be motivated by the fact of fixing as much as possible the quantities related to them, in order to make the engine model even more faithful with the experimental results and to appreciate better the effect of the studied software parameters.

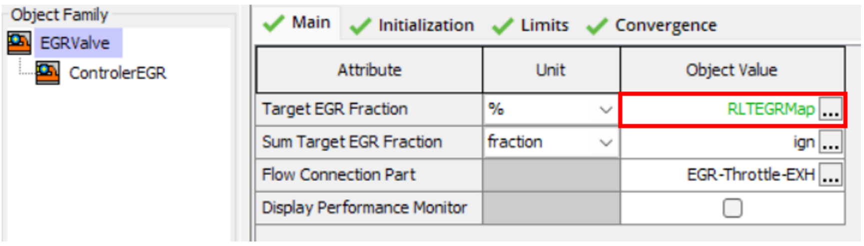

(a)

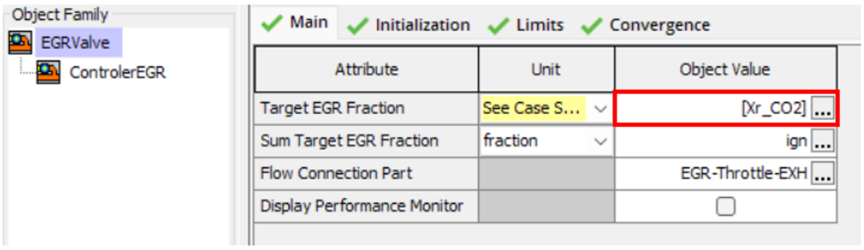

(b)

Figure 5.2: Modification of the EGR closed-loop controller.

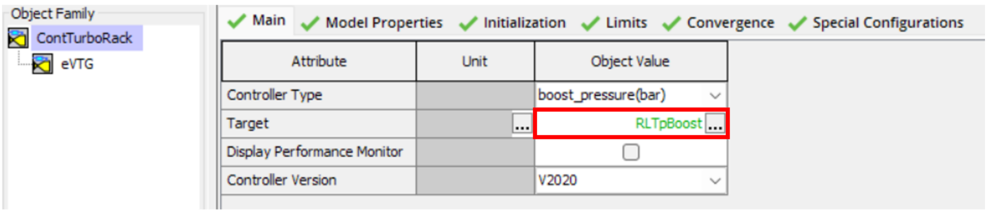

(a)

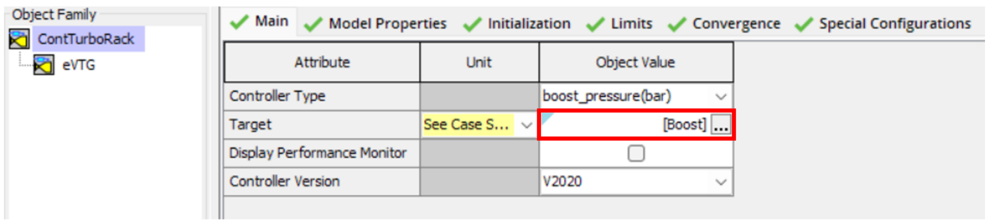

(b)

Figure 5.3: Modification of the VGT closed-loop controller.

The other important change concerns the hole diameter of the orifice "*20*". This orifice is placed downstream of the flap valve. It can be observed that, as hole diameter, there is the variable "*outlet*", imposed in Case Setup section. It is a vector of 126 values, like the number of cases. However, since it indicates a geometrical parameter, it has the same value for all cases. The modification is about this numerical value, which in all the previous simulations was 41 mm. Now it is changed to 40 mm, considering it as the reference value for studying the GT-ISE parameters. One of these software parameters is precisely the hole diameter of this orifice, and it will be possible to discover the effect that it has on the engine simulation results.

Now that the explained modifications have been actuated, the study of the software parameters can start, exploiting this new version of the engine model without ATS. Each parameter will be analyzed separately to detect its influence.

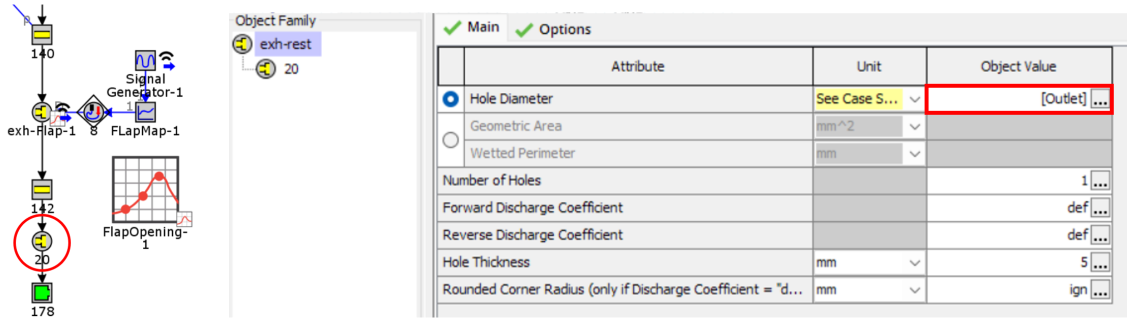

(a) (b)

Figure 5.4: Modification of the hole diameter of the orifice "*20*".

5.1 Heat transfer multiplier

The first parameter that is worth analyzing is the Heat Transfer Multiplier (HTM) of the exhaust manifold. This field belongs to the object that defines the manifold, which is the flow volume with general geometry. In particular, this field belongs to the thermal section of the related object, and it is the factor that amplifies or reduces the amount of heat transfer between the fluid and the wall. The HTM of the exhaust manifold can be observed in Figure 5.5. By default, this parameter is equal to 1. To detect the influence that it has on the engine quantities, it can be enhanced.

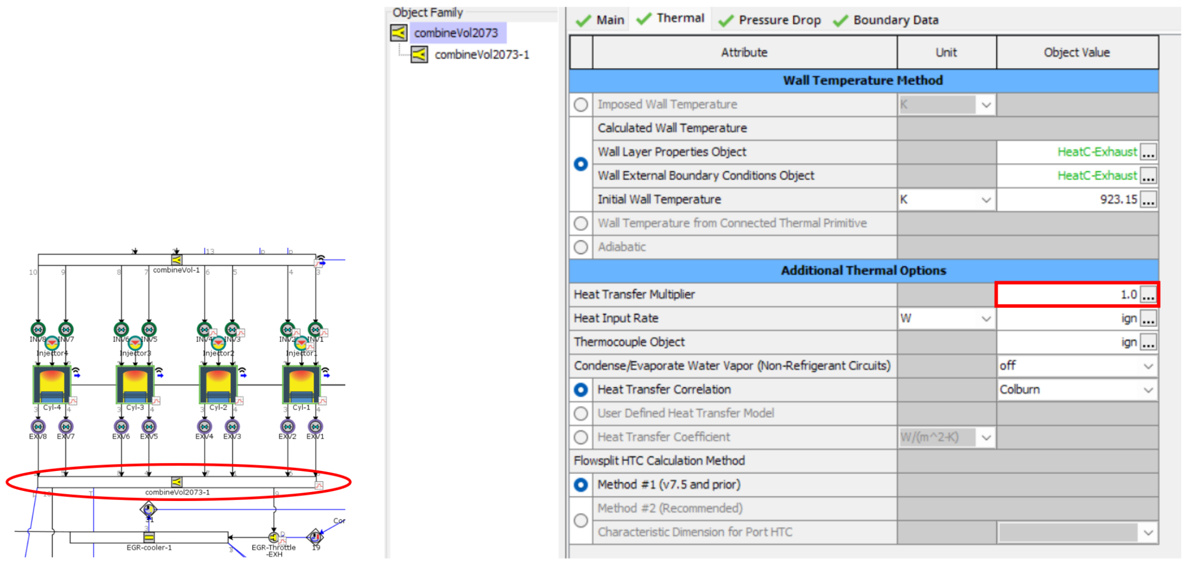

(a) (b)

Figure 5.5: Heat transfer multiplier of the exhaust manifold.

So three simulations were run: the first using a Heat Transfer Multiplier equal to 1, the second a HTM equal to 10 and the last one a HTM equal to 100.
All engine quantities have been examined, but the heat transfer multiplier turns out to be very little influential. Only two quantities are reported: the first is the average temperature of the exhaust manifold and the second is the temperature of the exhaust gases at turbine downstream.

A third quantity is also introduced, i.e. the exhaust manifold wall temperature, which can be very useful since the wall is directly affected by the amount of heat transfer. There is not an experimental exhaust manifold wall temperature, because of the complexity for carrying out the measurement. So, only the simulated trends are shown, which are very important to observe the influence of the heat transfer multiplier.
The average temperature of the exhaust manifold can be found in Figure 5.6 and the temperature of the exhaust gases at the turbine downstream in Figure 5.7. In both diagrams, there are the simulated trends for the three values of the heat transfer multiplier and the experimental trend. It is possible to note that both temperatures are not affected by the variation of the parameter in question. This can be confirmed by the *RMSE* values reported in Table 5.1, subject to very little change.

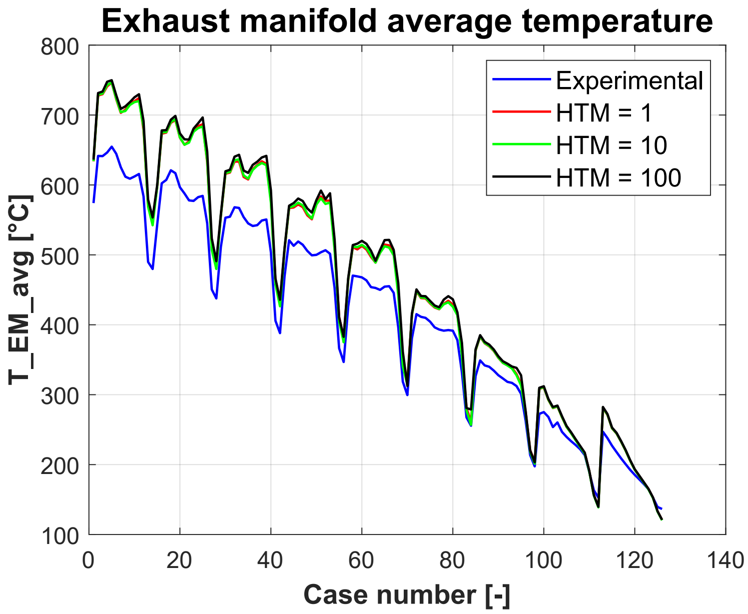

Figure 5.6: Effect of the heat transfer multiplier on the exhaust manifold average temperature.

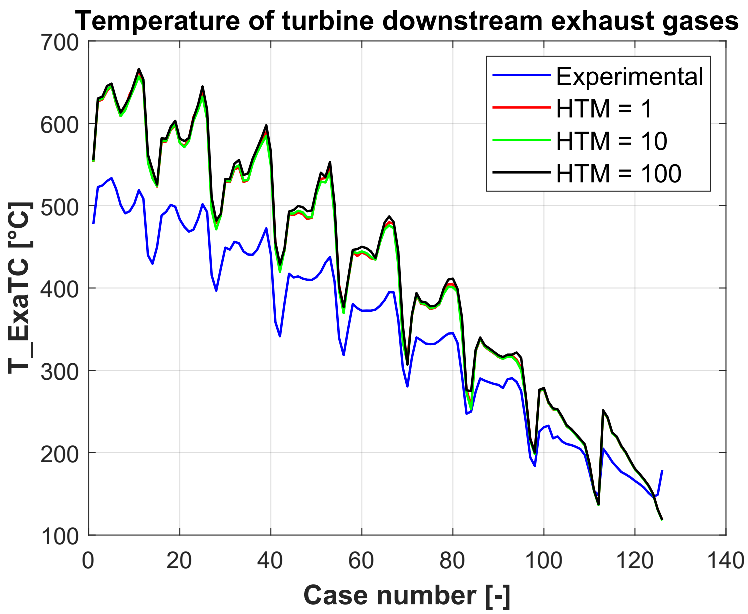

Figure 5.7: Effect of the heat transfer multiplier on the temperature of the turbine downstream exhaust gases.

	HTM = 1	HTM = 10	HTM = 100
T_EM_avg	54.149 °C	53.521 °C	58.915 °C
T_ExaTC	75.593 °C	74.133 °C	79.364 °C

Table 5.1: *RMSE* values of the heat transfer multiplier variation.

The wall temperature of the exhaust manifold, shown in Figure 5.8, is interesting to analyze. It can be seen that increasing the heat transfer multiplier this temperature enhances. This behavior is coherent, because enhancing the studied parameter the amount of heat transfer from the fluid to the wall grows and so the temperature on the wall increases. Furthermore, a detail that can be highlighted is a great gap between $HTM = 1$ and $HTM = 10$ and an almost negligible variation between $HTM = 10$ and $HTM = 100$. There is a saturation effect, so, as the heat transfer multiplier increases, the wall temperature grows less and less.

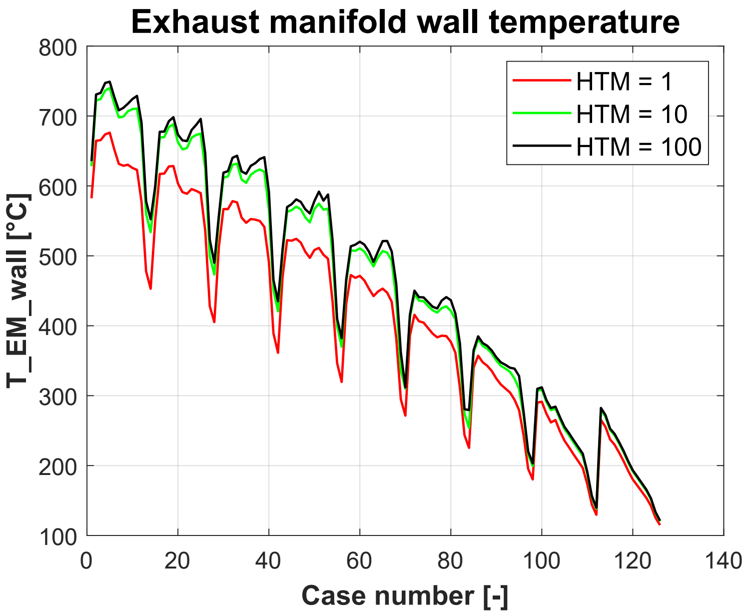

Figure 5.8: Effect of the heat transfer multiplier on the exhaust manifold wall temperature.

5.2 External convection coefficient

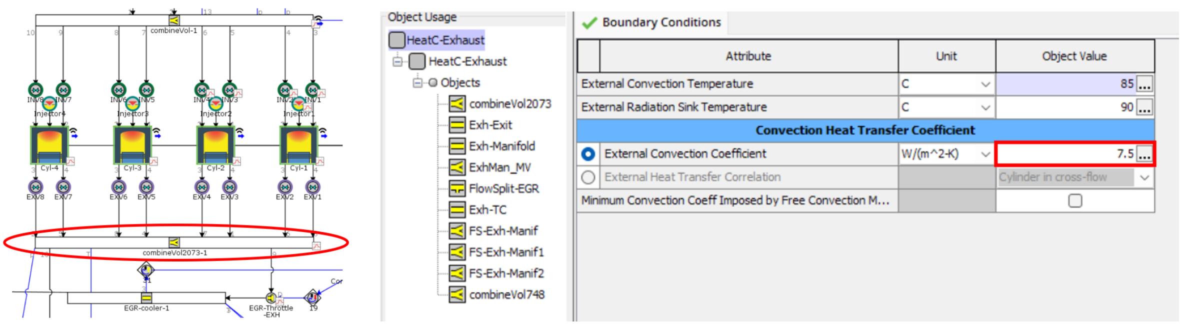

(a) (b)

Figure 5.9: External convection coefficient of the exhaust manifold.

Another parameter that can be studied is the External Convection Coefficient (ECC) of the exhaust manifold. The features of this parameter have already been shown in the previous chapter.

This parameter defines the amount of convective heat flow per surface and temperature unit exchanged with the external environment. It is defined by a single numerical value, as highlighted in Figure 5.9. The imposed value is 7.5 $W/(m^2K)$ and to observe which effect has on the simulated temperatures it can be increased.
The first simulation was run with the initial engine configuration, so with ECC = 7.5 $W/(m^2K)$. Then another simulation was launched, with a greater value of ECC, equal to 20 $W/(m^2K)$. Finally, the ECC was imposed equal to 100 $W/(m^2K)$ in a third simulation. In the last two simulations, the change also regards the temperatures of the wall external boundary conditions object. Both the external convection temperature and the external radiation sink temperature are imposed equal to 60 °C. However, this modification is almost negligible and the magnitude of variation in the results is determined by the ECC, on which the attention is placed.

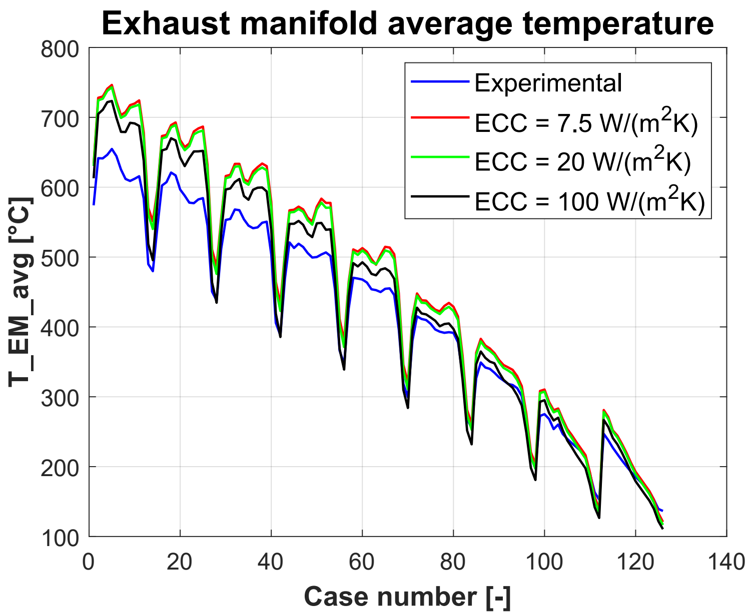

Figure 5.10: Effect of the external convection coefficient on the exhaust manifold average temperature.

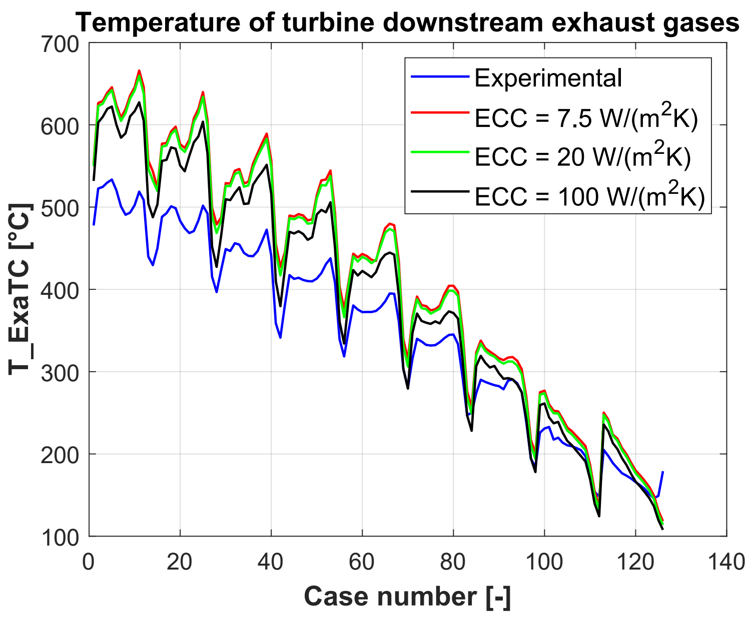

Figure 5.11: Effect of the external convection coefficient on the temperature of the turbine downstream exhaust gases.

	ECC = 7.5 W/(m^{2}K)	ECC = 20 W/(m^{2}K)	ECC = 100 W/(m^{2}K)
T_EM_avg	54.149 °C	50.152 °C	33.580 °C
T_ExaTC	75.593 °C	71.349 °C	52.754 °C

Table 5.2: *RMSE* values of the external convection coefficient variation.

The same quantities of the heat transfer multiplier analysis are reported, because they are directly linked to the ECC and exhibit the most relevant variations. The average temperature of the exhaust manifold is shown in Figure 5.10 and the temperature of the turbine downstream exhaust gases in Figure 5.11. In both quantities, an increase of the external convection coefficient leads to a decrease of the gases temperature, bringing them closer to the experimental results. This is coherent, since a fluid that delivers a greater amount of heat flow to the surroundings consequently is characterized by a diminuishment of its temperature. Furthermore, the decrease is almost proportional to the enhancement of the ECC. It is possible to observe this phenomenon also looking at the Table 5.2, where the RMSE value of each simulated trend is reported. Increasing the value of the external convection coefficient, the RMSE value decreases in an almost proportional manner.
The remaining quantity is again the wall temperature of the exhaust manifold. Looking at Figure 5.12, an opposite effect with respect to the HTM one verifies: increasing the external convection coefficient, the wall temperature decreases. This derives from the different definition of the ECC with respect to the heat transfer multiplier. In fact, while the heat transfer multiplier concerned the amount of heat transfer between the fluid and the wall of the exhaust manifold, the external convection coefficient involves the exchange of heat between the thermodynamic system of the exhaust manifold and the external environment. Therefore, the heat is released by both the fluid and the wall, which define the exhaust manifold system, and for this reason also the temperature wall decreases. Instead, with the rise of the HTM there was the rise of the heat delivered by the exhaust gas to the wall, which consequently was characterized by a higher temperature.
Finally, observing the wall temperature trends, there is always a certain proportionality between the ECC and the decrease of *T_EM_wall*.

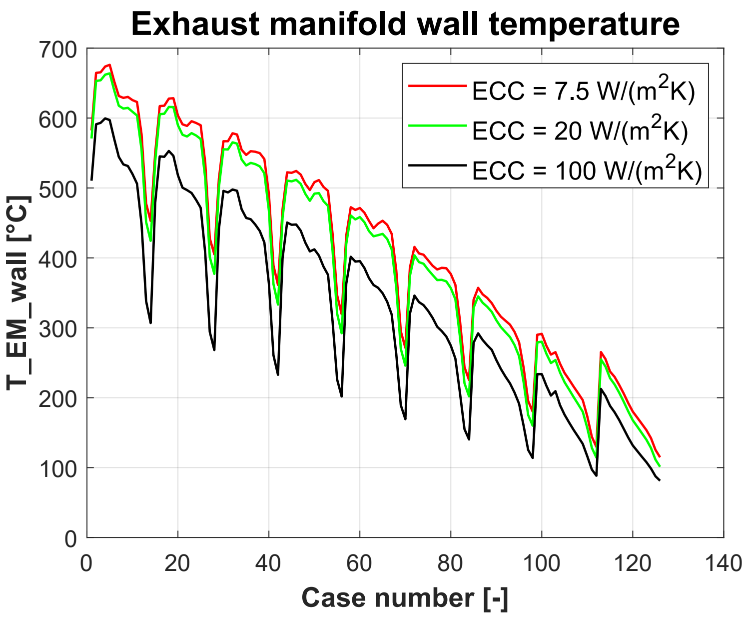

Figure 5.12: Effect of the external convection coefficient on the exhaust manifold wall temperature.

5.3 Turbine multipliers

This section is reserved for the analysis of the turbine multipliers. The effect of these parameters can be complex to understand and it is necessary to conduct a clear study on the influence that they have on the intersted engine quantities. The approach is to fix the thermodynamic conditions of the turbine downstream, and this can be done removing all blocks concerning the flap sub-system, highlighted in Figure 5.13(a). Therefore, the configuration of the turbine downstream side becomes like the one shown in Figure 5.13(b).

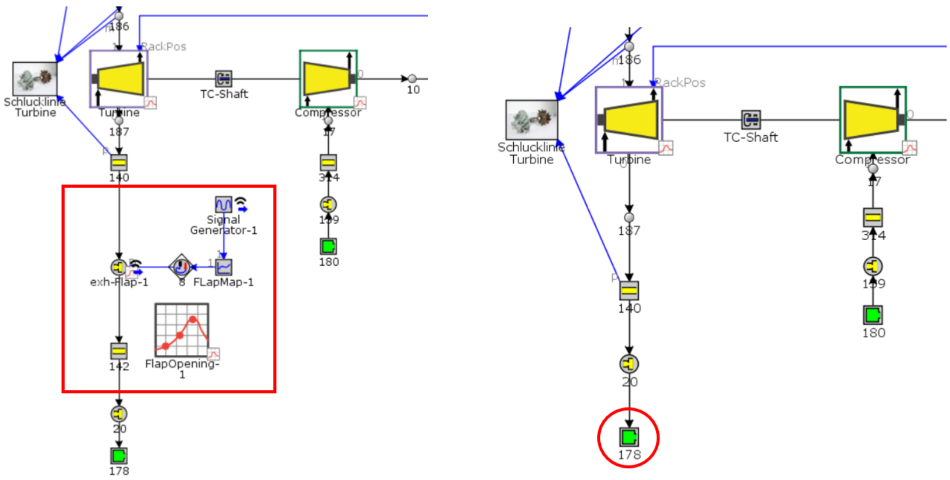

(a) (b)

Figure 5.13: Removal of flap sub-system from the turbine downstream side.

The aim is to impose the experimental thermodynamic conditions of the turbine downstream, considering them as the conditions of the exhaust external environment. This can be performed changing the features of the boundary pressure block "*178*", highlighted in Figure 5.13(b). The absolute pressure inside this block was the experimental pressure of the cabin, so the environment within which the real engine was tested. It is changed replacing this single numerical value by the experimental absolute pressures of the exhaust gases at turbine downstream (p_ExaTC_Abs). To guarantee more and more the imposition of these pressure values, the "inlet-static" condition is selected.

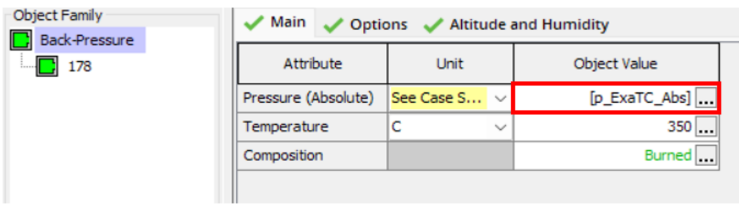

(a)

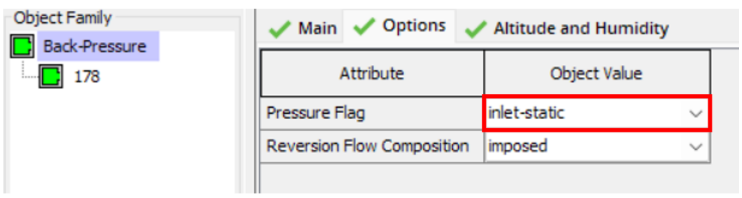

(b)

Figure 5.14: Change of some thermodynamic conditions inside the boundary pressure block "*176*".

The last step before starting with the analysis of the turbine multipliers is to regulate the pressure drops across the blocks staying in between the turbine and the boundary pressure ones, especially across the orifice "*20*". Since the experimental pressure values *p_ExaTC_Abs* must be ensured at the turbine outlet, the pressure drops must be reduced as much as possible. A solution can be to change the hole diameter of the orifice "*20*". There is no longer the Case Setup value "outlet", because was thoughtful for the presence of the flap sub-system. Now that the latter has been removed, there is the need to recalibrate this parameter, with the aim of ensuring the smallest possible pressure drop. The first attempt is the default value, as highlighted in Figure 5.15(b). The diameter value can be enhanced, choosing other five values, that are 53 mm, 54 mm, 56 mm, 58 mm and 60 mm. Six simulations were run, each one with a different hole diameter. In Figure 5.16 the average pressure drop across the orifice "*20*" as a function of the case number is reported, with the trends for all the diameter values.

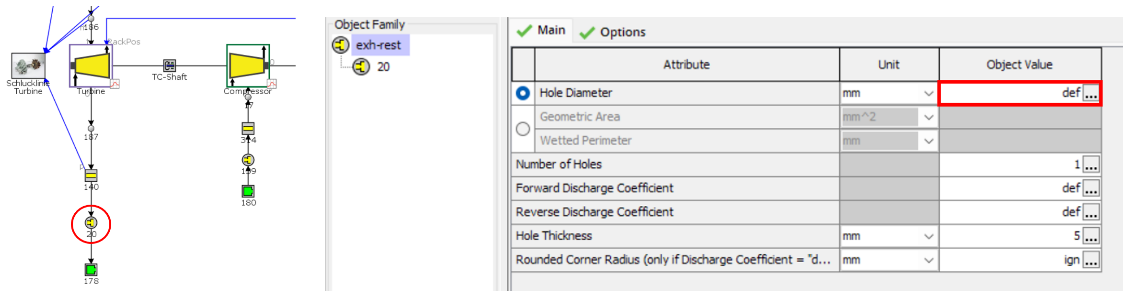

(a) (b)

Figure 5.15: Recalibration of the hole diameter of the orifice "*20*".

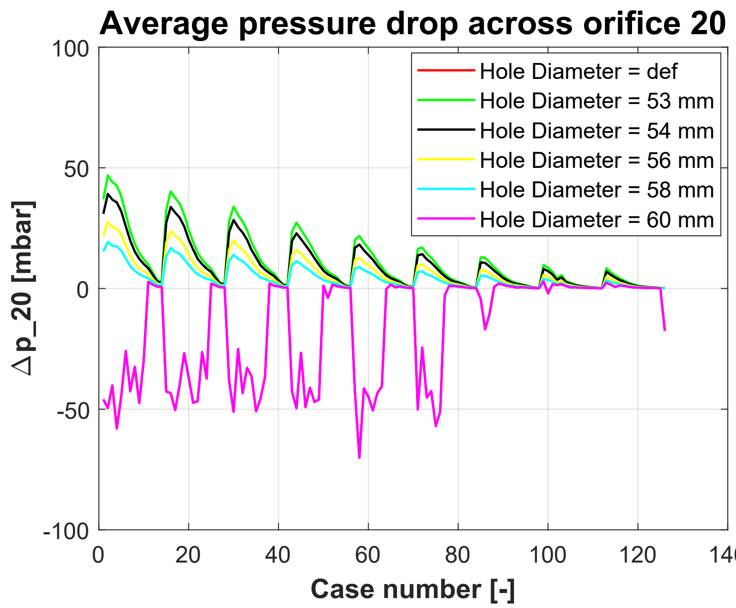

Figure 5.16: Effect of variation of the hole diameter on the average pressure drop across the orifice "*20*"

Observing the diagram, there is a trend that completely differs from the others. It is about the trend for a hole diameter of 60 mm. Actually, the latter overlaps the trend related to the default diameter. So, it can be concluded that the default diameter coincides with a value around 60 mm, since it gives the same outcome. This trend is made up of negative pressure drops. This means that at downstream of the orifice there is a greater pressure than the one at the orifice upstream, phenomenon due to the back-pressure waves. Now that there is no longer the flap valve, these waves can be present in a greater extent, so a value of the orifice diameter must be found to avoid them. The values of diameter different by "def" and 60 mm ensure this. In fact, their pressure drop trends have positive values, as it should be. In particular, the diameter that guarantees the lowest pressure drop across the orifice is 58 mm. Therefore, this value is chosen as the hole diameter value of block "*20*" to perform the analysis of the turbine multipliers.

5.3.1 Turbine efficiency multiplier

The first turbine multiplier investigated is the efficiency one. This parameter belongs to the "Options" section of the turbine block, reported in Figure 5.17, where the multiplier is highlighted. The Turbine Efficiency Multiplier (TEM) is the factor that multiplies the turbine efficiency once derived from the related map, before its imposition. By default, this value is equal to 1 and in all the previous simulations it was used. To understand what type of effect is caused by this parameter, it is necessary to use other values. Six simulations were run, each one exploiting a precise value of this TEM series: 0.9, 1, 1.1, 1.15, 1.2 and 1.25.

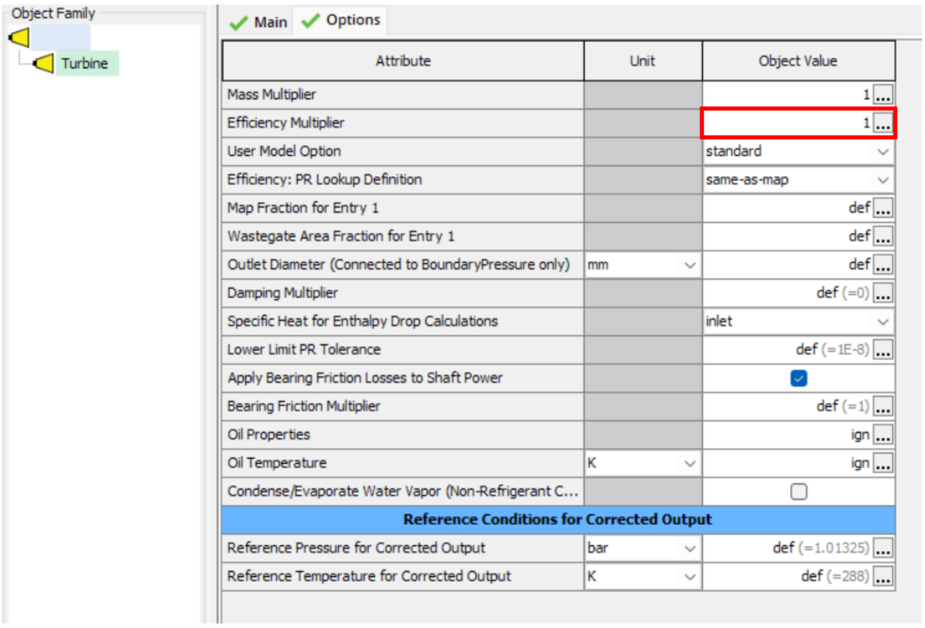

Figure 5.17: "Options" section of the turbine block: Efficiency Multiplier

All the usual engine quantities have been investigated, but only the ones that exhibit the greatest variations are reported. The first quantity is the absolute pressure inside the exhaust manifold (Figure 5.18), which decreases enhancing the turbine efficiency multiplier. In fact, the simulated pressures approach the experimental trend more and more, which is not so distinguishable because it is covered by the last four trends, i.e. the ones of TEM = 1.1, TEM = 1.15, TEM = 1.2 and TEM = 1.25. They are very close to each other and it is useful to rely on the table where the related *RMSE* values are shown (Table 5.3). The root mean square errors of *p_ExbTC_Abs* are reported in the first column, and it can be observed that the best experimental estimate is provided by a TEM = 1.1.
Another quantity that is affected by the TEM change is the *T_EM_avg* (Figure 5.19), which decreases enhancing the parameter in question. The simulated trends get closer and closer to the experimental values, as it is confirmed by the *RMSE* values that decrease, reaching the minimum value for TEM = 1.25.
For what concerns the pressure of the exhaust gases at turbine downstream, it does not depend on the turbine efficiency multiplier, meaning that its variations are negligible changing this parameter. This result is useful to understand that the TEM influences only the pressure at turbine upstream and not the one at turbine downstream. Therefore, for changing the second pressure it is necessary to rely on another parameter, as it will be possible to observe in one of the next sections. Instead,

the increase of this parameter has a little effect on the temperatures at turbine upstream and downstream, which reduce a bit.
The other temperature shows a dependence on the TEM: it is the temperature of the exhaust gases at turbine downstream (Figure 5.20). The same reasoning made about the average temperature of the exhaust manifold is proposed again here. Enhancing the TEM, the simulated *T_ExaTC* decreases and approaches the experimental trend.

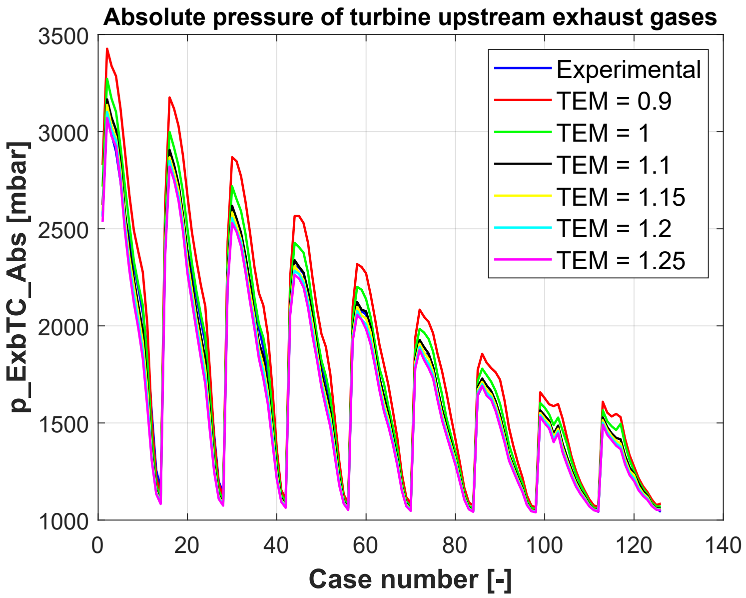

Figure 5.18: Effect of the turbine efficiency multiplier on the absolute pressure of turbine upstream exhaust gases.

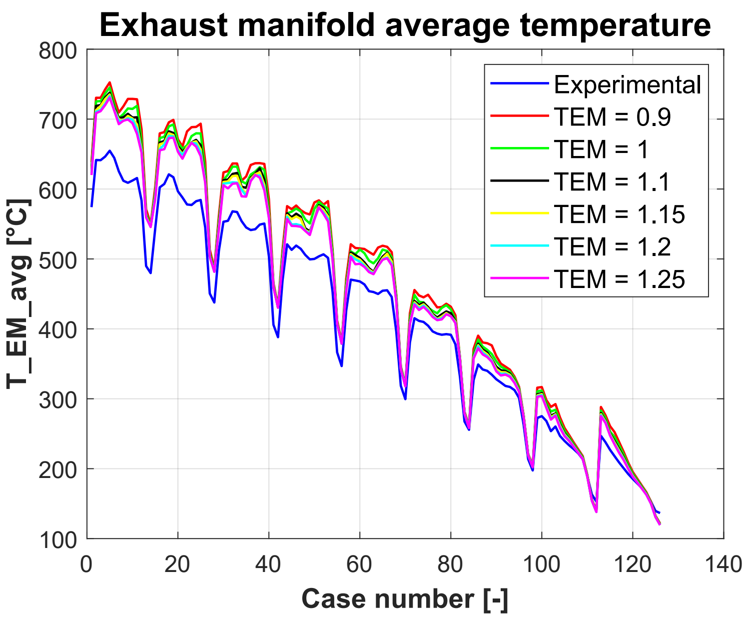

Figure 5.19: Effect of the turbine efficiency multiplier on the exhaust manifold average temperature.

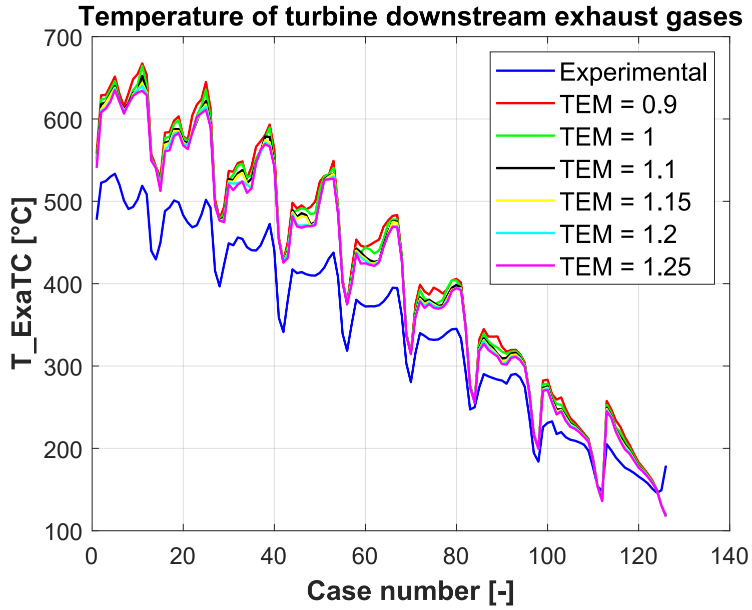

Figure 5.20: Effect of the turbine efficiency multiplier on the temperature of the exhaust gases at turbine downstream.

	p_ExbTC_Abs	***T_EM_avg***	***T_ExaTC***
TEM = 0.9	175.917 mbar	59.222 °C	80.535 °C
TEM = 1	79.923 mbar	52.717 °C	74.951 °C
TEM = 1.1	50.999 mbar	47.518 °C	70.777 °C
TEM = 1.15	59.320 mbar	45.487 °C	69.257 °C
TEM = 1.2	73.233 mbar	43.397 °C	67.653 °C
TEM = 1.25	88.096 mbar	41.773 °C	66.525 °C

Table 5.3: *RMSE* values of the turbine efficiency multiplier variation.

5.3.2 Turbine mass multiplier

The second multiplier that is analyzed is the Turbine Mass Multiplier (TMM). It is highlighted in Figure 5.21 and by default its value is equal to 1. This parameter is the factor that multiplies the mass flow rate once it is derived from the related map, before its imposition. To investigate the effect provided by this multiplier, it is useful to run simulations with other values. Three simulations were run, the first with TMM = 0.9, the second with TMM = 1 and the third with TMM = 1.1.

Only a quantity is influenced by this parameter in relevant way, i.e. the *p_ExbTC_Abs* (Figure 5.22). It can be noticed that for TMM = 0.9 the quantity is overestimated at high and medium loads, while at low loads the simulated trend follows in a better way the experimental one. A different behavior has the trend related to TMM = 1.1: a greater approach to the experimental values at high and medium loads, but a major gap at low loads. Globally, the best trend is provided by TMM = 1. In fact, the *RMSE* values are: 110.172 mbar for TMM = 0.9, 79.923 mbar for TMM = 1 and 91.244 mbar for TMM = 1.1. The first value of TMM gives the worst response, due to the excessive overestimation at high loads. Even with a turbine mass multiplier greater than the default one, there is not an optimal experimental prediction, due to the relevant overestimation at low loads.

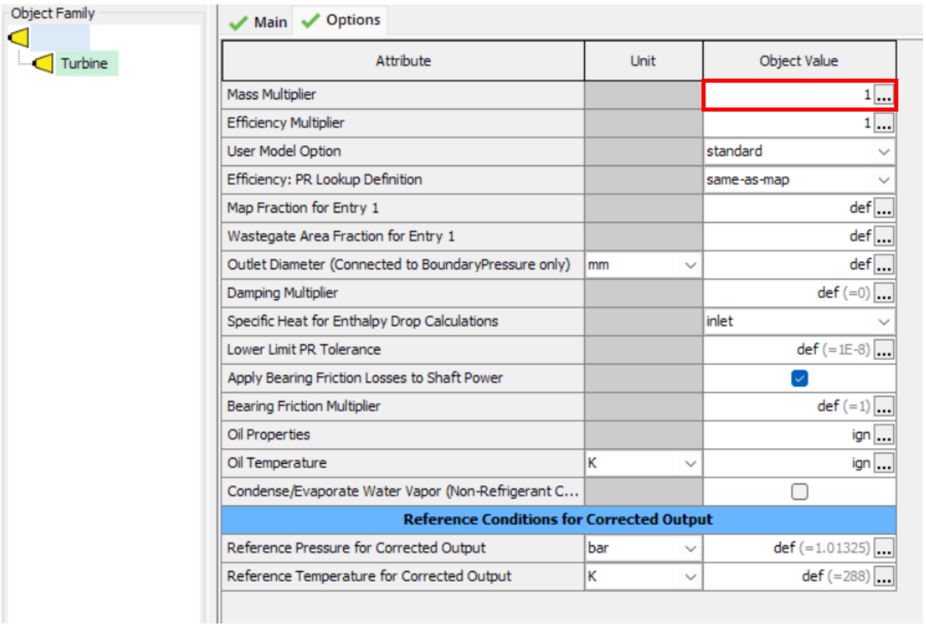

Figure 5.21: "Options" section of the turbine block: Mass Multiplier

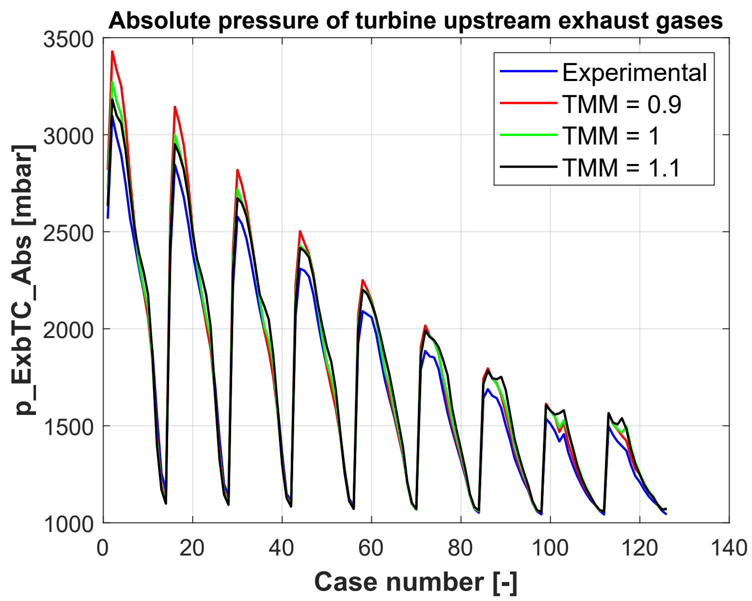

Figure 5.22: Effect of the turbine mass multiplier on the absolute pressure of turbine upstream exhaust gases.

5.4 Hole diameter of orifice "*20*"

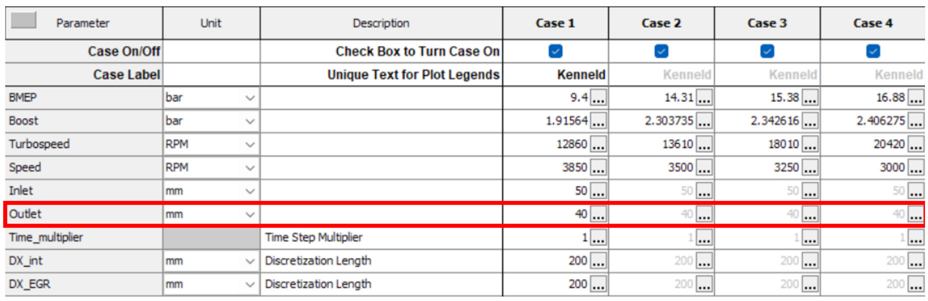

Parameter	Unit	Description	Case 1	Case 2	Case 3	Case 4
Case On/Off		Check Box to Turn Case On	☑	☑	☑	☑
Case Label		Unique Text for Plot Legends	Kenneld	Kenneld	Kenneld	Kenneld
BMEP	bar		9.4	14.31	15.38	16.88
Boost	bar		1.91564	2.303735	2.342616	2.406275
Turbospeed	RPM		12860	13610	18010	20420
Speed	RPM		3850	3500	3250	3000
Inlet	mm		50	50	50	50
Outlet	mm		40	40	40	40
Time_multiplier		Time Step Multiplier	1	1	1	1
DX_int	mm	Discretization Length	200	200	200	200
DX_EGR	mm	Discretization Length	200	200	200	200

Figure 5.23: Case Setup section: "*Outlet*" variable.

Another important parameter that can be studied is the hole diameter of orifice "*20*". To perform the analysis, it is necessary to restore the flap sub-system. Once all flap blocks have been reintegrated in the turbine downstream side, the hole diameter of the orifice can be varied. New values can be directly inserted in the "*Outlet*" variable in the Case Setup section, as it can be observed in Figure 5.23. This variable is imposed as hole diameter of the orifice 20, like it was illustrated in Figure 5.4.
The value of the "*Outlet*" variable can be increased, and simulations with 40 mm, 41 mm, 42 mm, 43 mm, 44 mm and 45 mm were run.

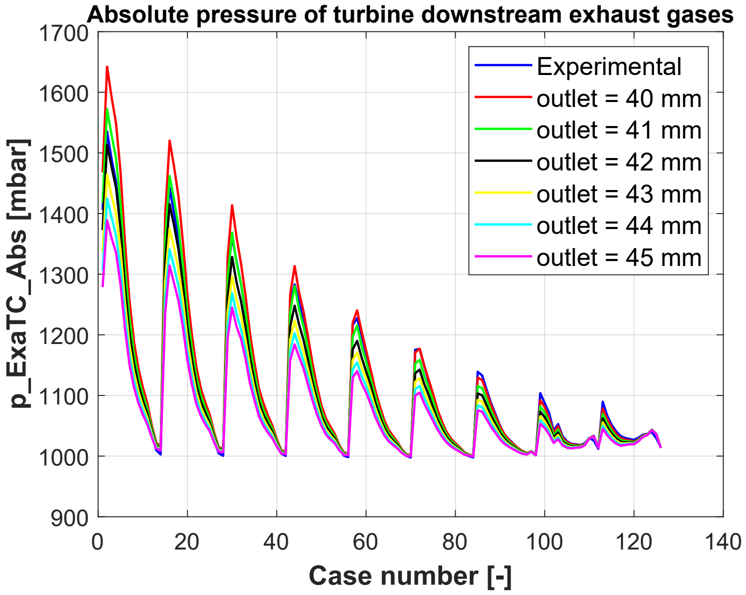

Figure 5.24: Effect of hole diameter of orifice "*20*" on the absolute pressure of turbine downstream exhaust gases.

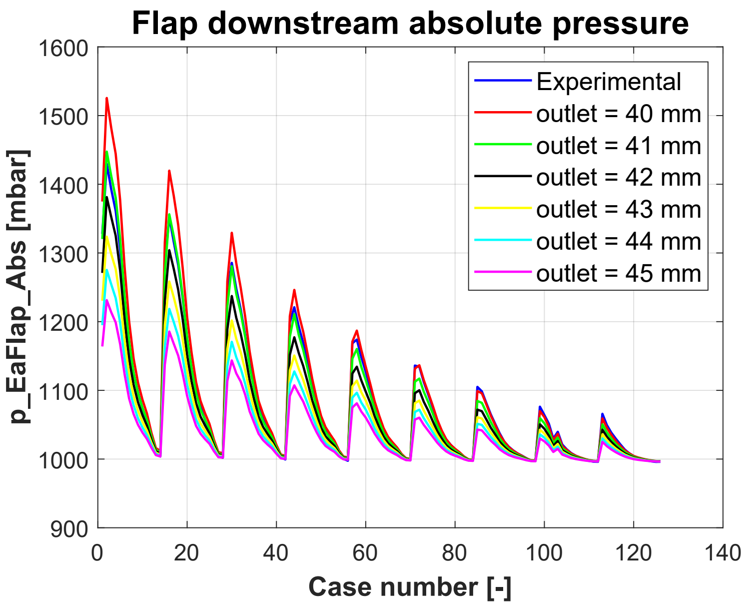

Figure 5.25: Effect of hole diameter of orifice "*20*" on the absolute pressure of flap downstream.

Analyzing the results, the most relevant dependence on this parameter is about the absolute pressure at turbine downstream (Figure 5.24) and about the absolute pressure at flap downstream (Figure 5.25). The latter quantity has never been shown so far, and it is very useful in this section to examine what happens at flap downstream side, since it is the location of the orifice 20.
The increase of this diameter leads to a decrease of both pressures. In fact, having an orifice

of greater sizes helps to diminuish the pressure at its upstream. In particular, the pressures at turbine downstream depend on this parameter. Even the pressure at turbine upstream decreases with the growth of the orifice 20 diameter, but in less extent than the other pressures. So for this reason only the pressures at turbine downstream are reported.
Observing the *RMSE* values in Table 5.4, it can be noticed that the best experimental estimate is ensured by a hole diameter of 41 mm. The value of 40 mm provides an excessive overestimation at high loads, while all other values greater than 41 mm cause an extreme underestimation of the pressures.
The hole diameter of orifice "*20*", even if in less extent, influences also the pressure at turbine upstream and the temperatures at turbine upstream and downstream. In fact, enhancing the diameter, a little reduction of these quantities occurs, and this represents a further advantage that can be exploited in the final optimization of the engine model, shown in the next chapter.

	p_ExaTC_Abs	***p_EaFlap_Abs***
outlet = 40 mm	26.270 mbar	22.395 mbar
outlet = 41 mm	11.147 mbar	8.310 mbar
outlet = 42 mm	17.172 mbar	21.509 mbar
outlet = 43 mm	30.044 mbar	36.973 mbar
outlet = 44 mm	41.983 mbar	50.771 mbar
outlet = 45 mm	52.401 mbar	62.890 mbar

Table 5.4: *RMSE* values of the variation of orifice "*20*" hole diameter.

5.5 Coolant and oil boundary conditions of the cylinder object

This last section concerns the thermal properties of the cylinder object and will represent the most decisive solution to improve the estimate of the temperatures. The study focuses on the Wall Temperature object, highlighted in Figure 5.27, with the name "*Wallheat*".

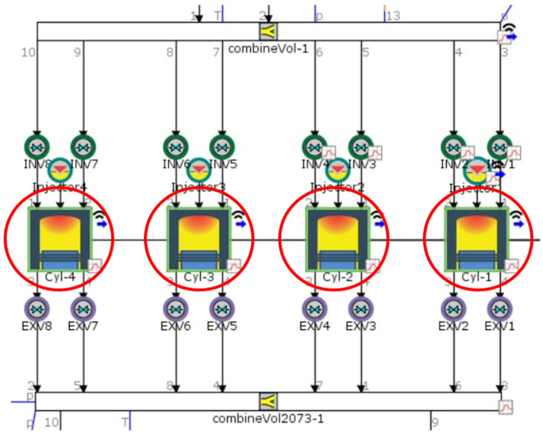

Figure 5.26: Thermal modification within the blocks of the cylinders.

The wall temperature object is shown in Figure 5.28 and is made up of three sections. The third one is exhibited, with the name "Cooling Boundary Conditions". As the name suggests, this section defines the thermodynamic boundary conditions of the cylinder cooling. There are several fields that define the properties of the two fluids used to cool the cylinders: the coolant and the oil. For the coolant, the temperature and the heat transfer coefficient of the cylinder side can be chosen. Then the same quantities can be defined for the head side. About the oil, in the same way, the temperature and the heat transfer coefficient of the cylinder side can be inserted. Furthermore, there are the same two quantities but for the piston side. It is possible to notice that for the heat transfer coefficients of both fluids there are single numerical values, while all the temperatures are defined by maps. The latter are three-dimensional maps, where the values of temperatures in °C are as a function of the engine speed and BMEP, exactly like all the 3D maps seen so far.

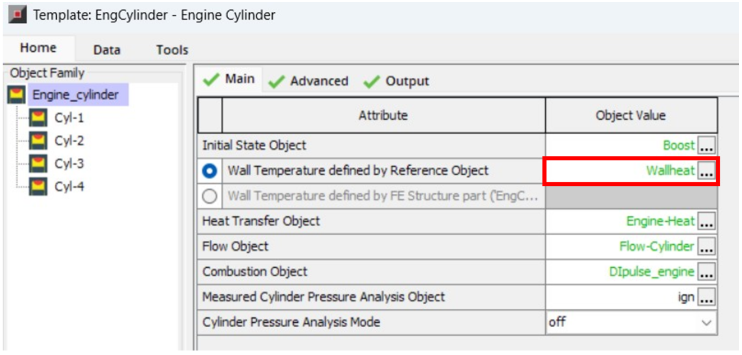

Figure 5.27: Engine cylinder object.

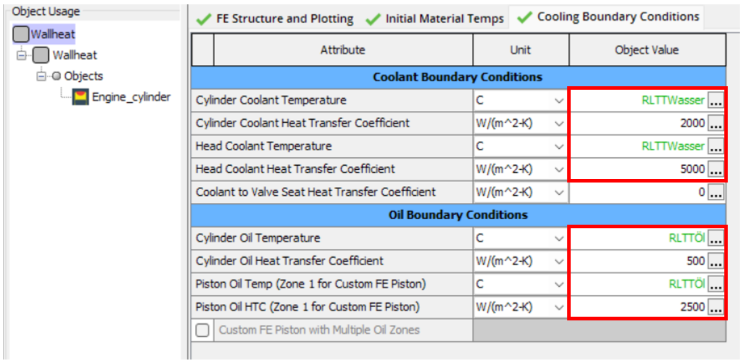

Figure 5.28: Wall Temperature object of the engine cylinders.

To examine the influence of the thermal properties of these two fluids, it is useful to modify them using the following logic, creating these new engine configurations:

- "Coolant HTC": first engine configuration with a new value of heat transfer coefficient of the coolant;
- "Coolant HTC&T": second engine configuration with a new value of heat transfer coefficient and temperature of the coolant;
- "Coolant HTC&T" - Oil HTC": third engine configuration with a new value of heat transfer coefficient and temperature of the coolant and with a new value of heat transfer coefficient of the oil;
- "Coolant HTC&T - Oil HTC&T": fourth engine configuration with a new value of heat transfer coefficient and temperature of the coolant and with a new value of heat transfer coefficient and temperature of the oil.

It can be noted that every successive new engine configuration includes all the previous ones. This logic helps to study in a sequential way the effect of each thermal property.
The heat transmission between the cylinders and the two cooling fluids is mainly of convective type. In particular, it is a forced convection, since both fluids are governed by pumping systems in a real engine. Therefore, the new value of the heat transfer coefficient, for both coolant and oil, is set as the upper estreme of the experimental range of coefficients for water and liquids in forced convection: 10000 $W/(m^2K)$. In fact, the experimental range of these coefficients is 50 $\div$ 10000 $W/(m^2K)$. A good solution is to take the maximum of this range with the aim to enhance

the heat exchange, for reducing the simulated temperatures, but at the same time to comply with the physical limits of the phenomenon in question.
Regarding the temperatures of the two fluids, the three-dimensional maps are replaced by experimental values, test by test. About the new temperature of the coolant, the arithmetic average of the fluid experimental temperature at the cooling system inlet and of the one at the cooling system outlet is exploited. Instead, for the oil temperature it is used the experimental temperature of the oil in the engine gallery. These two temperatures, functions of the steady-state test number, are reported in Figure 5.29. Some considerations can be carried out about the two trends. The average coolant temperature exhibits a trend that increases globally. This enhancement is mainly due to the decrease of the load. An internal combustion engine at low loads has a lower efficiency, so a greater heat dissipation occurs, absorbed by the coolant. So, this explains the general increase of the coolant temperature proceeding with the steady-state tests. Furthermore, it is possible to see shortly before the test 100 a singularity, where there is a large decrease of the coolant temperature. This is probably due to a longer time interval from the previous test, which caused a engine cooling down. A similar phenomenon occurs, even if in less extent, to the temperature of the oil (Figure 5.29(b)), always looking shortly before the test 100. About the latter temperature, it has a different behavior with respect to the coolant one. In fact, going ahead with the tests it shows a global diminuishment and furthermore it has a more orderly trend. This trend follows the engine speed one: at high engine speeds there are high oil temperatures, while at lower engine speeds the oil temperature decreases. The oil is responsible for the lubrication and the cooling of the engine moving parts, for instance the bearings, the pistons etc. At high engine speeds, the moving parts are subjected to more friction, with a consequent greater dissipation of heat, absorbed by the oil. Instead, the global decrease of the oil temperature trend can be explained with the load decrease. The moving parts are less stressed when there is a minor amount of load, producing less friction and so dissipating less heat.

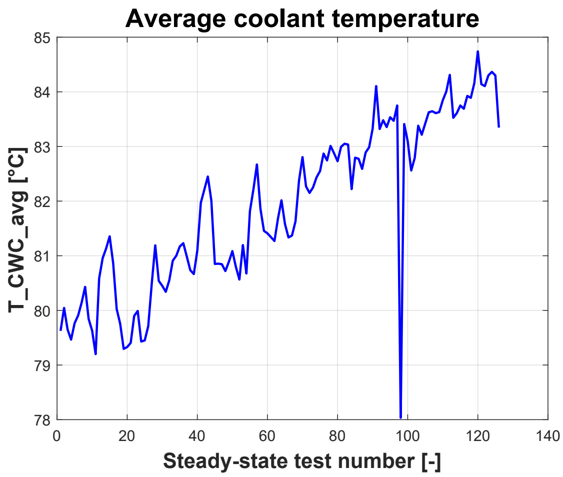

(a)

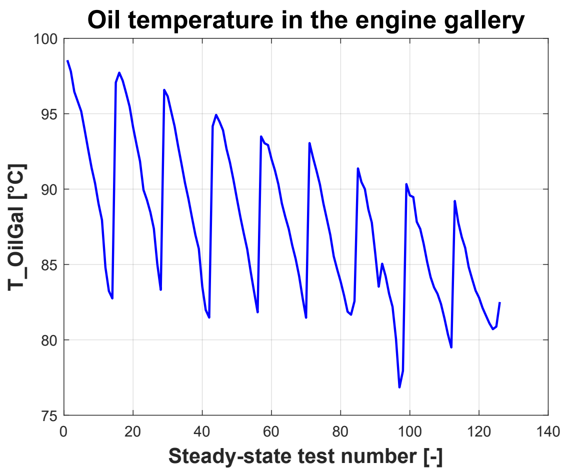

(b)

Figure 5.29: Average coolant temperature **(a)** and oil temperature in the engine gallery **(b)**.

It is possible to perform a simulation with each of the new engine configurations, with the aim of detecting the effect of the thermal modifications described above. The first simulation regards the initial configuration, so without thermal modifications within the engine cylinder object, i.e. with the properties shown in Figure 5.28. The second simulation concerns the "Coolant HTC" configuration, where the heat trensfer coefficients of the coolant are set equal to 10000 $W/(m^2K)$ and the other properties are the same as the initial configuration. Then the next simulation regards the "Coolant HTC&T" engine layout, imposing the coolant temperatures equal to T_CWC_avg and with the same settings as the previous configuration. The fourth simulation is of the "Coolant HTC&T - Oil HTC" layout, where the heat transfer coefficients of the oil are set equal to 10000 $W/(m^2K)$ and the other properties are the same as the previous "Coolant HTC&T" engine

configuration. Finally, the last simulation is about the "Coolant HTC&T - Oil HTC&T" model, setting the temperatures of the oil equal to *T_OilGal* and including all the properties of the previous configuration.
The changes about the boundary conditions of the coolant and oil mainly impact on the temperatures of the engine model. The other quantities are also influenced, but in less extent and furthermore their behavior with respect to the experimental results is not compromised. Therefore, only the temperatures are examined. The first is the exhaust manifold average temperature (Figure 5.30), where the thermal modifications regarding the cylinders have a reducing effect. In fact, introducing more and more the changes about the heat transfer coefficients and temperatures of the coolant and oil, the simulated temperature decreases, approaching the experimental results. The best trend is given by the engine configuration that includes all the thermal modifications, i.e. the "Coolant HTC&T - Oil HTC&T".

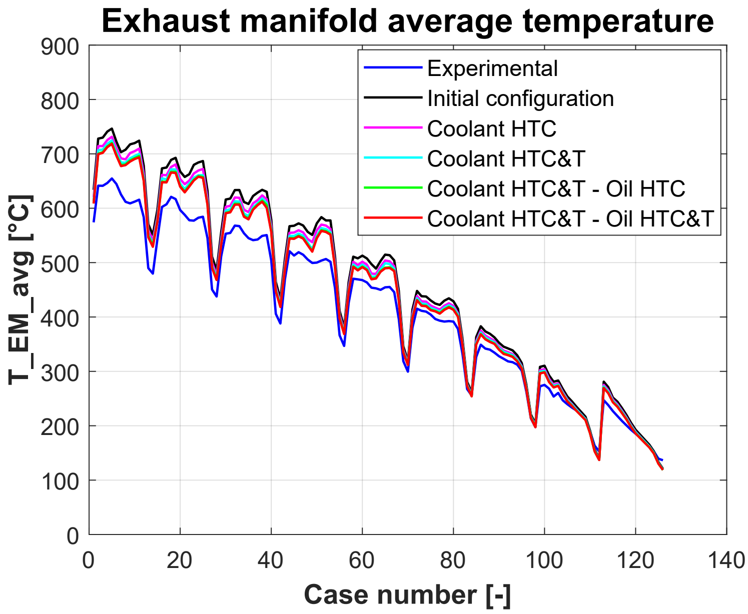

Figure 5.30: Effect of coolant and oil boundary conditions on the exhaust manifold average temperature.

The same behavior observed about the *T_EM_avg* is present also in the other two temperatures, which are the temperature of the exhaust gases at turbine downstream (Figure 5.31) and the temperature at flap downstream (5.32). The latter is a new quantity, never shown so far, but very useful to observe the effect of the analyzed parameters. The behavior of the temperatures is confirmed by the related *RMSE* values, reported in Table 5.5. Looking at the root mean square error values in sequential order, it is possible to note that the reducing effect is smaller and smaller. In fact, introducing the new heat transfer coefficients of the coolant, the *RMSE* values decrease by almost 10 °C. Then, inserting the new coolant temperatures, the reduction is by about 5°C, and finally introducing the new heat transfer coefficients of the oil and the new oil temperatures the reductions are respectively of roughly 3°C and 1°C. Therefore, there is a sort of saturation effect. However, these modifications will be exploited in the next chapter to improve the engine temperatures.

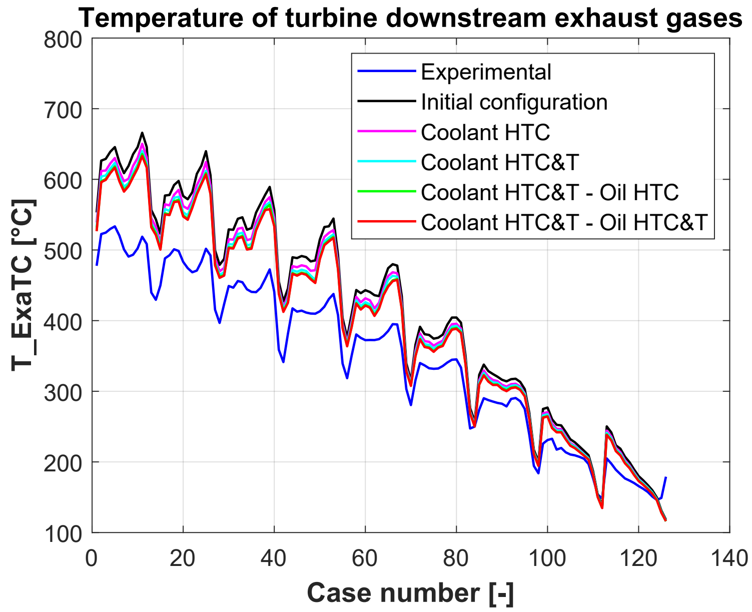

Figure 5.31: Effect of coolant and oil boundary conditions on the temperature of the exhaust gases at turbine downstream.

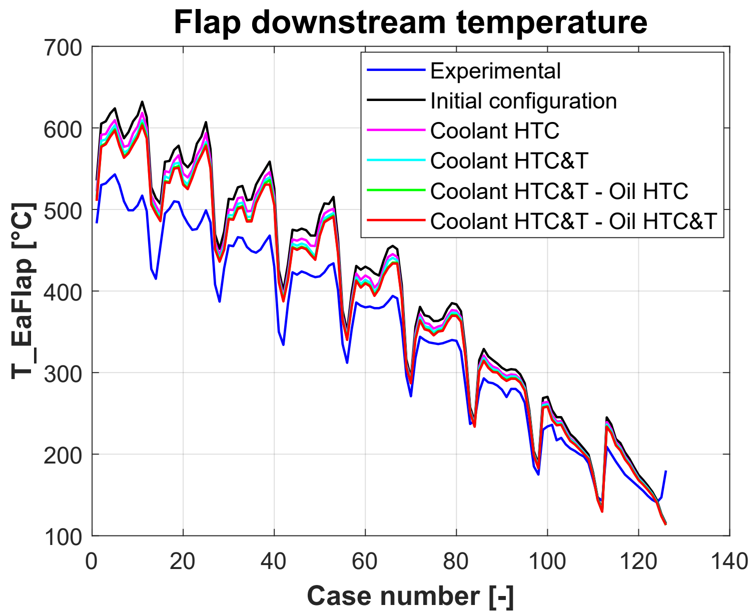

Figure 5.32: Effect of coolant and oil boundary conditions on the flap downstream temperature.

	T_EM_avg	*T_ExaTC*	*T_EaFlap*
Initial configuration	54.149 °C	75.593 °C	56.710 °C
Coolant HTC	44.395 °C	65.502 °C	47.700 °C
Coolant HTC&T	39.402 °C	60.333 °C	43.109 °C
Coolant HTC&T - Oil HTC	36.597 °C	57.396 °C	40.548 °C
Coolant HTC&T - Oil HTC&T	35.439 °C	56.163 °C	39.442 °C

Table 5.5: *RMSE* values of the variation of coolant and oil boundary conditions.

Chapter 6

Optimization of the engine model without ATS and final simulation

6.1 Optimization of the engine model without ATS

Having understood which are the effects of the GT-ISE parameters studied in the previous chapter, they can be exploited to perform an optimization of the engine model without ATS. This operation is performed on the engine configuration equipped with EGR and VGT closed-loop controllers, i.e. the same configuration on which the previous study was conducted. Actually, the goal is to reintegrate the two open-loop controllers into this optimized configuration, for then performing a final simulation and comparing the results with the ones of the original engine configuration without ATS. However, to perform this reintegration, a further step is needed, as it will be possible to see.

The optimization is based on these GT-ISE parameters:

- the boundary conditions of the coolant and oil of the cylinder object;
- the hole diameter of the orifice ”*20*”;
- the External Convection Coefficient (ECC) of the thermal model inside the exhaust pipes;
- the Turbine Efficiency Multiplier (TEM).

The aim is to exploit the advantages brought by these parameters, knowing the quantities on which they have relevant effects.

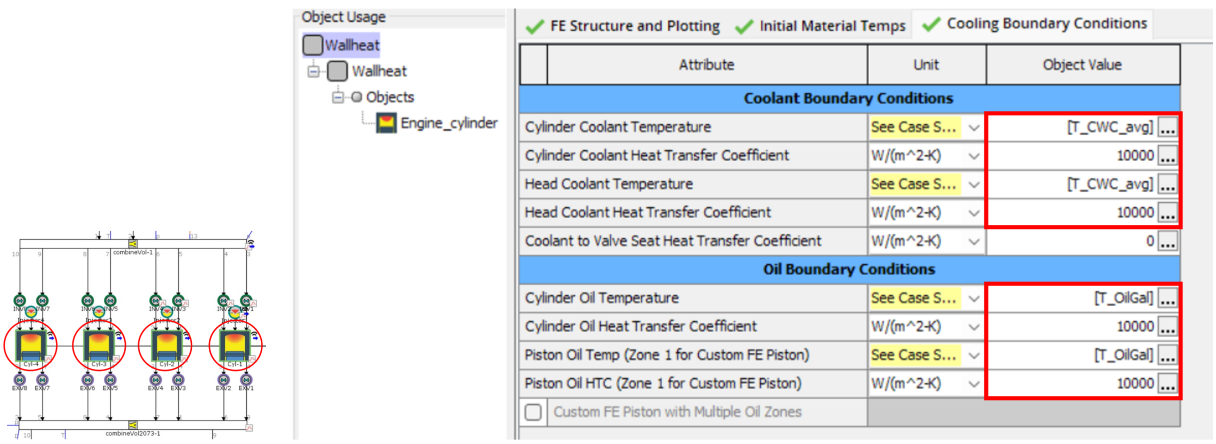

(a) (b)

Figure 6.1: ”Coolant HTC&T - Oil HTC&T” configuration for the final optimization.

Starting from the boundary conditions of coolant and oil inside the engine cylinder object, the reducing effect provided by them on the temperatures was shown in the previous chapter. It was stated that the configuration that guarantees the best estimate of the experimental temperatures is the "Coolant HTC&T - Oil HTC&T" configuration, in which the heat transfer coefficients are equal to 10000 $W/(m^2K)$ and the temperatures are *T_CWC_avg* for the coolant and *T_OilGal* for the oil. So these modifications are introduced in the new optimized engine configuration, as reported in Figure 6.1.
The second parameter exploited for the optimization is the hole diameter of orifice "*20*". The goal of its utilization is to align the pressures at turbine downstream with the experimental trends. In fact, in the previous chapter it was observed that the enhancement of this parameter leads to a reduction of *p_ExaTC_Abs* and *p_EaFlap_Abs*. It was seen that the value that guarantees the best experimental prediction is 41 mm, and this value is chosen for the final engine model. The choice of this parameter is reported in Figure 6.2. This parameter brings also a slight decrease of *p_ExbTC_Abs* and of the temperatures at turbine upstream and downstream, feature that is advantageous for the improvement of their experimental estimate.

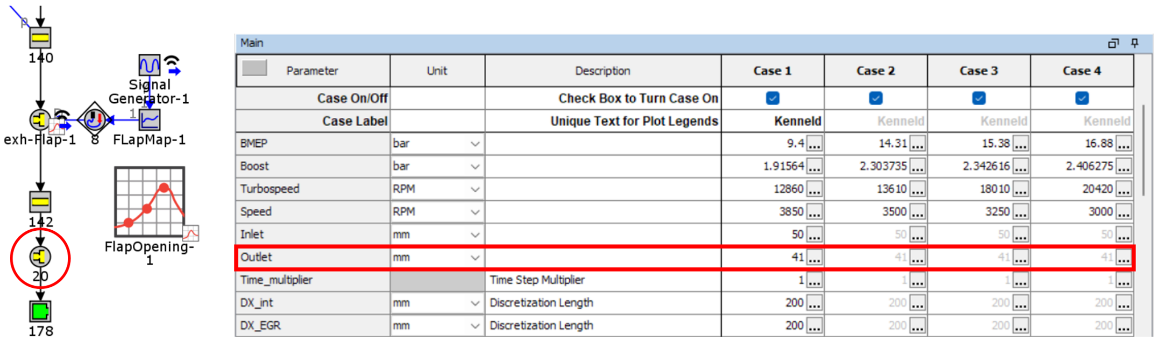

(a) (b)

Figure 6.2: Change of the orifice "*20*" diameter for the final optimization.

Continuing the optimization with the external convection coefficient, it is enhanced in all the exhaust pipes to further reduce the temperatures at turbine upstream and downstream. The new value chosen is 25 $W/(m^2K)$, which is the upper extreme of the typical range of the thermal exchange coefficient of the air in natural convection ($5 \div 25$ $W/(m^2K)$). In fact, the fluid surrounding the exhaust pipes is the air and the heat transfer way between the two thermodynamic system is the free convection. The reason of the selected heat transfer coefficient is to increase the amount of thermal flux towards the surroundings but at the same time to comply with the physical limits of the air in free convection. The modification of the ECC is reported in Figure 6.3 and applies to all highlighted exhaust pipes.

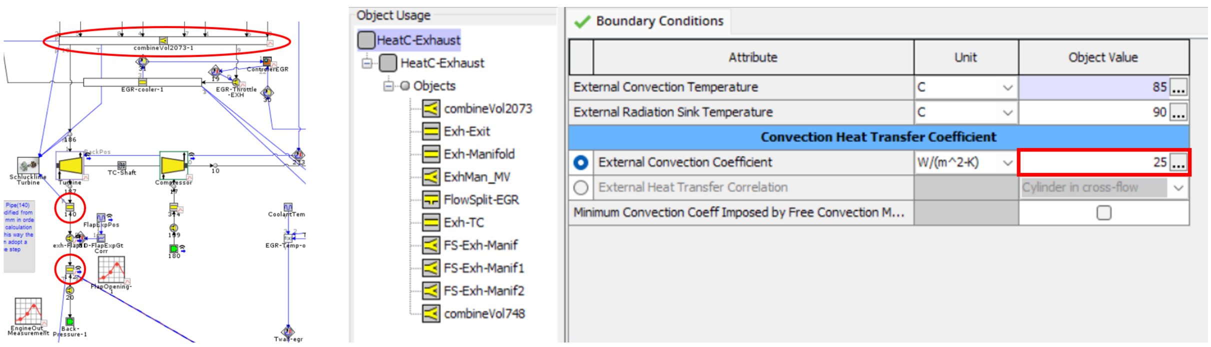

(a) (b)

Figure 6.3: Change of the external convection coefficient in the exhaust pipes for the final optimization.

The last parameter that is modified to perform the optimization is the turbine efficiency multiplier. It is enhanced only to 1.05, so as not to deviate too much from the realistic values of turbine efficiency but at the same time exploiting a little the advantages brought by this parameter increase, i.e. the reduction of the absolute pressure at turbine upstream and of all the temperatures. It is possible to observe the presence of this new value in Figure 6.4(b).
Now that all the parameters have been updated to obtain the optimized engine model, it is necessary to reintegrate into the configuration the EGR and VGT open-loop controllers.

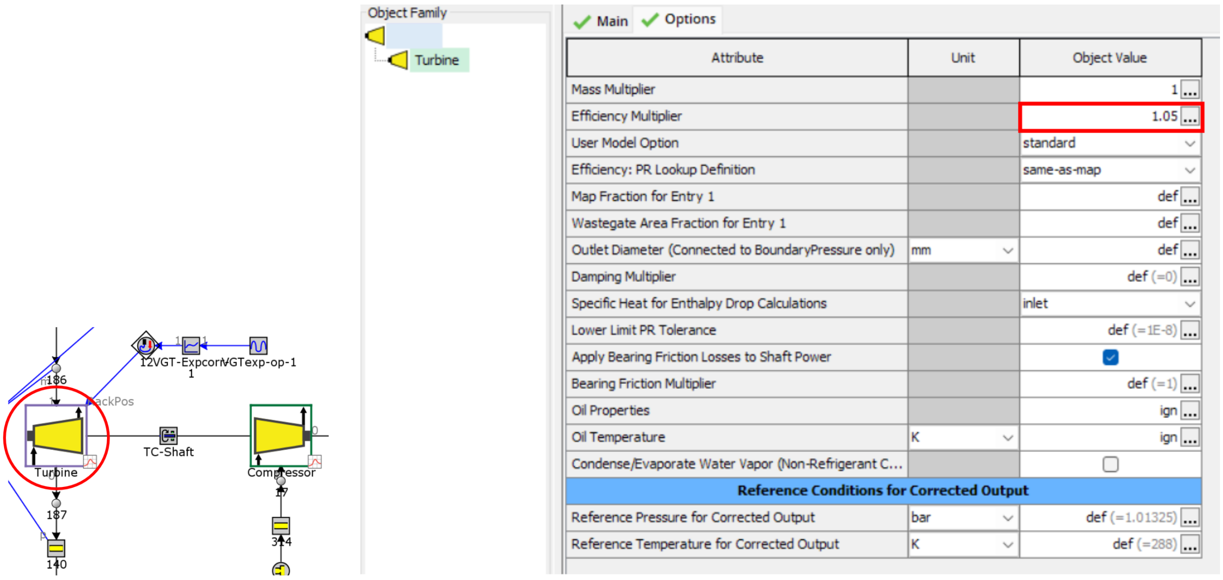

(a) (b)

Figure 6.4: Change of the turbine efficiency multiplier for the final optimization.

6.2 Reintegration of the open-loop controllers into the engine model without ATS

This section is reserved for the reintroduction of the EGR and VGT open-loop controllers into the engine model without ATS. The aim is to compare this new optimized configuration with the initial one, in which there were the two open-loop chains. For this reason, it is necessary to reintegrate them, to observe the advantages brought by the new optimal parameters.
Running a simulation, it has been detected that at high loads many quantities, in particular the pressures, are affected by an excessive overestimation of the experimental results. The responsibility for this phenomenon lies with the correlation into the VGT open-loop chain. In fact, the VGT correlation, reported in Figure 3.8, was calibrated with a turbine efficiency multiplier equal to 1. Now that there is a new value for this parameter, it is necessary to perform a new calibration. Therefore, this further step is needed before running the last simulation.
The calibration of the VGT correlation is performed relying on the optimized engine model equipped with closed-loop controllers. As it is known, this controller typology guarantees a higher precision than the open-loop chain. So, a simulation of the engine model with EGR and VGT closed-loop controllers must be run, consulting the rack position imposed on the turbine by the VGT controller. The goal is to reproduce as much as possible the control given by the closed-loop VGT, calibrating on it the new correlation of the open-loop chain. The bisector plot of the rack position is exploited, in which there are the simulated values of the optimized engine configuration with closed-loop controllers as a function of the experimental values. The correlation is obtained through an interpolation of the rack position points, that can be of various types. In this case a second degree polynomial interpolation is chosen, performed by a dedicated Matlab

command, called "*fit*". The magenta curve in Figure 6.5 is obtained. However, this curve has been compared with the old VGT correlation and they are more or less equivalent. The problem of the overestimation at high loads remains, so another strategy must be found. The solution is to impose greater values of rack position at high loads, to have, in accordance with the GT-SUITE convention, greater openings of the turbine vanes and therefore a decrease of the boost action. In this way, the problem of the overestimation at high loads can disappear. Therefore, a VGT correlation with a greater concavity must be obtained. A curve with this feature can be got imposing the interpolation only on the rack position points of high load, that are the ones in red. The curve related to this new interpolation is the green one.

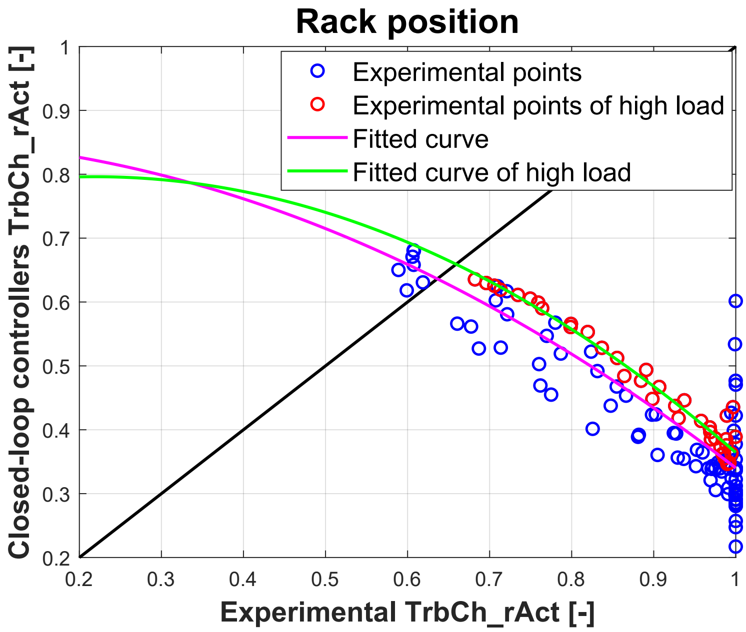

Figure 6.5: Bisector plot of the experimental rack position and of the simulated values of the optimized engine model equipped with closed-loop controllers.

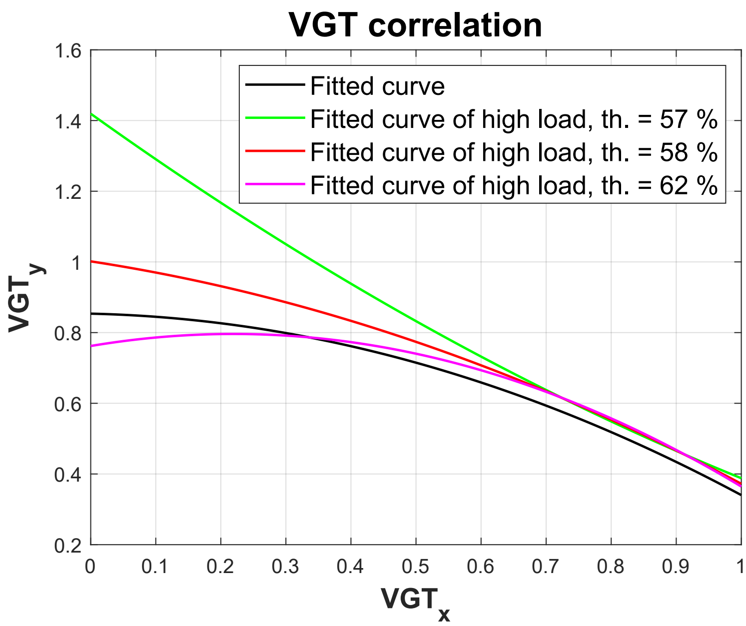

Figure 6.6: VGT correlations taking into account all the rack position points (black curve), the rack position points above 57 % (green curve), 58 % (red curve) and 62 % (magenta curve) of the experimental *BMEP*.

To select the rack position points of the high loads, a load threshold must be chosen, i.e., once this threshold is decided, only the rack position points referring to a load greater than this value are considered. This threshold is a percentage of the experimental *BMEP*, and the selected percentage is 62 %. Therefore, the green curve of Figure 6.5 is derived imposing this threshold value. Lower percentages of BMEP were explored, but the resulting curves had a completely different behavior (Figure 6.6). In fact, it is interesting to note that, decreasing the load threshold from 62 % to 58 % and from 58 % to 57 %, the concavity of the fitted curve changes completely. Using lower values of load threshold leads to curves with lower concavity, which is not the desired feature. For this reason, the value of 62 % has been selected.
The updated VGT correlation, suitable for a turbine efficiency multiplier of 1.05, can be compared with the initial correlation, as it can be observed in Figure 6.7. To medium and high values of the abscissa correspond higher values of the ordinate, and this is the desired behavior. However, considering low values of abscissa, lower values of the ordinate are obtained from the updated magenta curve. It is necessary to restore the ordinate values of the original correlation, because lower values can create problem of instability in transient simulations. In this thesis only steady-state simulations are included, but the optimized engine model must be suitable even for transient conditions. Therefore, the new definitive correlation is created in this way: the first 20 values are the ones of the original correlation, while the values from the thirtieth to the last one are of the updated correlation. Regarding the values going from position 21 to 29, they have been modified by hand, in order to get a matching between the two portions of curve. The new correlation is reported in Figure 6.8.

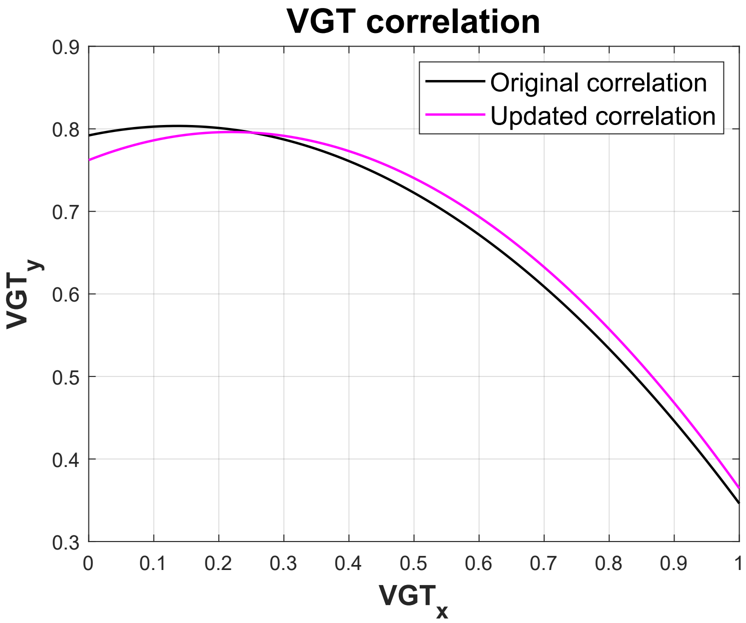

Figure 6.7: Comparison between the original correlation and the updated correlation.

Now, the new correlation can be inserted within the reserved block of the VGT open-loop chain. The ordinate values of the obtained curve are taken and imported into the block. These values are highlighted in Figure 6.9(b).
This new VGT correlation represents the last modification performed in the engine model without ATS. Now it is possible to run a final simulation and observe the results.

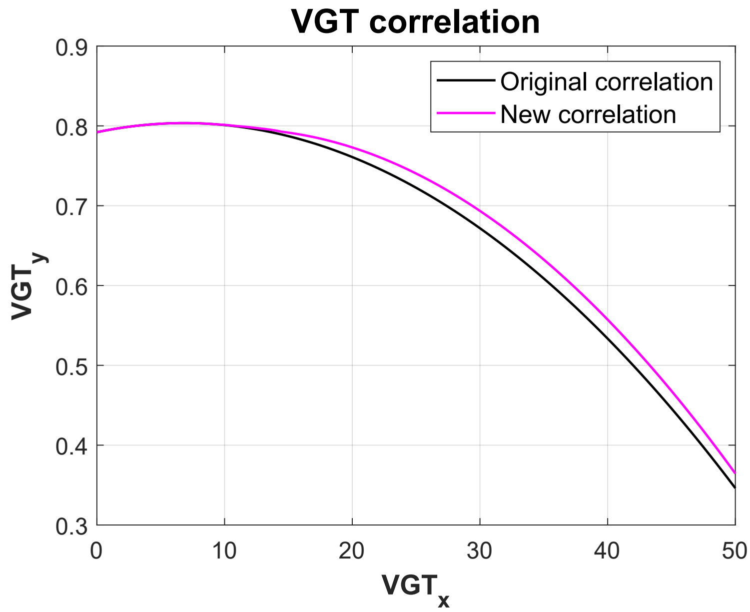

Figure 6.8: Comparison between the original correlation and the new correlation.

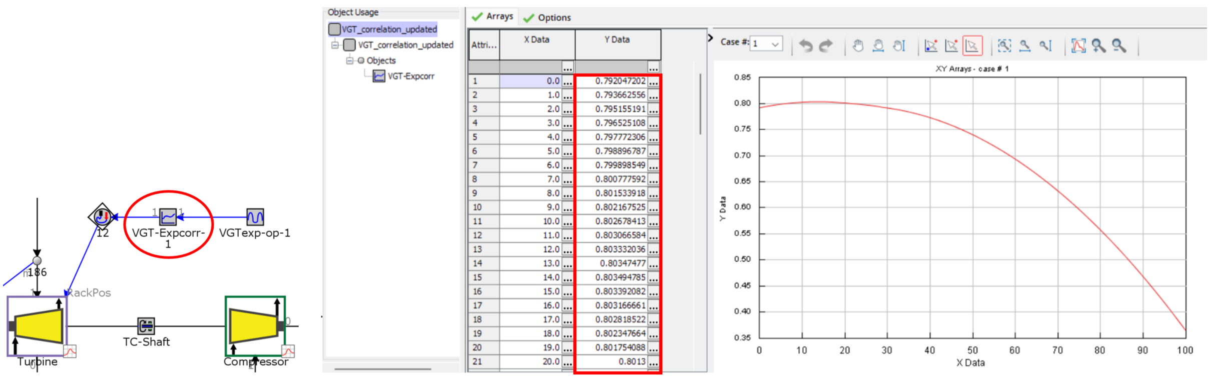

(a) (b)

Figure 6.9: New correlation inside the VGT correlation block.

6.3 Final simulation and comparison with the initial configuration

The final version of the engine model without ATS was obtained. The related simulation can be run, examining all the main quantities and comparing them with the ones of the primitive version of the engine model without ATS. To have a complete overview of the results provided by the model, some new quantities are introduced. Indicating them always in accordance with the department dictionary, they are:

- *megr_CO2_EGR*: EGR mass flow rate;
- *Lambda*: relative air-fuel ratio;
- *eta_volumetric_IM*: volumetric efficiency referred to the intake manifold;
- *NOx_exh*: NOx concentration at catalyst upstream.

For each quantity, the same plot types shown in chapter 2 are shown: the experimental and simulated quantities as a function of the case number and the related bisector plot. There are two simulated trends in each plot, i.e. the one related to the optimized engine model without

ATS and the one related to the initial configuration, with the aim of performing a comparison. All the squared correlation coefficients and the root mean square errors are collected respectively in Tables 6.1 and 6.2.
Starting with the average fuel consumption during the test (Figure 6.10), all trends, so both simulated and experimental ones, overlap. This is due to the reason already explained in the second chapter, i.e. the imposition of the experimental fuel mass per pulse within the injector object of the model.

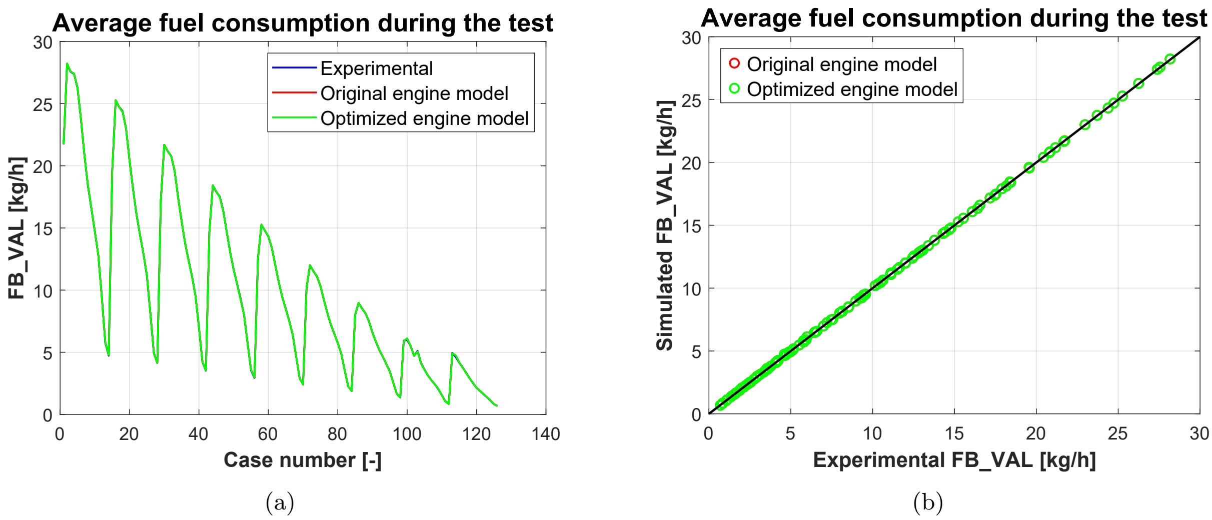

Figure 6.10: Comparison of the average fuel consumption during the test between the original and the optimized engine model without ATS: experimental and simulated trends as a function of the case number **(a)**; bisector plot **(b)**.

Then there are the wet and dry air mass flow rates, reported respectively in Figures 6.11 and 6.12. The variation between the results given by the original engine model and by the optimized configuration is not so distinguishable only by looking at the diagrams. The change can be observed referring to the *RMSE* values of Table 6.2. The final engine layout gets slightly worse the experimental prediction of these quantities.

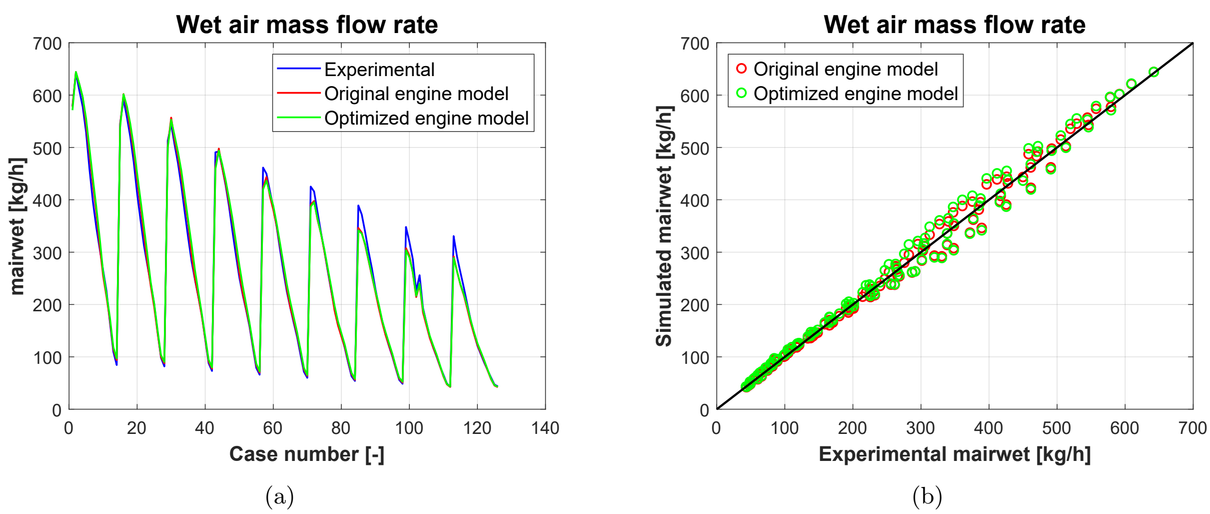

Figure 6.11: Comparison of the wet air mass flow rate between the original and the optimized engine model without ATS: experimental and simulated trends as a function of the case number **(a)**; bisector plot **(b)**.

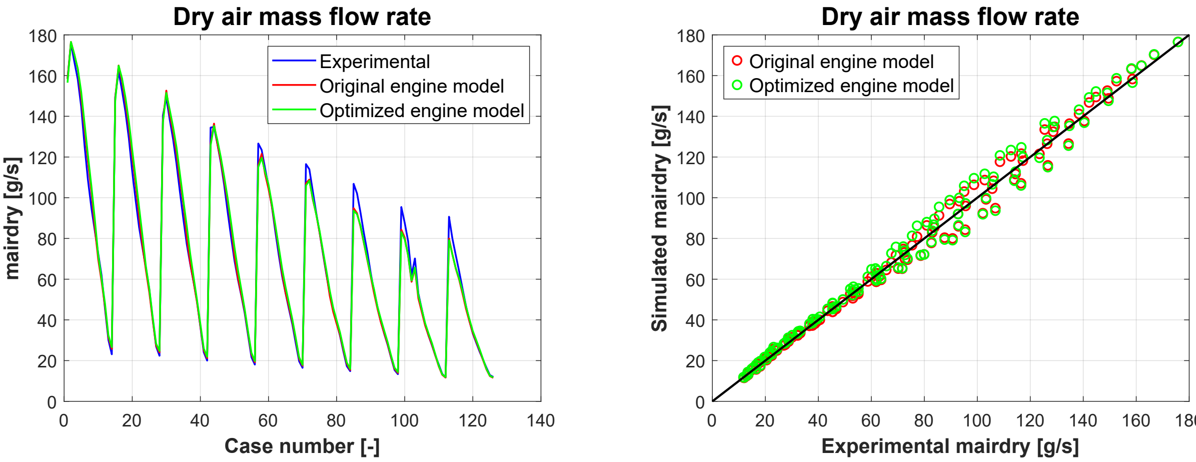

(a) (b)

Figure 6.12: Comparison of the dry air mass flow rate between the original and the optimized engine model without ATS: experimental and simulated trends as a function of the case number **(a)**; bisector plot **(b)**.

Regarding the first of the new quantities, so the EGR mass flow rate, shown in Figure 6.13, there is not a uniform behavior. At high loads the simulated trends follow in better way the experimental one, while increasing the case number the estimate gets worse. In fact, in the upper peaks, at medium and low load, there is an underestimation of the experimental results. The two simulated trends are more or less equivalent and this is confirmed by the two *RMSE* values, that are very similar.

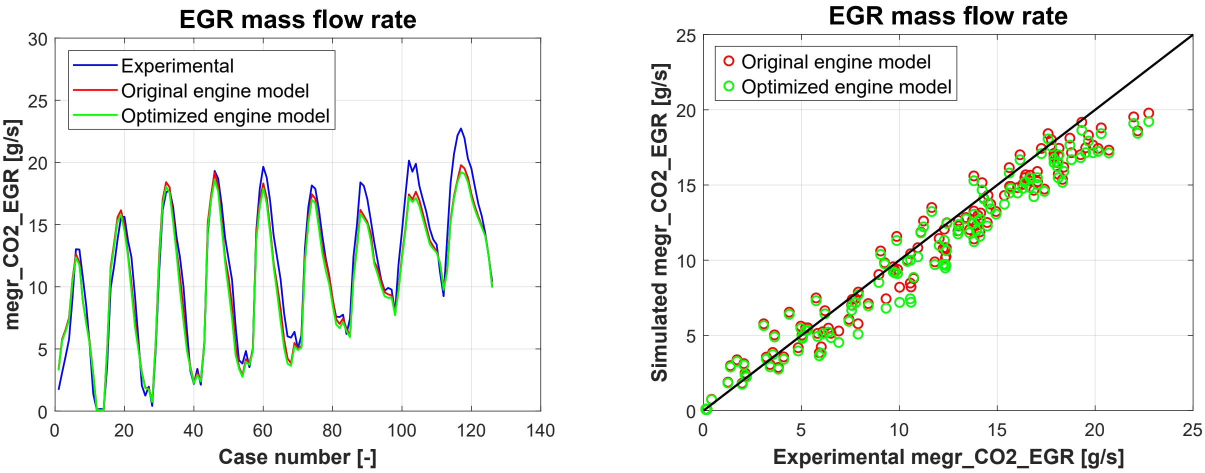

(a) (b)

Figure 6.13: Comparison of the EGR mass flow rate between the original and the optimized engine model without ATS: experimental and simulated trends as a function of the case number **(a)**; bisector plot **(b)**.

Another new quantity that contributes to the completeness of the results is the relative air-fuel ratio *Lambda*. The two simulated trends are directly computed exploiting the simulated *mairwet* and *FB_VAL*, according the equation 6.1, in which $\dot{m}_{air} = mairwet$ and $\dot{m}_{fuel} = FB\_VAL$.

$$\lambda = \frac{\frac{\dot{m}_{air}}{\dot{m}_{fuel}}}{\alpha_{st}} \tag{6.1}$$

The α_{st} parameter is the stoichiometric air-fuel ratio, taken from the experimental data set and equal to 14.61.

The *Lambda* quantity is reported in Figure 6.14, where it is possible to see that in most cases the two simulated trends overestimation the experimental one. This occurs particularly in correspondence of the decreasing slopes of the wet air mass flow rate diagram, in which the simulated *mairwet* are a little higher than the experimental one. Therefore, according to the relation 6.1, the relative air-fuel ratio provided by the models overestimates its experimental values. Instead, in correspondence with the upper peaks at medium and low loads, the experimental relative air-fuel ratio is higher than the simulated trends. This is always due to the simulated *mairwet* behavior. Furthermore, the results provided by the optimized engine model have a more accentuated tendency, both about the overestimation and underestimation of the experimental values. However, from a global point of view, the two root mean square errors are pretty similar.

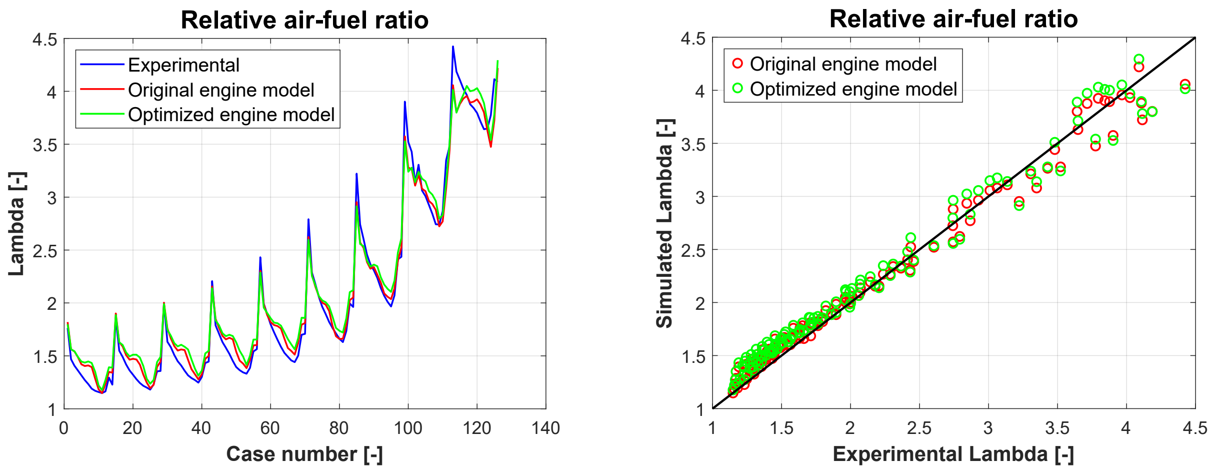

(a) (b)

Figure 6.14: Comparison of the relative air-fuel ratio between the original and the optimized engine model without ATS: experimental and simulated trends as a function of the case number **(a)**; bisector plot **(b)**.

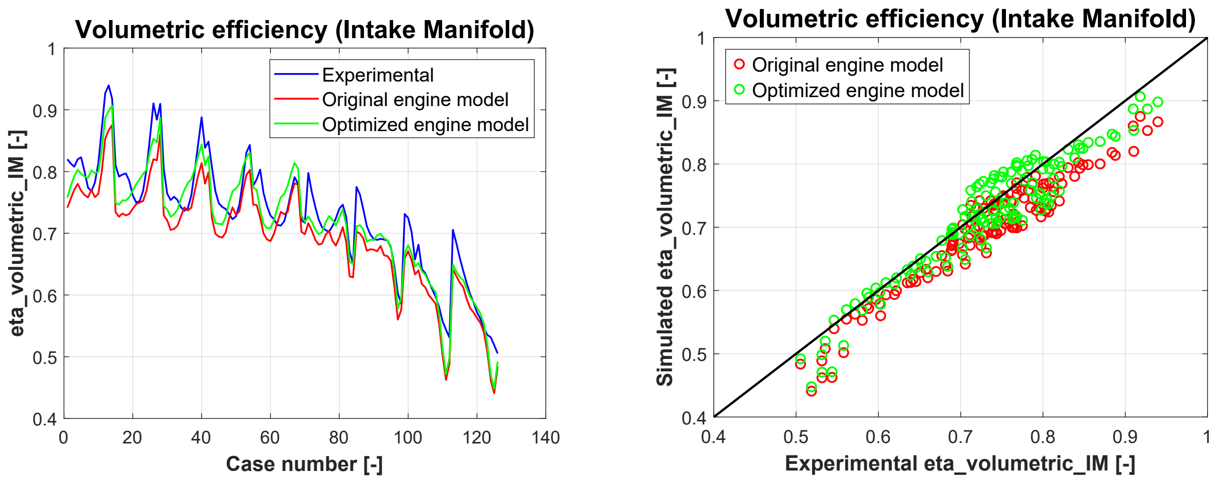

(a) (b)

Figure 6.15: Comparison of the volumetric efficiency related to the intake manifold between the original and the optimized engine model without ATS: experimental and simulated trends as a function of the case number **(a)**; bisector plot **(b)**.

A quantity that cannot be neglected is the volumetric efficiency *eta_volumetric_IM*, shown in Figure 6.15. Volumetric efficiency is a parameter that evaluates the ability of the engine intake and exhaust systems to work as an air pumping device. It can be defined as the "measure of the breathing efficiency of an engine" [9]. The formulation of volumetric efficiency (6.2) shows that it is defined as the ratio between m_{air}, i.e. the air mass per cycle and per cylinder, and $m_{air,id}$, which is the ideal reference mass, i.e. the air mass that could enter the cylinder ideally.

$$\lambda_v = \frac{m_{air}}{m_{air,id}} = \frac{m_{air}}{\rho_{air} V_d} = \frac{\dot{m}_{air}}{\rho_{air} i V_d \frac{n}{2}} \tag{6.2}$$

$\dot{m}_{air}$ is the air mass flow rate into the engine, iV_d is the total engine displacement and n is the engine speed. Regarding ρ_{air}, it is the air density, that can be evaluated in two different ways, based on the engine type. For the naturally aspirated engines, it is equal to the enviromental air density, so the relation $\rho_{air} = \rho_{amb}$ holds, while for the turbo-charged engine, like the engine of this thesis, the air density is evaluated by the intake manifold thermodynamic conditions, therefore $\rho_{air} = \rho_{IM}$.
The simulated trends were not computed, but were taken directly from GT-POST outcomes. From a first analysis, it can be observed that they do not estimate perfectly the experimental trend. However, observing both the squared correlation coefficients and the root mean square errors, actually they have a good behavior. Furthermore, the optimized configuration exhibits a lower $RMSE$, probably thanks to, as it will be possible to observe, the improvement of the intake manifold pressure, necessary for the computation of λ_v executed by the software.

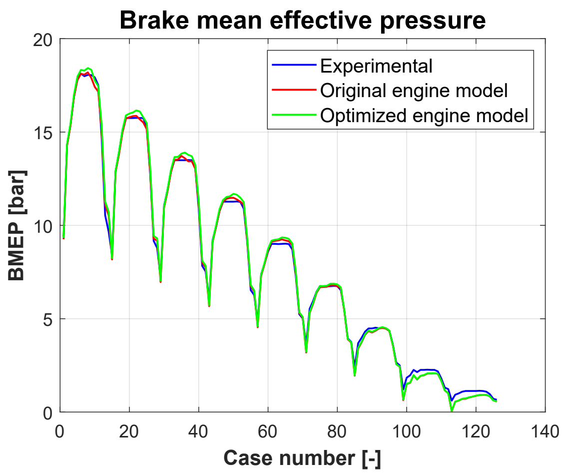

(a)

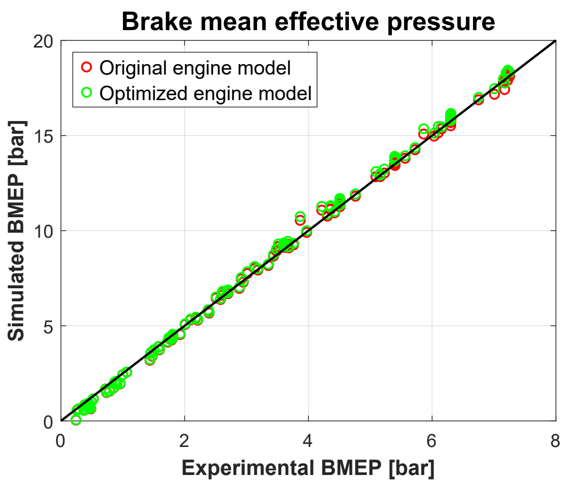

(b)

Figure 6.16: Comparison of the brake mean effective pressure between the original and the optimized engine model without ATS: experimental and simulated trends as a function of the case number **(a)**; bisector plot **(b)**.

Then there is the brake mean effective pressure (6.16), whose trend given by the optimized engine model gets slightly worse at high loads. In fact, having greater values of simulated $BMEP$ leads to an overestimation of the experimental values. These higher values of $BMEP$ can be explained by the exhaust gases temperatures that, as it will be possible to observe, decrease, so less thermal energy is given to the exhaust and more work is provided by the engine. This is the compromise to accept for having a relevant improvement of the experimental prediction of the exhaust temperatures, which represents one of the most important results of this thesis.
Regarding the absolute pressure at the intake manifold, it is shown in Figure 6.17. It can be noted that at high loads, the optimized engine configuration brings an improvement of the experimental estimate. In fact, the trend provided by the original engine layout overestimates the experimental values, while the new trend is very close to them. This good behavior is mainly due to the new VGT correlation, by which the VGT open-loop control can work much better at high loads.

Decreasing the load more and more leads to a general underestimation of the experimental results, even greater considering the trend of the optimized engine model. This behavior, exhibited by both engine models, is substantially due to a limit of the open-loop control, that does not guarantee the same level of precision of the closed-loop one. However, to maintain the presence of the open-loop control, it is an acceptable behavior.

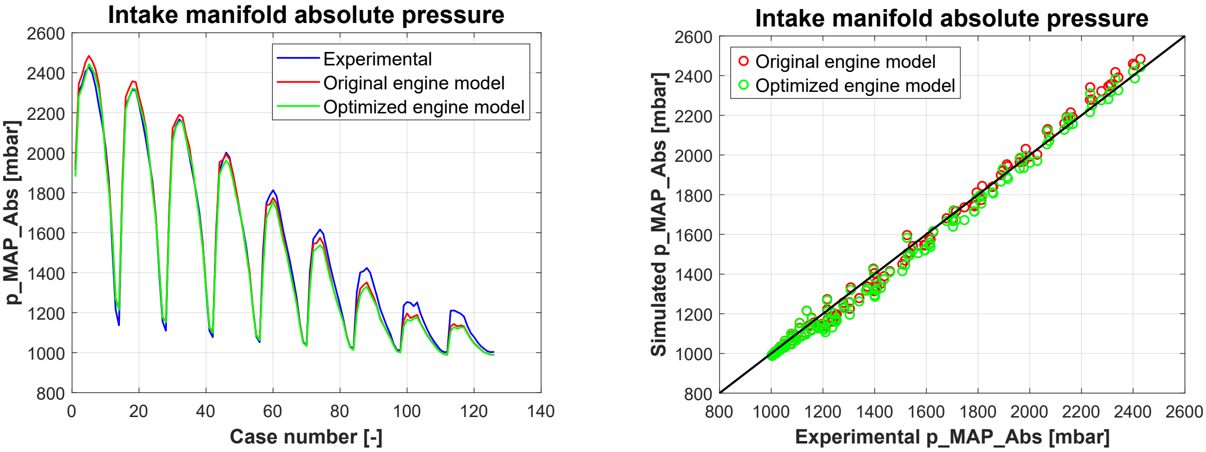

(a) (b)

Figure 6.17: Comparison of the intake manifold absolute pressure between the original and the optimized engine model without ATS: experimental and simulated trends as a function of the case number **(a)**; bisector plot **(b)**.

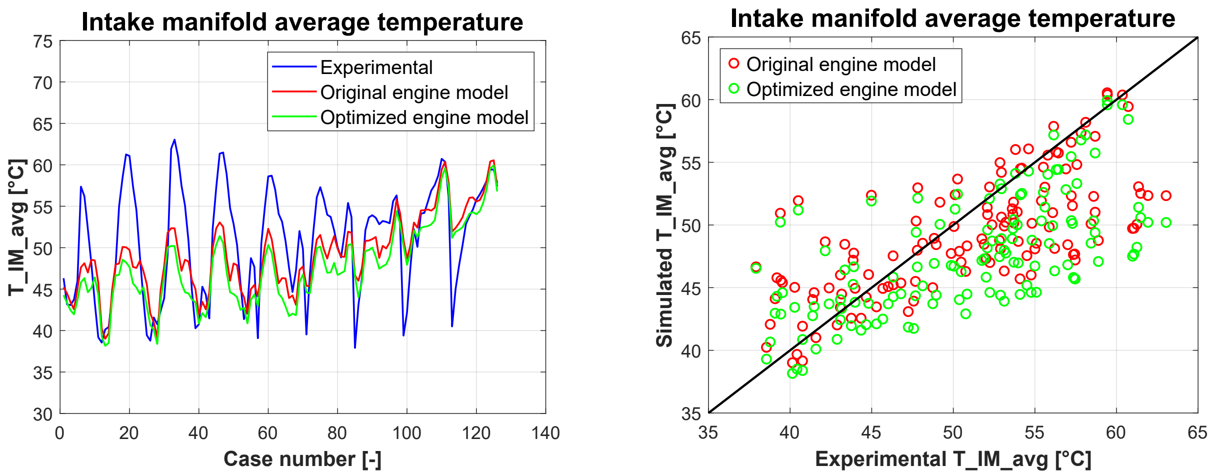

(a) (b)

Figure 6.18: Comparison of the intake manifold average temperature between the original and the optimized engine model without ATS: experimental and simulated trends as a function of the case number **(a)**; bisector plot **(b)**.

The intake manifold average temperature *T_IM_avg* is reported in Figure 6.18. There is again difficulty for the engine model to follow the experimental trend for this quantity. The optimized layout has also trouble estimating the experimental results, showing even less ability, as it can be observed in the *RMSE* table. The main reason is always the dependence on the EGR, which makes difficult the thermodynamic modelling of the intake manifold. As it will be shown, the EGR percentage estimate will get worse in the optimized engine configuration, and this explains the greater *RMSE* value of the final engine model *T_IM_avg* trend. However, considering the scale covered by the trends values, the discrepancies are acceptable.

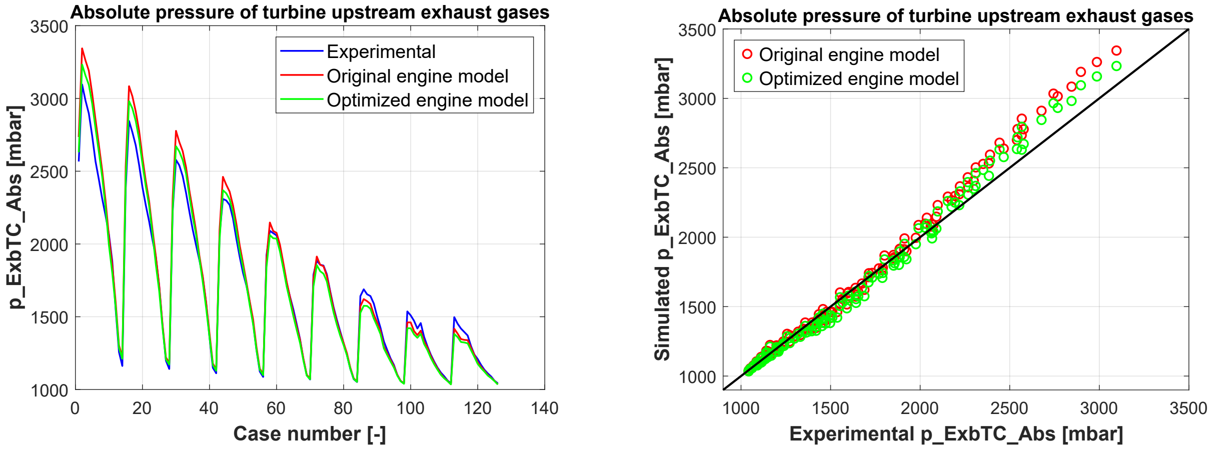

(a) (b)

Figure 6.19: Comparison of the absolute pressure of turbine upstream exhaust gases between the original and the optimized engine model without ATS: experimental and simulated trends as a function of the case number **(a)**; bisector plot **(b)**.

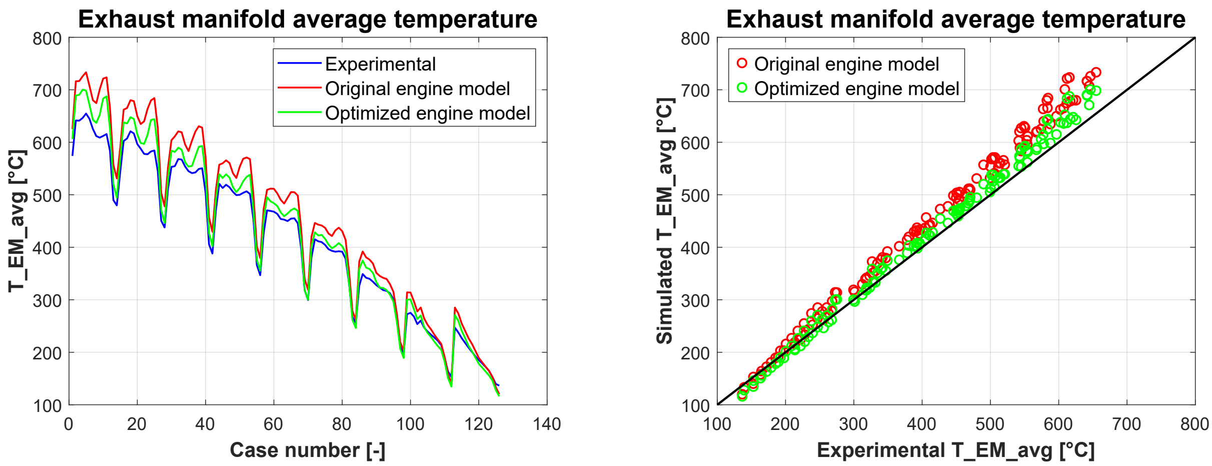

(a) (b)

Figure 6.20: Comparison of the exhaust manifold average temperature between the original and the optimized engine model without ATS: experimental and simulated trends as a function of the case number **(a)**; bisector plot **(b)**.

Concerning the absolute pressure within the exhaust manifold (Figure 6.19), the final engine layout exhibits an improvement in the experimental estimate at high loads. The merit of this goes to the new turbine efficiency multiplier that, as was shown in the previous chapter, has the effect of reducing the intake manifold pressure with its enhancement. This is confirmed by the $RMSE$ value, which reduces from 98.068 mbar to 75.325 mbar.
The average temperature of the exhaust manifold, shown in Figure 6.20, like all other exhaust temperatures, exhibits the greatest effect of the optimization procedure performed in the engine model without ATS. The T_EM_avg reduces in a relevant extent, approaching a lot the experimental trend. This is the effect brought by all the modifications introduced in the optimization phase, in particular by the changes of the coolant and oil boundary conditions within the cylinder object. There are also the small contributes of the new external convection coefficient inside the exhaust pipes thermal model, of the new value of the orifice diameter at the flap downstream and also of the new turbine efficiency multiplier. All these changes lead to a reduction of the $RMSE$ value from 47.618 °C to 23.826 °C, reduction that can be appreciated even by looking at the bisector plot, in which the green points cloud is closer to the bisector than the red points one.

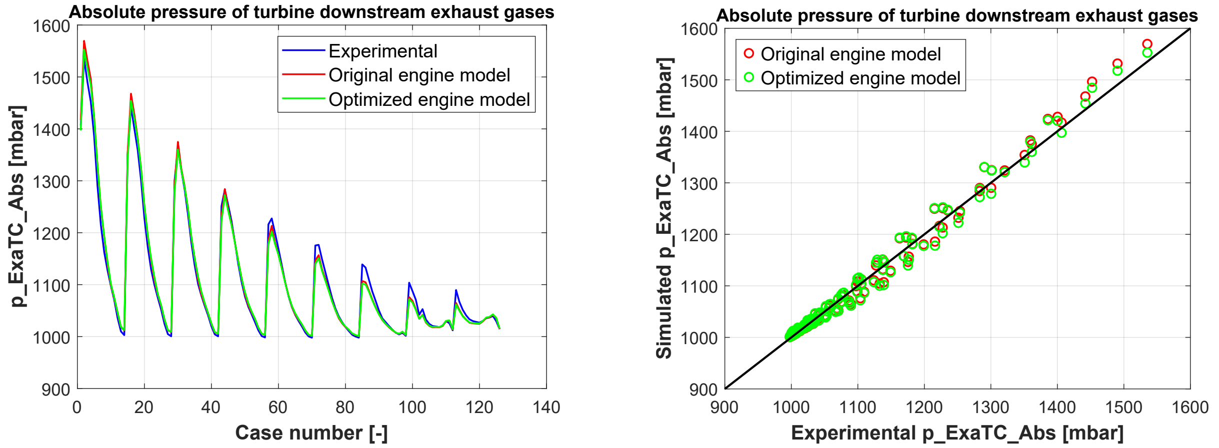

(a) (b)

Figure 6.21: Comparison of the absolute pressure of turbine downstream exhaust gases between the original and the optimized engine model without ATS: experimental and simulated trends as a function of the case number **(a)**; bisector plot **(b)**.

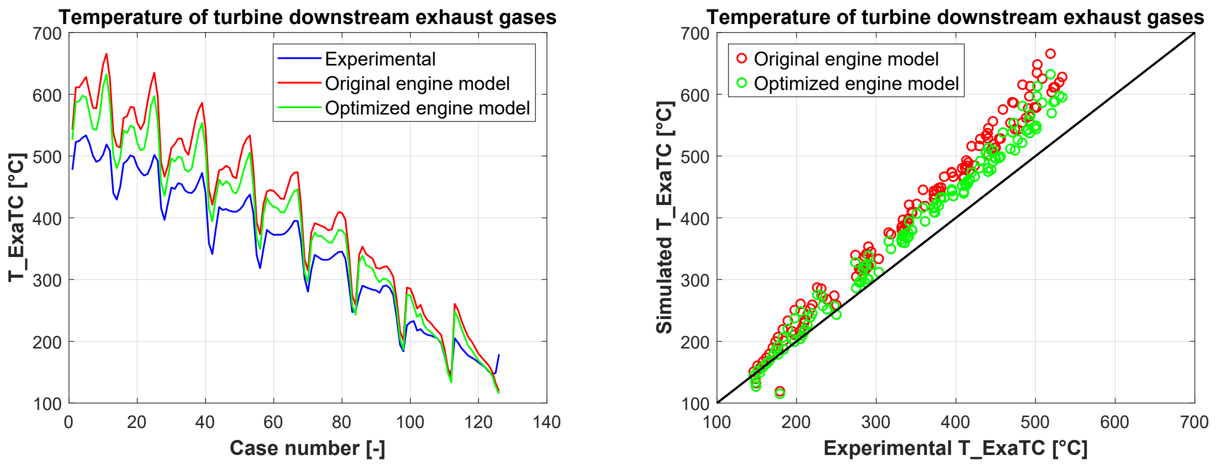

(a) (b)

Figure 6.22: Comparison of the temperature of turbine downstream exhaust gases between the original and the optimized engine model without ATS: experimental and simulated trends as a function of the case number **(a)**; bisector plot **(b)**.

The absolute pressure of the exhaust gases at turbine downstream (Figure 6.21) does not show a relevant change between the initial and the final engine model. There is only a slight reduction in the simulated pressure of the optimized engine model, but it is negligible.
Regarding the temperature *T_ExaTC*, there is the same effect observed in *T_EM_avg*. The extent of reduction can be observed on the $RMSE$ values, in which the one of the optimized engine model decreases approximately by 24 °C, exactly like the case of the exhaust manifold temperature. The difference is that the simulated *T_ExaTC* of the initial engine layout starts with a major level of overestimation, and consequently the new simulated trend does not reach the same amount of approaching of the *T_EM_avg* one. However, the quality of the result can be considered satisfactory.
Now, there are the quantities related to the single engine cylinder. The third cylinder is again chosen, mainly to perform the comparison with the original engine model. There are again the maximum pressure inside the combustion chamber *PMAX3* (Figure 6.23), the net indicated mean effective pressure *IMEP3* (Figure 6.24), the gross indicated mean effective pressure *IMEPH3* (Figure 6.25), the pumping mean effective pressure *IMEPL3* (Figure 6.26) and the total friction

mean effective pressure *TFMEP3* (Figure 6.27). Apart *PMAX3*, in which the optimized engine model shows a slightly worse behavior due to a greater underestimation at high loads, the two indicated mean effective pressures have a small improvement with the optimization procedure, and the pumping and total friction mean effective pressures have practically the same behavior.

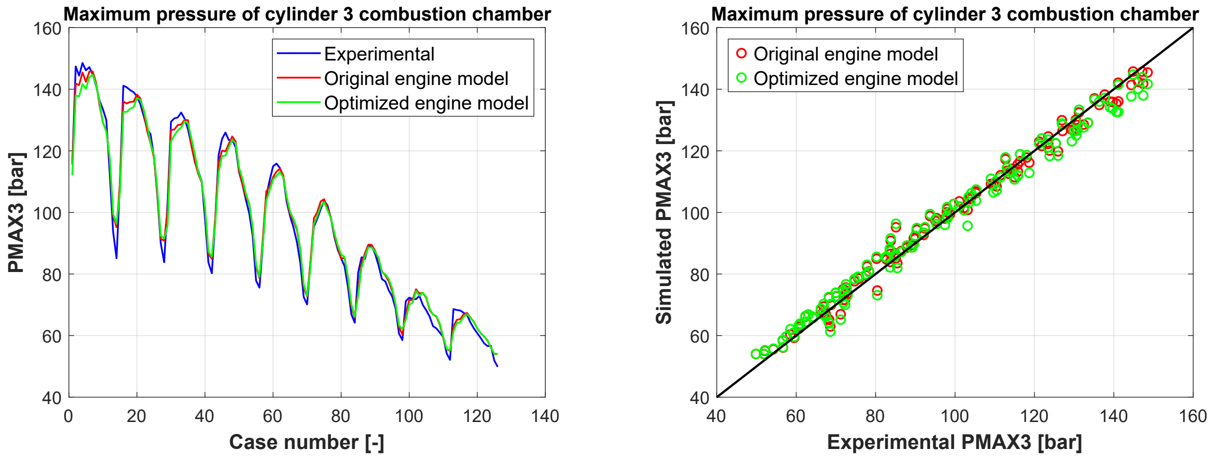

(a) (b)

Figure 6.23: Comparison of the maximum pressure of cylinder 3 combustion chamber between the original and the optimized engine model without ATS: experimental and simulated trends as a function of the case number **(a)**; bisector plot **(b)**.

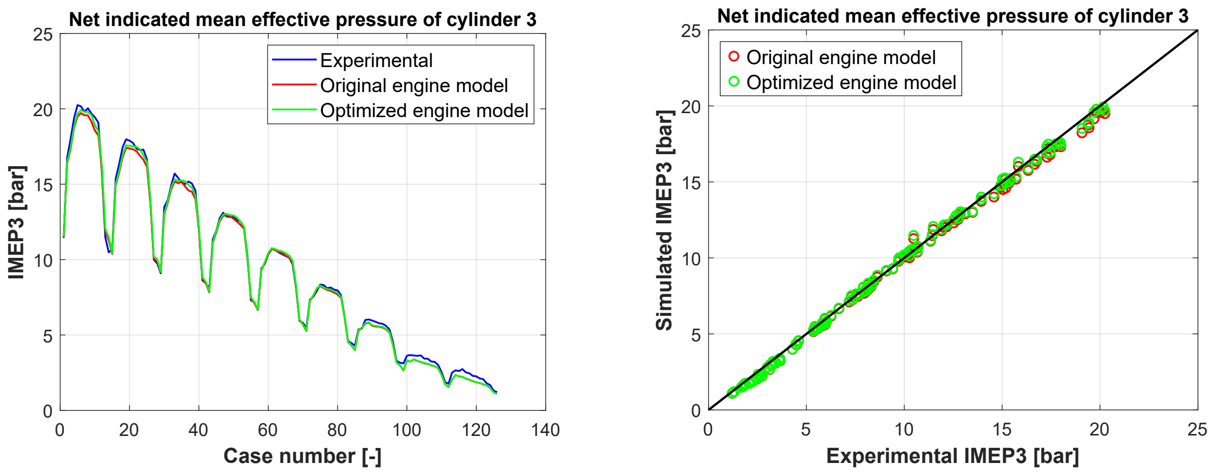

(a) (b)

Figure 6.24: Comparison of the net indicated mean effective pressure of cylinder 3 between the original and the optimized engine model without ATS: experimental and simulated trends as a function of the case number **(a)**; bisector plot **(b)**.

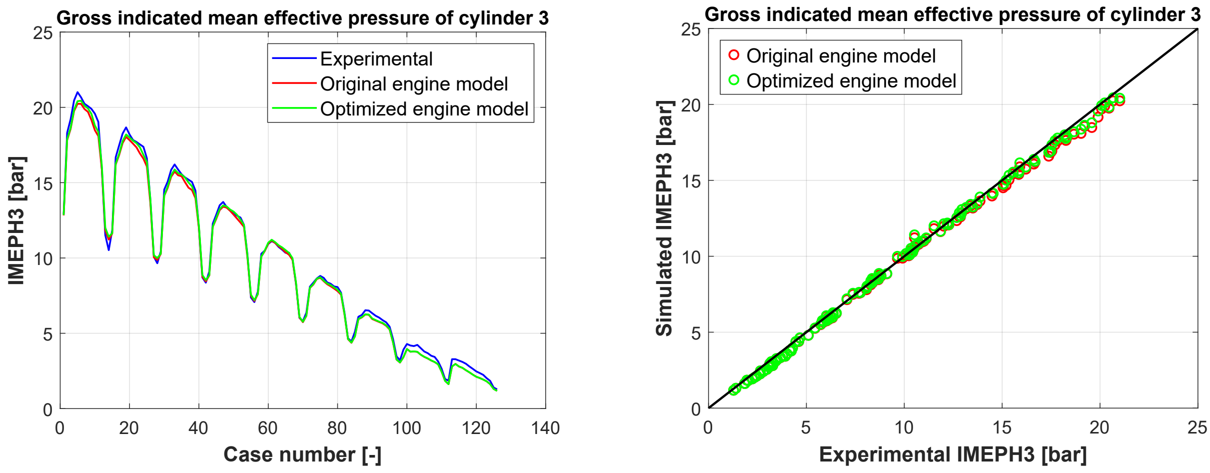

(a) (b)

Figure 6.25: Comparison of the gross indicated mean effective pressure of cylinder 3 between the original and the optimized engine model without ATS: experimental and simulated trends as a function of the case number **(a)**; bisector plot **(b)**.

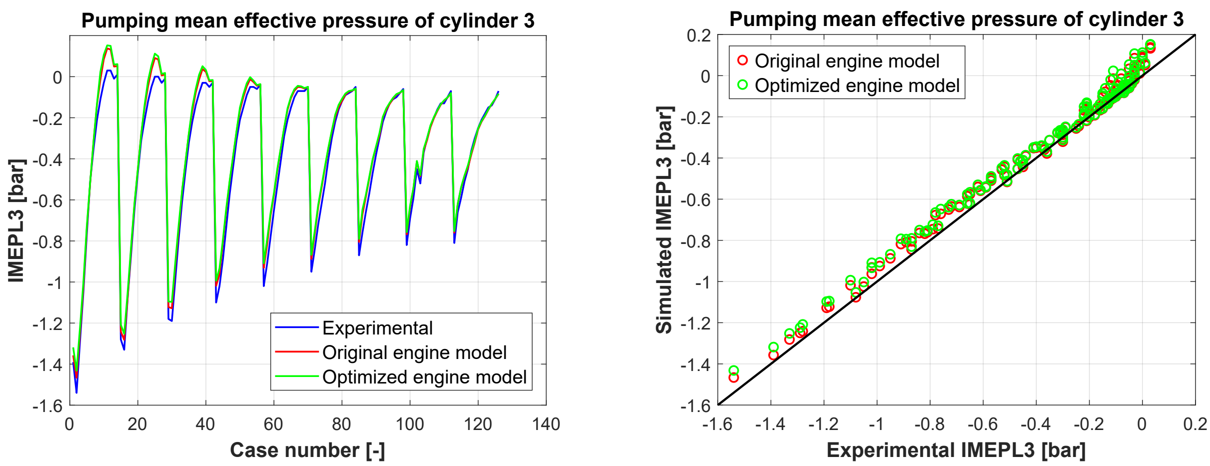

(a) (b)

Figure 6.26: Comparison of the pumping mean effective pressure of cylinder 3 between the original and the optimized engine model without ATS: experimental and simulated trends as a function of the case number **(a)**; bisector plot **(b)**.

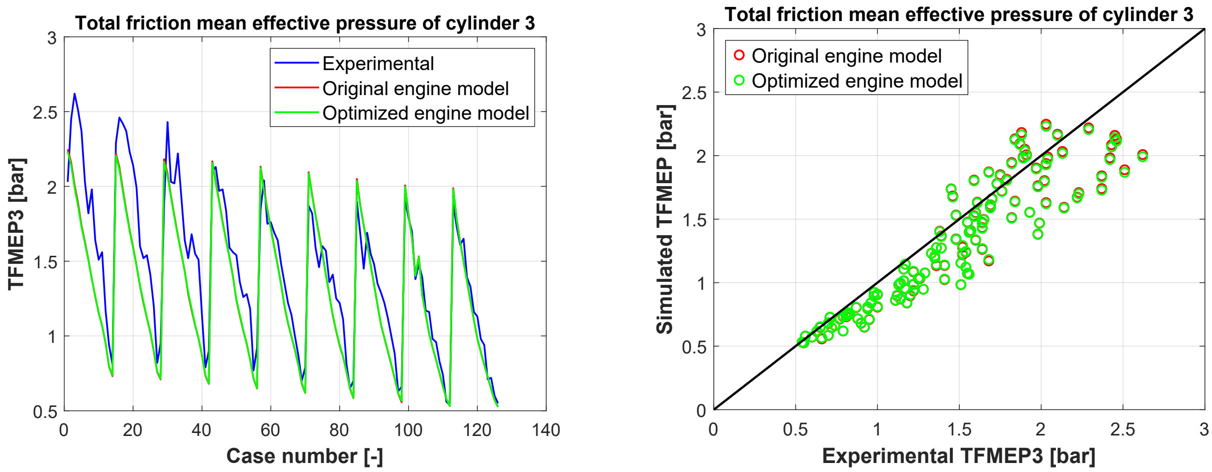

(a) (b)

Figure 6.27: Comparison of the total friction mean effective pressure of cylinder 3 between the original and the optimized engine model without ATS: experimental and simulated trends as a function of the case number **(a)**; bisector plot **(b)**.

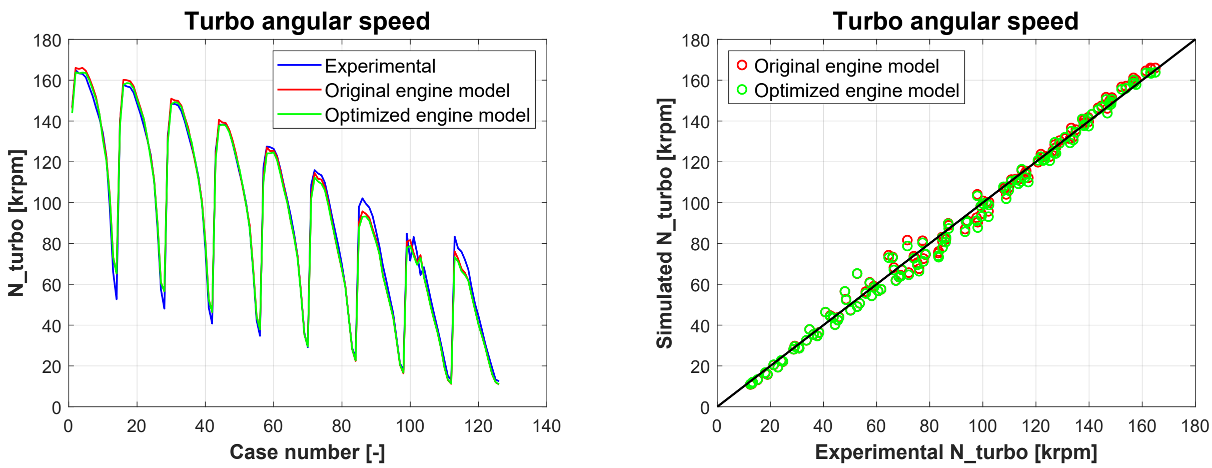

(a) (b)

Figure 6.28: Comparison of the turbo angular speed between the original and the optimized engine model without ATS: experimental and simulated trends as a function of the case number **(a)**; bisector plot **(b)**.

Regarding the turbo angular speed (Figure 6.28), there is a little improvement at high loads brought by the optimized configuration. However, the greater amount of underestimation at medium and low loads provided by the new engine layout leads to a little increase of the $RMSE$ value, but it is a value that can be accepted.
The EGR percentage (Figure 6.29) shows a worsening with the optimized engine configuration. The reason could be the need of recalibration of the EGR open-loop correlation. In fact, since important modifications were made, a similar procedure adopted for the VGT recalibration could be necessary. The starting point would be the same, hence the optimized engine model equipped with closed-loop controllers. However, while in the VGT case there was a known direction, i.e. the recalibration of the correlation giving priority to the high loads, in the EGR percentage case there is worse behavior more or less at all the load levels, so it would be more onerous to find a new EGR correlation that improves the estimate of the experimental quantities related to EGR.
About the boost pressure (Figure 6.30), the behavior is similar to the one observed about the intake manifold absolute pressure. At high loads, the simulated trend of the optimized engine

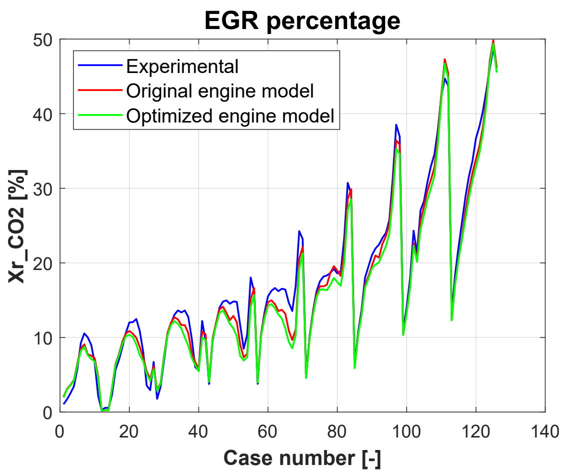

(a)

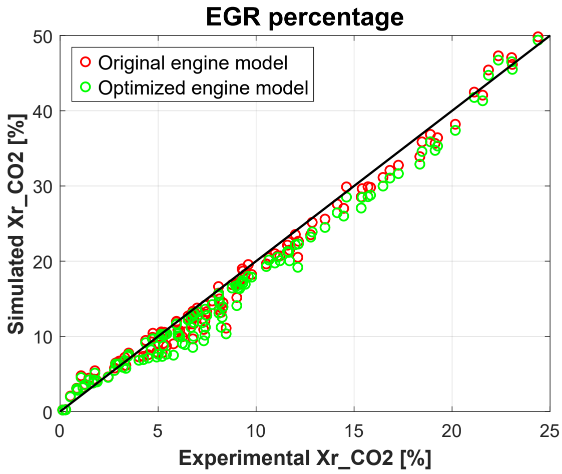

(b)

Figure 6.29: Comparison of the EGR percentage between the original and the optimized engine model without ATS: experimental and simulated trends as a function of the case number **(a)**; bisector plot **(b)**.

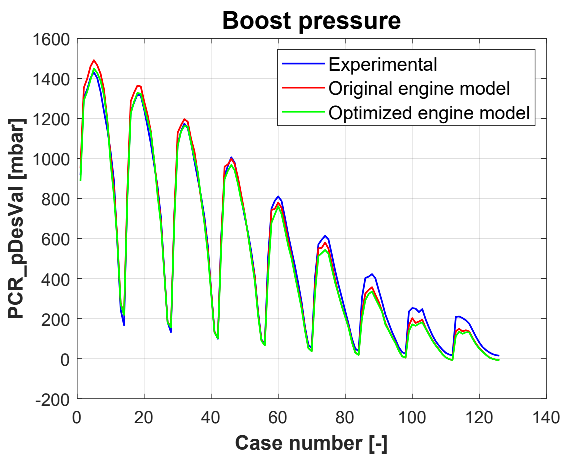

(a)

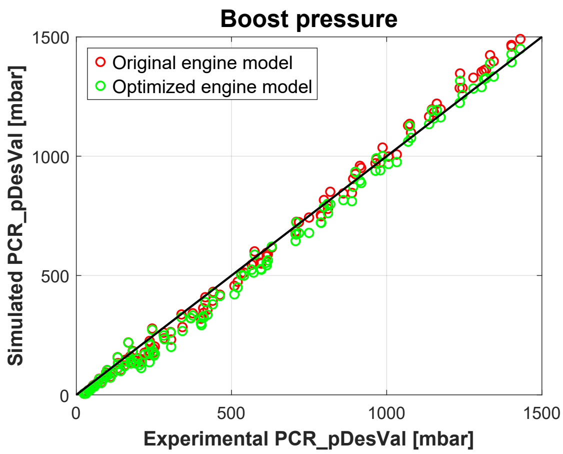

(b)

Figure 6.30: Comparison of the boost pressure between the original and the optimized engine model without ATS: experimental and simulated trends as a function of the case number **(a)**; bisector plot **(b)**.

model follows in a better way the experimental one, thanks to the new correlation within the VGT open-loop chain. The disadvantage is that at medium and low loads there is further level of underestimation for the new green trend, leading to an increase of the $RMSE$ value.
Regarding the flap downstream absolute pressure, shown in Figure 6.31, there is not a relevant change between the initial and the final engine models. In fact, in both cases the precision of the experimental results estimate is very high. In contrast, for the flap downstream temperature there is an important change introduced with the new engine layout, as it can be seen in Figure 6.32. The effect is similar to the one observed for two previous exhaust gases temperatures T_EM_avg and T_ExaTC. The discrepancy between the simulated temperature and the experimental one is reduced, looking also at the bisector plot. The amount of reduction is equivalent to the previous case, i.e. a $RMSE$ decrease of about 24 °C.

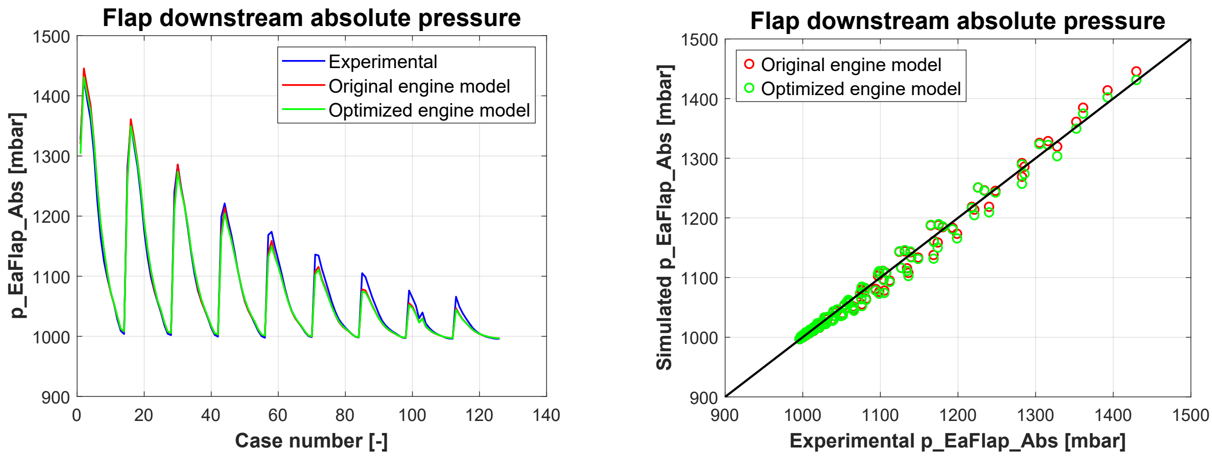

(a) (b)

Figure 6.31: Comparison of the flap downstream absolute pressure between the original and the optimized engine model without ATS: experimental and simulated trends as a function of the case number **(a)**; bisector plot **(b)**.

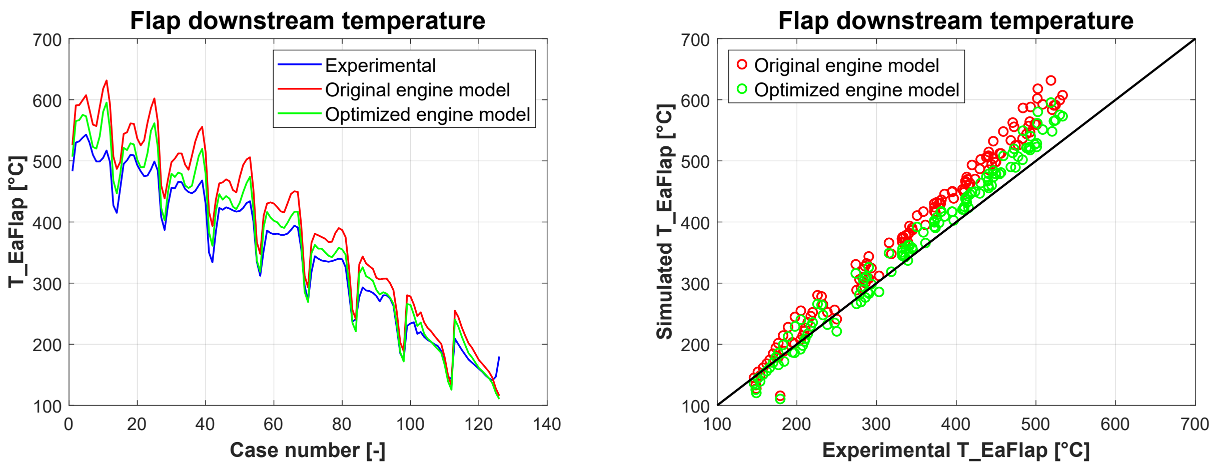

(a) (b)

Figure 6.32: Comparison of the flap downstream temperature between the original and the optimized engine model without ATS: experimental and simulated trends as a function of the case number **(a)**; bisector plot **(b)**.

The last quantity that is worth analyzing concern the nitrogen oxides concentration at catalyst upstream, reported in Figure 6.33. These molecules are one of the most relevant pollutant emissions of the diesel engine, and there is a need to reduce them for complying with the new legislations, which are more and more rigorous. The mechanism of formation of these pollutants is difficult to model inside the software, therefore the simulated trends do not follow in a precise way the simulated results. However, a certain degree of precision can be reached, looking at the square correlation coefficients of Table 6.1, which are above 0.9. The introduction of the new modifications into the engine model leads to a worsening of the experimental prediction, which however can be considered acceptable given the general difficulty to estimate this quantity.

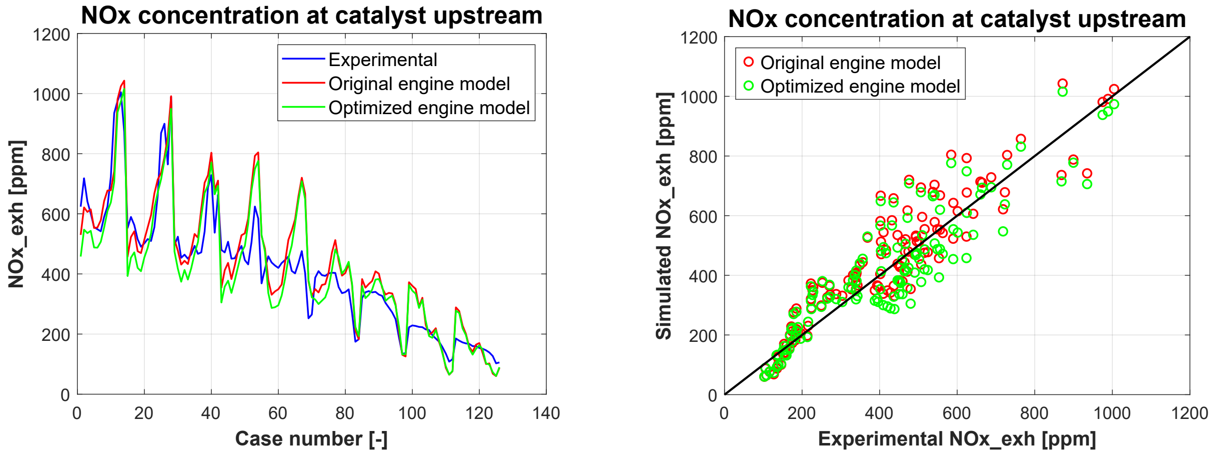

(a) (b)

Figure 6.33: Comparison of the NOx concentration at catalyst upstream between the original and the optimized engine model without ATS: experimental and simulated trends as a function of the case number **(a)**; bisector plot **(b)**.

	Original engine model	**Optimized engine model**
FB_VAL	1.000	1.000
mairwet	0.996	0.994
mairdry	0.996	0.994
megr_CO2_EGR	0.980	0.977
Lambda	0.994	0.990
eta_volumetric_IM	0.963	0.950
BMEP	0.999	0.999
p_MAP_Abs	0.997	0.996
T_IM_avg	0.707	0.662
p_ExbTC_Abs	0.996	0.995
T_EM_avg	0.997	0.998
p_ExaTC_Abs	0.995	0.993
T_ExaTC	0.992	0.993
PMAX3	0.996	0.992
IMEP3	0.999	0.999
IMEPH3	0.999	0.999
IMEPL3	0.996	0.995
TFMEP3	0.918	0.918
N_turbo	0.997	0.996
Xr_CO2	0.993	0.990
PCR_pDesVal	0.998	0.997
p_EaFlap_Abs	0.995	0.993
T_EaFlap	0.992	0.993
NOx_exh	0.926	0.900

Table 6.1: Root mean square errors $RMSE$ of the original engine model and of the optimized engine model.

	Original engine model	Optimized engine model
FB_VAL	0.037 kg/h	0.037 kg/h
mairwet	14.318 kg/h	18.085 kg/h
mairdry	3.969 g/s	4.998 g/s
megr_CO2_EGR	1.428 g/s	1.667 g/s
Lambda	0.124	0.155
eta_volumetric_IM	0.044	0.032
BMEP	0.226 bar	0.270 bar
p_MAP_Abs	41.256 mbar	48.171 mbar
T_IM_avg	4.928 °C	5.894 °C
p_ExbTC_Abs	98.068 mbar	75.325 mbar
T_EM_avg	47.618 °C	23.826 °C
p_ExaTC_Abs	14.244 mbar	14.795 mbar
T_ExaTC	68.241 °C	44.746 °C
PMAX3	2.830 bar	3.742 bar
IMEP3	0.332 bar	0.278 bar
IMEPH3	0.354 bar	0.292 bar
IMEPL3	0.050 bar	0.061 bar
TFMEP3	0.256 bar	0.257 bar
N_turbo	3.720 krpm	4.027 krpm
Xr_CO2	1.598 %	2.213 %
PCR_pDesVal	39.670 mbar	45.894 mbar
p_EaFlap_Abs	10.184 mbar	11.650 mbar
T_EaFlap	68.241 °C	44.746 °C
NOx_exh	86.632 ppm	91.998 ppm

Table 6.2: Squared correlation coefficients R^2 of the original engine model and of the optimized engine model.

Chapter 7

Conclusions

The goal of this thesis was to validate a GT-SUITE model of a 3.0L diesel engine through a series of steady-state tests. The activity began with a description of the two engine model versions initially available: one equipped with an After-Treatment System (ATS), but featuring unphysical heat transfer coefficients to accurately predict exhaust temperatures and the other without an ATS, but implementing physically consistent heat transfer coefficients, which, however, led to an overestimation of the exhaust temperatures.
For this reason, the thesis focused on the second engine model, with the goal of improving its accuracy in exhaust gas temperature estimate, while maintaining physical consistency.
Subsequently, before performing a detailed comparison between the two engine models, closed-loop controllers were introduced into the engine model without the ATS, in order to have the same controller setup for the two models.
Several GT-ISE parameters were analyzed to understand their effects on the engine behavior and how they could be adjusted to enhance model accuracy. As a result, the engine model without ATS was optimized, significantly improving the prediction of exhaust gas temperatures as well as the pressure at the turbine inlet. The optimization process involved adjustments to the boundary conditions of the coolant and oil within the cylinder object, the hole diameter of the orifice located downstream of the flap, the external convection coefficient of the thermal model within the exhaust pipes, and the turbine efficiency multiplier. All these modifications were made while respecting physical constraints, particularly for the cylinder boundary conditions and the external convection coefficient. In this way, physical consistency was ensured for the engine model, while also achieving greater prediction accuracy for the aforementioned engine parameters.
The trade-off was a slight deterioration in the prediction of other quantities, with the exception of the average fuel consumption during the test and the total friction mean effective pressure, which remained practically unaffected. However, this represents a good compromise. Furthermore, volumetric efficiency as well as the net and gross indicated mean effective pressures showed slight improvements with the optimized configuration.
Regarding future developments for the refined engine model, one possible direction is the re-assessment of the engine layout through new steady-state tests, in order to evaluate the effects of different operating conditions. In addition, a subsequent step will be the implementation of the already available ATS model. Finally, another important future development will be the analysis of the engine performance under transient conditions over homologation cycles.

Bibliography

[1] Eleanor Johnson. *Digital twins beginning to deliver real-world benefits*, CEO North America, 2025. https://ceo-na.com/technology/digital-twins-beginning-to-deliver-real-world-benefits/

[2] Gamma Technologies. https://www.gtisoft.com/gt-suite/

[3] Stefano D'Ambrosio, Cosimo Di Dio, Roberto Finesso. *Model-Based Calibration and Control of Tailpipe Nitrogen Oxide Emissions in a Light-Duty Diesel Engine and Its Assessment through Model-In-The-Loop*. Energies, 2023.

[4] Gamma Technologies. *GT-ISE Help, Reference Manual*, 2022.

[5] MathWorks. *MATLAB Help Center*. https://it.mathworks.com/help/releases/R2024b/images/ref/corr2.html?searchPort=51860

[6] MathWorks.*MATLAB Help Center*, https://it.mathworks.com/help/releases/R2024b/matlab/ref/rmse.html?searchPort=51860

[7] Anton Proskurnikov. *Automatic control*, Politecnico di Torino, 2021/2022.

[8] Carlo Novara, Nicola Amati. *Driver assistance system design*, Politecnico di Torino, 2022/2023.

[9] Stefano D'Ambrosio. *Propulsion systems and their applications to vehicles*, Politecnico di Torino, 2022/2023.

[10] Federico Millo. *Engine emissions control*, Politecnico di Torino, 2023/2024.